

**Presynaptic regulation of neurotransmitter release:
RIM-binding protein 2 sets release probability
by fine-tuning Ca²⁺ channel localization**

Inaugural-Dissertation

to obtain the academic degree

Doctor rerum naturalium (Dr. rer. nat.)

submitted to the Department of Biology, Chemistry and Pharmacy

of Freie Universität Berlin

by

Marie Katharina Grauel

from Berlin

2017

Die vorliegende Arbeit wurde im Zeitraum von Januar 2013 bis Januar 2017 unter der Leitung von Prof. Dr. Christian Rosenmund im Exzellenzcluster NeuroCure der Medizinischen Fakultät Charité – Universitätsmedizin Berlin angefertigt.

1. Gutachter: Prof. Dr. Christian Rosenmund

2. Gutachter: Prof. Dr. Stephan J. Sigrist

Disputation am 10. Juli 2017

Table of Contents

Table of Contents	5
Summary	7
Zusammenfassung	9
1. Introduction	13
1.1. The chemical synapse and synchronous neurotransmitter release	13
1.2. The AZ core complex at central vertebrate synapse	14
1.3. Presynaptic voltage-gated Ca²⁺ channels	18
1.4. RIM-binding proteins	19
1.4.1 Structure of RIM-BP genes and proteins.....	19
1.4.2 Expression of RIM-BP proteins in mice	21
1.4.3 RIM-BP localization and interactions	22
1.4.4 RIM-BP function	23
1.5. Aims of this work	24
2. Research Article	27
3. Discussion	49
4. Conclusion	50
5. Appendix	53
5.1. References	53
5.2. List of Figures and Tables	59
5.3. Nomenclature	60
5.4. Statement of contribution	61
5.5. Acknowledgements	62
5.6. Curriculum Vitae	63
5.7. Erklärung an Eides statt	65

Summary

Fast neuronal communication is fundamental to sensory information processing and all cognitive function in the brain, including memory formation and retrieval. The necessary temporal and spatial precision of neurotransmitter-based information transfer can only be achieved by a highly efficient synaptic vesicle release machinery combined with an exceptionally accurate spatial arrangement of the sites of Ca^{2+} entry. The presynaptic area of neurotransmitter release is called the active zone. It comprises the key proteins fundamental to both these prerequisites, including Rab3-interacting molecules (RIMs), Munc13s, a-liprins, ELKS, piccolo, bassoon and RIM-binding proteins (RIM-BPs). We were interested in the role of RIM-BPs in neurotransmitter release for three reasons: First, RIM-BPs have been shown to bind to RIMs, Bassoon and voltage-gated Ca^{2+} channels. Second, at the *Drosophila melanogaster* neuromuscular junction RIM-BP is crucial for presynaptic ultrastructure, Ca^{2+} channel coupling and neurotransmitter release. Third, RIM-BPs have been associated with autism spectrum disorders (ASD), however, until recently little was known about their exact function in vertebrate central synapses.

In this study we set out to elucidate the role of RIM-BP1 and RIM-BP2 in neurotransmitter release at murine hippocampal synapses. We investigated knockout (KO) mouse lines lacking RIM-BP1, RIM-BP2 or both proteins and compared neurotransmission in neurons from WT and KO animals. We focused mainly on RIM-BP2 as RIM-BP2 had higher expression levels than RIM-BP1 in hippocampal neurons and initial electrophysiological characterization indicated a more important functional role of RIM-BP2 as well.

First, we assessed basic electrophysiological parameters in glutamatergic hippocampal neurons grown in autaptic cell culture (Grauel et al., 2016; Fig. 1B-K). Evoked release and vesicular release probability (P_{VR}) were significantly reduced, while the size of the readily-releasable pool (RRP) of fusion-component vesicles and spontaneous release were unaltered in RIM-BP2-deficient synapses. Measurements of the paired-pulse ratio (PPR) of evoked transmitter release and responses to train stimulations showed a strong facilitation compared to WT, supporting the hypothesis of a reduced release probability. We independently verified this phenotype in recordings from area CA1 of acute hippocampal slices, underlining the validity of the results (Grauel et al., 2016; Fig. 2).

Initial recordings in RIM-BP1-deficient cultured neurons did not reveal any detectable effect of RIM-BP1 deletion on synaptic transmission (unpublished data). Since this could be due to a functional redundancy of RIM-BP1 and RIM-BP2 we analyzed neurotransmission in area CA1 of acute hippocampal slices of RIM-BP1/2 DKO animals (Grauel et al., 2016; Fig. S4G-I). We could not detect a significant difference in the PPR or short-term plasticity of RIM-BP2 KO and RIM-BP1/2 DKO animals, demonstrating that RIM-BP2 does not functionally substitute for RIM-BP1 and that RIM-BP2 is indeed the more relevant isoform in these hippocampal neurons.

The observed reduction in release probability and increase in facilitation could be explained by either an impairment in the molecular priming of synaptic vesicles or a deficiency in the spatial coupling of Ca^{2+} channels to release sites, also termed 'positional priming'.

The analysis of spontaneous release rates, fusogenicity and release kinetics of the RRP in autaptic hippocampal neurons largely excluded a role of RIM-BP2 in molecular priming (Grauel et al., 2016; Fig. S3D-G).

We next analyzed parameters that could point to an impairment of positional priming (Grauel et al., 2016; Fig. 3). The global Ca^{2+} influx into presynaptic terminals, assessed by Ca^{2+} imaging using SynGCamp6f, was not reduced in RIM-BP2 neurons. However, due to the limited spatial resolution of the technique, the results cannot exclude changes in the local Ca^{2+} signal in the vicinity of the Ca^{2+} sensor synaptotagmin.

We examined the dependence of neurotransmitter release on external Ca^{2+} concentrations (Grauel et al., 2016; Fig. 3D-G). The Hill function fit indicated that the number of Ca^{2+} channels and Ca^{2+} cooperativity of release was largely unaffected by RIM-BP2 deletion. However, the significant alterations in P_{VR} and PPR seen at lower external Ca^{2+} concentrations in RIM-BP2 KO neurons were rescued by increasing external Ca^{2+} concentrations above physiological levels. These data suggest that there is indeed an impairment of Ca^{2+} secretion coupling in the RIM-BP2-deficient synapses.

Next, we evaluated Ca^{2+} channel localization at the presynaptic active zone using superresolution light microscopy in mouse brain cryosections (Grauel et al., 2016; Fig. 4). Dual- and triple-channel time-gated stimulation emission depletion (gSTED) microscopy for Bassoon and P/Q-type Ca^{2+} channels ($\text{Ca}_v2.1$), as well as RIM1, $\text{Ca}_v2.1$ and the postsynaptic marker Homer1 showed that the relative localization of the presynaptic active zone marker Bassoon and $\text{Ca}_v2.1$ s was indeed altered in the absence of RIM-BP2, suggesting an impairment of the subsynaptic localization of Ca^{2+} channels. Functionally, this altered localization resulted in an increased coupling distance between the Ca^{2+} channels and the Ca^{2+} sensor for release, as judged by the stronger effect of the membrane-permeable Ca^{2+} chelator EGTA-AM on EPSC amplitudes and P_{VR} in RIM-BP2-deficient neurons (Grauel et al., 2016; Fig. S6).

In summary, our data shows that at murine glutamatergic hippocampal synapses RIM-BP2 supports the precise positioning of Ca^{2+} channels within the active zone and thereby assures appropriate synaptic function. In the absence of RIM-BP2 the fine positioning of Ca^{2+} channels is altered, albeit moderately, which reduces release probability and changes short-term plasticity properties of these synapses. In particular the latter phenotype could provoke significant alterations in the computational properties of the neuronal network and therefore underlie neurological disorders, such as ASD, associated with mutations in RIM-BP genes.

Zusammenfassung

Effiziente neuronale Kommunikation ist eine Grundvoraussetzung für Informationsverarbeitung und jegliche kognitiven Prozesse im Gehirn. Die hierfür notwendige zeitliche und räumliche Präzision des neurotransmitterbasierten Informationstransfers kann nur durch die Kombination einer höchsteffizienten Freisetzungsmaschinerie mit einer akkuraten räumlichen Kopplung der Kalziumkanäle und der Freisetzungstellen erreicht werden. Der hochspezialisierte präsynaptische Bereich, in dem neurotransmittergefüllte synaptische Vesikel mit der Plasmamembran fusionieren, wird aktive Zone genannt. Sie wird aus einer Reihe von Proteinen gebildet, die für diese Funktionen unbedingt erforderlich sind. Dazu gehören unter anderem Rab3-interacting molecules (RIMs), Munc13s, α -liprins, ELKS, piccolo, bassoon and RIM-binding proteins (RIM-BPs).

Wir waren aus drei Gründen insbesondere an der Rolle von RIM-BPs bei der Freisetzung von Neurotransmittern interessiert: Erstens interagieren RIM-BPs mit RIMs, Bassoon und spannungsabhängigen Kalziumkanälen. Zweitens ist RIM-BP essenziell für die Integrität der präsynaptischen Ultrastruktur, sowie die räumliche Kopplung spannungsabhängiger Kalziumkanäle und Neurotransmitterfreisetzung an der neuromuskulären Synapse von *Drosophila melanogaster*. Drittens wurden RIM-BPs in mehreren Studien mit Autismus-Spektrum-Störungen in Verbindung gebracht. Dennoch war bis vor kurzem wenig über die exakte Funktion dieser Proteinfamilie in zentralen Synapsen von Wirbeltieren bekannt.

Das Ziel der vorliegenden Arbeit war es, die Rolle von RIM-BP1 und RIM-BP2 in der Neurotransmitterfreisetzung an murinen hippocampalen Synapsen zu untersuchen. Hierfür haben wir *Knockout* (KO)-Mauslinien für RIM-BP1 und RIM-BP2, sowie eine RIM-BP1/2 Doppel-KO-Mauslinie generiert und die Neurotransmitterfreisetzung in Wildtyp (WT)- und KO-Neuronen verglichen. Wir haben uns vor allem auf RIM-BP2 konzentriert, da RIM-BP2 in hippocampalen Neuronen höhere Expressionslevel aufwies als für RIM-BP1 und eine anfängliche elektrophysiologische Charakterisierung darauf hinwies, dass RIM-BP2 auch funktionell eine wichtigere Rolle in diesem Neuronentyp spielt als RIM-BP1.

Zunächst haben wir eine grundlegende elektrophysiologische Charakterisierung RIM-BP2-defizienter glutamaterger hippocampaler Neurone vorgenommen (Grauel et al., 2016; Fig. 1B-K). Die evozierte Glutamatfreisetzung (EPSC) und die vesikuläre Freisetzungswahrscheinlichkeit (P_{VR}) war signifikant vermindert, während die Größe des Pools fusionskompetenter synaptischer Vesikel (*readily-releasable pool*, RRP) und die spontane Neurotransmitterfreisetzung unverändert waren. Messungen der Neurotransmitterfreisetzung bei Stimulation mit zwei Pulsen (*Paired-Pulse Ratios* (PPR)) oder mit 50 Pulsen bei 10 Hz zeigten eine stärkere Faszilitierung als in WT-Neuronen. Dies stützt die Hypothese, dass die Freisetzungswahrscheinlichkeit in RIM-BP2 KO-Neuronen reduziert ist. Wir haben diese Ergebnisse in Messungen in der CA1-Region akuter hippocampaler Schnitte unabhängig

verifiziert. Dies unterstreicht zusätzlich die Validität der Ergebnisse (Grauel et al., 2016; Fig. 2).

Anfängliche Messungen in RIM-BP1-defizienten Neuronen offenbarten keinen signifikanten Phänotyp (unveröffentlichte Daten, siehe *Figure 6, Introduction*). Wir haben daher die Neurotransmission in akuten hippocampalen Schnitten RIM-BP1/2 defizienter Tiere analysiert, um eine mögliche funktionelle Redundanz von RIM-BP1 und RIM-BP2 zu untersuchen (Grauel et al., 2016; Fig. S4G-I). Wir konnten jedoch keinen Unterschied zwischen RIM-BP2 KO und RIM-BP1/2 DKO hinsichtlich der PPR oder der Kurzzeitplastizität feststellen. Diese Ergebnisse zeigen, dass RIM-BP2 RIM-BP1 nicht funktionell ersetzen kann und RIM-BP2 tatsächlich die funktionell relevantere Isoform in hippocampalen Neuronen darstellt.

Der beobachteten Reduktion der Freisetzungswahrscheinlichkeit in RIM-BP2-defizienten Neuronen könnte ein Defekt entweder im molekularen *Priming* der synaptischen Vesikel oder in der räumlichen Kopplung von spannungsabhängigen Kalziumkanälen (*Positional Priming*) und Freisetzungstellen zugrunde liegen.

Die Analyse der spontanen Freisetzungsrates, sowie der Fusogenizität und der Freisetzungskinetiken des RRP in autaptischen hippocampalen Neurone schloss eine Funktion von RIM-BP2 im *Molecular Priming* weitestgehend aus (Grauel et al., 2016; Fig. S3D-G).

Als Nächstes analysierten wir Parameter, die auf einen Defekt im *Positional Priming* hindeuten könnten (Grauel et al., 2016; Fig. 3). Der globale Kalziumeinstrom in die Präsynapse RIM-BP2-defizienter Neurone, gemessen mithilfe von SynGCamp6f, war jedoch nicht verändert. Aufgrund der begrenzten räumlichen Auflösung dieser Methode können diese Ergebnisse jedoch nicht mögliche Veränderungen im lokalen Kalziumprofil in der unmittelbaren Umgebung des Kalziumsensors Synaptotagmin ausschließen.

Des Weiteren haben wir die Abhängigkeit der Neurotransmitterfreisetzung von der externen Kalziumkonzentration untersucht. Das Hill-Diagramm zeigte, dass die Gesamtanzahl der Kalziumkanäle, sowie die Kalziumkooperativität der Neurotransmitterfreisetzung in RIM-BP2 KO Neuronen nicht beeinträchtigt war. Die signifikanten Unterschiede der P_{VR} und PPR zwischen WT- und RIM-BP2 KO-Neuronen in niedrigen Kalziumkonzentrationen verschwanden jedoch, wenn die externen Kalziumkonzentrationen über ein physiologisches Niveau angehoben wurde. Diese Resultate zeigen, dass in RIM-BP2-defizienten Synapsen tatsächlich ein Defekt in der Kopplung von Kalziumeinstrom und Neurotransmitterfreisetzung vorliegt.

Schließlich haben wir die Lokalisierung der Kalziumkanäle an der präsynaptischen aktiven Zone mittels *Stimulated Emission Depletion* (STED) Mikroskopie in Kryoschnitten von WT und RIM-BP2 KO Mausgehirnen untersucht (Grauel et al., 2016; Fig. 4). Zweikanal und Dreikanal- STED-Mikroskopie für Bassoon und den P/Q-Typ spannungsabhängiger Kalziumkanäle ($Ca_v2.1$), sowie RIM1, $Ca_v2.1$ und das postsynaptische Markerprotein Homer1 zeigten, dass die relative Lokalisation des aktiven Zonen Markers Bassoon und der $Ca_v2.1$ -Kanäle in Abwesenheit von RIM-BP2 tatsächlich verändert war. Diese Ergebnisse deuten auf einen Defekt in der subsynaptischen Lokalisierung der

Kalziumkanäle hin. Funktionell resultierte dies in einer erhöhten Kopplungsdistanz zwischen Kalziumkanälen und Kalziumsensor, verdeutlicht durch den stärkeren Effekt des langsamen Kalziumchelators EGTA-AM auf EPSC und P_{VR} in RIM-BP2-defizienten Neuronen.

Zusammengefasst zeigen unsere Ergebnisse, dass in murinen glutamatergen hippocampalen Synapsen RIM-BP2 die präzise Positionierung spannungsabhängiger Kalziumkanäle in der aktiven Zone aufrechterhält. Dadurch gewährleistet RIM-BP2 die adäquate Funktion der Synapse. Fehlt RIM-BP2, führt dies zu einer moderaten Veränderung in der Feinpositionierung der Kalziumkanäle. Diese wiederum resultieren in einer signifikanten Verminderung der initialen Freisetzungswahrscheinlichkeit und Veränderungen in den Kurzzeitplastizitätseigenschaften dieser Synapsen. Insbesondere die veränderte Kurzzeitplastizität könnte eine signifikante Auswirkung auf die Eigenschaften des neuronalen Netzwerks zur Folge haben und somit den neurologischen Störungen zugrunde liegen, die mit Mutationen in den RIM-BP-Genen in Verbindung gebracht werden.

1. Introduction

1.1. The chemical synapse and synchronous neurotransmitter release

The functional basis of all cognitive processes, including processing of sensory stimuli, learning and memory, is rapid communication between neurons. The contact points between sending and receiving neurons are termed synapses. They comprise a presynaptic compartment, which releases neurotransmitter molecules, the synaptic cleft, and a postsynaptic compartment, where the neurotransmitters bind to their receptors (Figure 1A).

The active zones (AZs) are the presynaptic sites specialized for neurotransmitter release in response to an action potential. Neurotransmitters, such as glutamate, γ -aminobutyric acid (GABA), glycine and acetylcholine (ACh), are stored in synaptic vesicles (SVs), which are first moved towards and then attached (docked) to the AZs. SVs become release-competent by a process termed ‘priming’. In the primed state, the SV membrane and the plasma membrane are thought to be held in close proximity to each other by the SNARE complex, a four-helix bundle formed by the soluble N-ethylmaleimide-sensitive factor attachment protein receptors (SNAREs) SNAP-25, syntaxin-1 and synaptobrevin-2 (Poirier et al., 1998; Sutton et al., 1998). Action potential firing transiently depolarizes the plasma membrane of the terminal, which triggers the opening of voltage-gated Ca^{2+} channels (Ca_v s). Ca^{2+} then enters the presynapse and binds to a Ca^{2+} sensor (i.e. Synaptotagmin-1 for fast release (Fernández-Chacón et al., 2001)). This ultimately leads to the fusion of the two membranes (reviewed in Rizo and Rosenmund, 2008; Südhof, 2013) - presumably through the final zippering of the SNARE complex - neurotransmitter release and activation of the postsynaptic receptors.

Synaptic firing rates can range from $< 1\text{ Hz}$ to 1 kHz , depending on the neuron type (Hallermann and Silver, 2013). Additionally, synapses adapt their strength or efficacy in an activity-dependent manner. Changes in efficacy, referred to as synaptic plasticity can occur through presynaptic or postsynaptic mechanisms, and can increase (potentiation/facilitation) or decrease (depression) synaptic strength (reviewed in Citri and Malenka, 2008; Malenka and Bear, 2004; Zucker and Regehr, 2002). Synaptic plasticity changes have differing duration: Short-term plasticity (STP) lasts milliseconds to seconds, while long-term plasticity (LTP) affects transmission for minutes to hours. Both types of plasticity are crucial for information processing, and long-term potentiation in particular has been associated with learning and memory (Bliss and Collingridge, 1993).

In summary, synapses fulfill a number of complex functional requirements in order to assure that synaptic transmission remains both dynamic and reliable. Therefore, action potential-triggered synchronous neurotransmitter release is a tightly regulated process and relies on several factors: an extremely efficient release machinery, a highly accurate spatial arrangement of Ca_v s in regard to the neurotransmitter release sites, and the accurate alignment of the PSD exactly opposite of the AZ. The

presynaptic AZ contains a number of specialized proteins, which ensure the fine-tuning of each of these aspects (Rizo and Rosenmund, 2008).

1.2. The AZ core complex at central vertebrate synapse

AZs of central synapses are disc-like structures of 0.2-0.5 μm diameters (Holderith et al., 2012; Schikorski and Stevens, 1997; Südhof, 2012). They include at least seven core protein families crucial for adequate fast, synchronous neurotransmitter release: Rab3-interacting molecules (RIMs), Munc13s, α -liprins, ELKS, piccolo, bassoon and RIM-BPs (see Figure 1).

RIMs

The two longest vertebrate RIMs isoforms, RIM1a and RIM2 α , contain five functional domains (Figure 1): an N-terminal Zinc finger domain, surrounded by α -helices, a central PDZ domain, a conserved PxxP motif and two C-terminal C₂ domains, C₂A and C₂B. The Zinc finger domain of RIM binds to the C₂A domain of Munc13-1 and ubMunc13-2, the two main isoforms of the priming factor Munc13 expressed in brain (Betz et al., 2001; Dulubova et al., 2005). This interaction activates Munc13 by disrupting its homodimerization and forming "active" RIM/Munc13 heterodimers (Deng et al., 2011; Lu et al., 2006). The α -helices surrounding the Zinc finger domain bind to the GTP-bound form of the SV protein Rab3 (Fukuda, 2003; Lu et al., 2006), which is a small SV-associated GTPase involved in SV cycling (Südhof, 2004).

The central PDZ domain of RIMs binds to Cav2.1 and Cav2.2 (Kaesler et al., 2011; see also Chapter 1.3 for Cav classification) as well as ELKS (Ohtsuka et al., 2002; Wang et al., 2002). It is essential for Cav recruitment to release sites (Han et al., 2011; Kaesler et al., 2011), a process referred to as 'positional priming'. RIMs also bind to RIM-binding proteins (RIM-BPs) through their PxxP motif (Hibino et al., 2002; Kaesler et al., 2011). This interaction appears to be equally essential for correct Cav localization (Kaesler et al., 2011).

Additionally, a C-terminal sequence of RIMs binds to the β -subunit of Cav_s thereby inhibiting Cav inactivation (Kiyonaka et al., 2007). Finally, the C-terminal C₂B domain of RIMs also binds to α -liprins and synaptotagmin-1 (Schoch et al., 2002) and C₂A and C₂B possibly bind to Cav_s and SNARE proteins (Coppola et al., 2001).

Synapses lacking all isoforms of RIM1 and RIM2 exhibit severe impairment in SV docking and priming (Deng et al., 2011; Han et al., 2011; Kaesler et al., 2011), as well as Cav recruitment to the AZ (Kaesler et al., 2011). Only the expression of RIM constructs containing both the PDZ domain and the PxxP motif can rescue the presynaptic loss of Cav_s (Kaesler et al., 2011), suggesting that RIMs function in positional priming in concert with RIM-BPs.

Functionally, RIM1 α has been shown to be crucial for STP (Kintscher et al., 2013; Schoch et al., 2002) and has also been implicated in presynaptic LTP at some, but not all types of

specialized vertebrate synapses expressing this type of LTP (Castillo et al., 2002; Kintscher et al., 2013). RIM1 α acts in synaptic plasticity possibly *via* binding to Rab3s (Castillo et al., 1997, 2002; Schoch et al., 2002; Südhof, 2012), while phosphorylation at serine-413 by protein kinase A is not required for presynaptic LTP (Kaesler et al., 2008; Yang and Calakos, 2010)

Munc13s

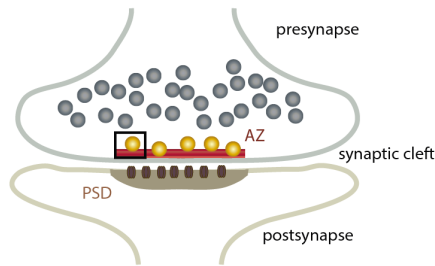
Munc13s are fundamental factors for molecular priming of SVs at the AZ. Together with Munc18-1, they orchestrate SNARE complex assembly. Key to this priming function is the α -helical MUN domain common to all Munc13s (Basu et al., 2005; Figure 1).

All Munc13 isoforms expressed in the brain additionally contain a diacylglycerol (DAG)-binding C₁ domain as well as a central and a C-terminal C₂ domain (C₂B and C₂C, respectively). These three domains have been implicated in bridging the SV and plasma membranes to facilitate SNARE complex assembly by the MUN domain (Liu et al., 2016; Xu et al., 2017).

The most abundant mammalian isoform, Munc13-1, and the ubiquitously expressed form of Munc13-2 (ubMunc13-2) both contain an additional N-terminal C₂ domain (C₂A) not present in other Munc13 isoforms. The C₂A domain allows Munc13 to form homodimers, thereby inhibiting the priming function of the MUN domain (Deng et al., 2011). RIMs release Munc13 homodimerization and form "active" RIM/Munc13 heterodimers (Deng et al., 2011). Consequently, deletion of both Munc13-1 and Munc13-2 results in the complete arrest of evoked and spontaneous neurotransmitter release (Varoqueaux et al., 2002) and a severe impairment of SV docking (Imig et al., 2014).

Additionally, Munc13s regulate multiple forms of presynaptic STP. These include isoform-specific depression and facilitation (Rosenmund et al., 2002), DAG/phorbol ester-dependent potentiation of release requiring the C₁ domain (Basu et al., 2007; Rhee et al., 2002) and Ca²⁺-dependent STP involving the C₂B domain and a central calmodulin (CaM)-binding region (Junge et al., 2004; Shin et al., 2010; Xu et al., 2017).

A



B

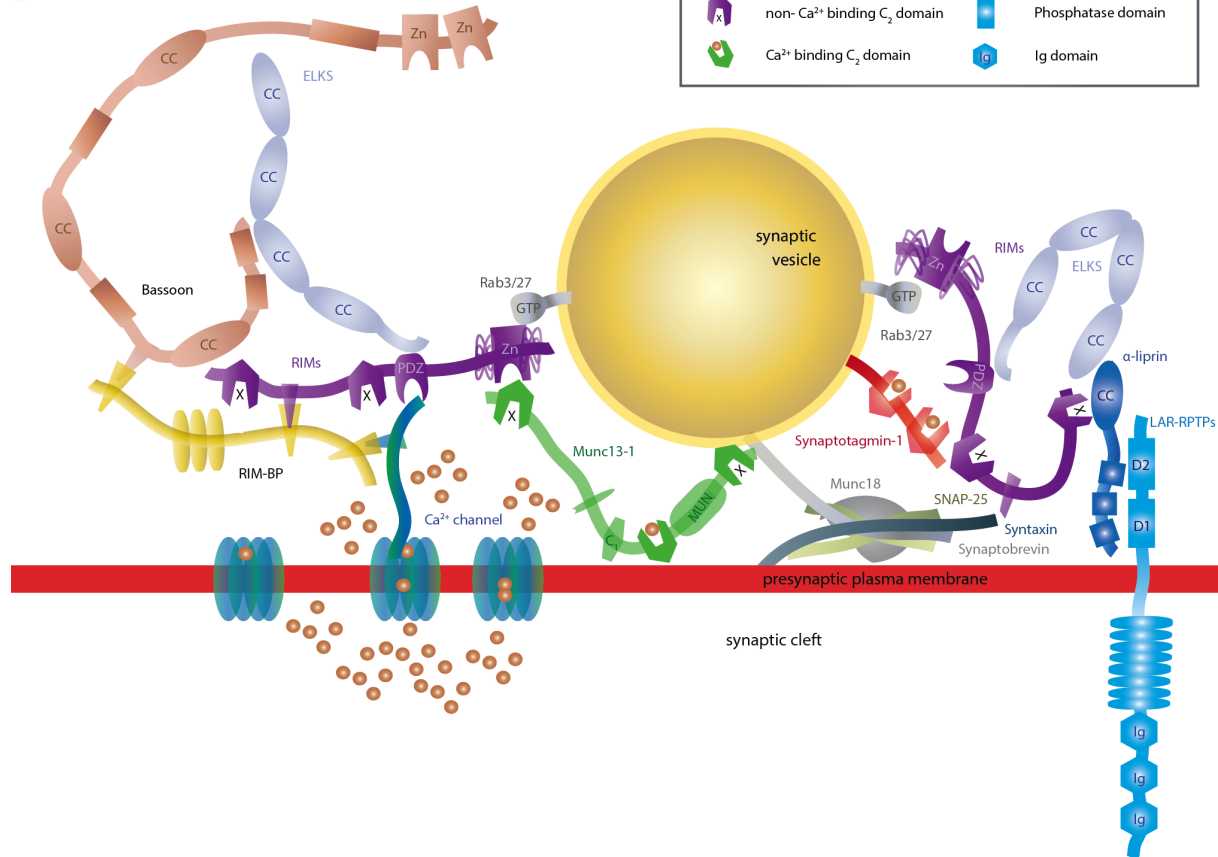


Figure 1 The presynaptic active zone. (A) Scheme of a typical central synapse comprising a presynaptic compartment with the active zone (AZ), the synaptic cleft and the postsynaptic compartment with the postsynaptic density (PSD) containing neurotransmitter receptors. (B) Detailed scheme of the black box in (A). The main proteins of the AZ are depicted with their domain structure and binding partners. Piccolo, Ca^{2+} channel auxiliary subunits and some other interaction partners have been omitted for clarity.

α -liprins

Not much is known about α -liprin function in vertebrate systems. They form homodimers (Serra-Pagès et al., 1998; Taru and Jin, 2011) or heterodimers with β -liprins (Serra-Pagès et al., 1998), bind to RIMs (Schoch et al., 2002), ELKS (Dai et al., 2006; Ko et al., 2003a) and Leukocyte-common antigen related (LAR) -type receptor phosphotyrosine phosphatases (Serra-Pagès et al., 1995, 1998; Figure 1). Additionally, α -liprins interact with GIT1, CASK and mDiaphanous (Ko et al., 2003b; Olsen et al., 2005; Sakamoto et al., 2012). In *Caenorhabditis elegans* and *Drosophila melanogaster*, loss of α -liprins alters the size of the presynaptic AZ (Kaufmann et al., 2002; Zhen and Jin, 1999).

Overall, α -liprins appear to link AZ formation and the presynaptic AZ core complex to trans-synaptic cell adhesion (Südhof, 2012).

ELKS

ELKS consist of four coiled-coil domains (Figure 1), which bind to α -liprins (Ko et al., 2003a), Bassoon (Takao-Rikitsu et al., 2004), and β -subunits of Ca^{2+} channels (Kiyonaka et al., 2012). A C-terminal sequence, present only in some isoforms, additionally binds to the RIM PDZ domain (Wang et al., 2002).

Deletion of ELKS reduces Ca^{2+} influx to the presynapse and decreases neurotransmitter release probability in inhibitory neurons (Liu et al., 2014). At excitatory synapses ELKS deletion reduces the size of the readily-releasable pool (RRP) of SVs without changing Ca^{2+} influx or release probability (Sugawara and Nikaido, 2014). Interestingly, the C-terminal sequence known to bind to RIM is dispensable for this function in RRP enhancement.

Piccolo and Bassoon

Piccolo and Bassoon are structurally related large multi-domain proteins encompassing ten highly conserved regions (Piccolo Bassoon homology regions PBH1-10, Figure 1). Both proteins are involved in a large number of protein-protein interactions (Schoch and Gundelfinger, 2006) and have been implicated in SV clustering and the maintenance of SV pools (Hallermann and Silver, 2013; Mukherjee et al., 2010). Additionally, they are indispensable for the assembly of precursor vesicles for AZ assembly (Dresbach et al., 2006; Maas et al., 2012). However, deletion of Bassoon or Piccolo affects the ultra-structural organization of the AZ only in specialized sensory synapses, such as photoreceptor and hair cell ribbon synapses (Dick et al., 2003; Khimich et al., 2005; Regus-Leidig et al., 2014), but not in the central synapses (Altrock et al., 2003; Leal-Ortiz et al., 2008; Mukherjee et al., 2010).

Bassoon is thought to recruit SVs to vacated release sites (Hallermann et al., 2010; Mendoza Schulz et al., 2014) and to position Ca_v s near release sites, through its interactions with RIM-BPs and Ca^{2+} channels (Chen et al., 2011; Davydova et al., 2014; Frank et al., 2010). Piccolo interacts with several actin-associated proteins (Gundelfinger et al., 2016) and regulates activity-induced F-actin assembly in presynaptic boutons, thereby enabling efficient synaptic transmission (Waites et al., 2011).

Additionally to their function in synaptic release, both Bassoon and Piccolo are critical regulators of the ubiquitin-proteasome and the autophagy-lysosomal systems through their interactions with Siah1, and thus control presynaptic proteostasis and synaptic integrity (Waites et al., 2013).

1.3. Presynaptic voltage-gated Ca^{2+} channels

At least three gene families, comprising ten subtypes of voltage-gated Ca^{2+} channels (Ca_v s), are expressed in the nervous system (see Table 1). In the central nervous system, action potential-triggered Ca^{2+} influx is mostly mediated by presynaptic N-type and P/Q-type channels (Dunlap et al., 1995; Olivera et al., 1994), although R-type channels might also contribute at some synapses (Breustedt et al., 2003; Gasparini et al., 2001). In contrast, the L-type channels $\text{Ca}_\text{v}1.3$ and $\text{Ca}_\text{v}1.4$ trigger neurotransmitter release in specialized sensory synapses, such as cochlear hair cells and retinal photoreceptor ribbon synapses, respectively (Catterall, 2011).

Ca^{2+} Channel family	Pore-forming subunit	Ca^{2+} Current	Specific blocker
$\text{Ca}_\text{v}1.1$	$\alpha_{1\text{S}}$	L-type	DHP (dihydropyridine)
$\text{Ca}_\text{v}1.2$	$\alpha_{1\text{C}}$	L-type	DHP (dihydropyridine)
$\text{Ca}_\text{v}1.3$	$\alpha_{1\text{D}}$	L-type	DHP (dihydropyridine)
$\text{Ca}_\text{v}1.4$	$\alpha_{1\text{F}}$	L-type	DHP (dihydropyridine)
$\text{Ca}_\text{v}2.1$	$\alpha_{1\text{A}}$	P/Q-type	ω -agatoxin IVA
$\text{Ca}_\text{v}2.2$	$\alpha_{1\text{B}}$	N-type	ω -conotoxin GVIA
$\text{Ca}_\text{v}2.3$	$\alpha_{1\text{E}}$	R-type	SNX-482
$\text{Ca}_\text{v}3.1$	$\alpha_{1\text{G}}$	T-type	-
$\text{Ca}_\text{v}3.2$	$\alpha_{1\text{J}}$	T-type	-
$\text{Ca}_\text{v}3.3$	$\alpha_{1\text{I}}$	T-type	-

Table 1 Voltage-gated Ca^{2+} channel gene families and subtypes

The α -subunits of Ca_v s make up the actual pore (Figure 2) and contain most sites of channel regulation (reviewed in Catterall and Few, 2008; Catterall et al., 2013). The auxiliary subunits β , $\alpha_2\delta$, and in some cases γ , influence Ca^{2+} channel function and cell-surface expression (Catterall et al., 2013).

Neurotransmitter release is triggered by Ca^{2+} influx through one or several Ca_v s forming a cluster, depending on the synapse type and developmental stage (reviewed in Eggermann et al., 2011). The number and distribution of Ca_v s critically shape the local Ca^{2+} profile "seen" by the Ca^{2+} sensor for release. Therefore both parameters are determining factors for the efficacy and speed of synaptic transmission and strongly influences STP and LTP properties of individual synapses (Nadkarni et al., 2012; Sheng et al., 2012). The number of open Ca_v s necessary for neurotransmitter release can be determined by application of slow Ca_v blockers, while the coupling distance between Ca_v s and Ca^{2+} sensor can be assessed using intracellular application of the exogenous Ca^{2+} chelators EGTA and BAPTA and quantitative modeling (Eggermann et al., 2011). Generally, one distinguishes

between microdomain coupling (coupling distance ≥ 100 nm) involving a larger number of Ca_Vs and nanodomain coupling (coupling distance < 100 nm) involving only few Ca_Vs (reviewed in Eggermann et al., 2011).

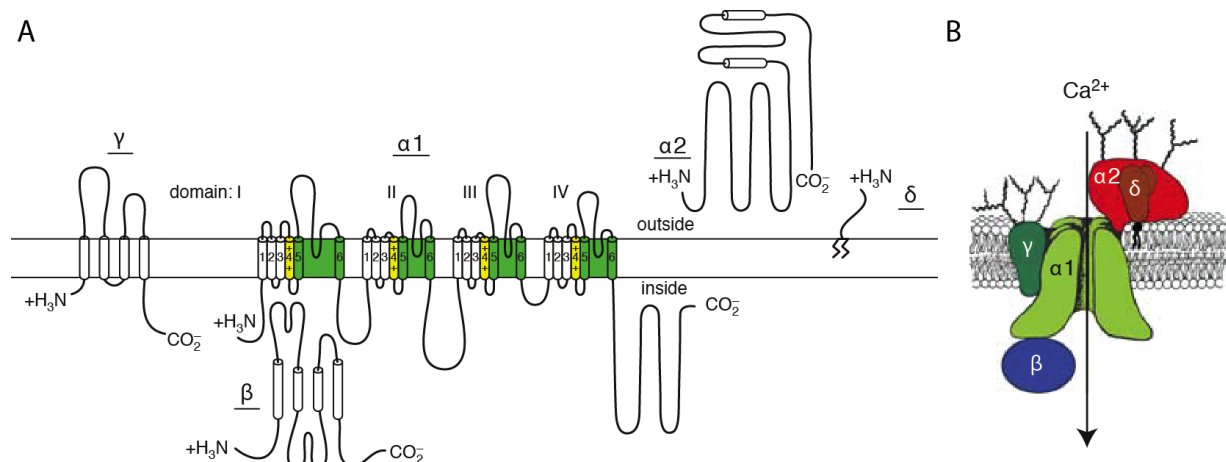


Figure 2 Structure of voltage-gated Ca^{2+} channels. (A) and (B) Subunit structure of the pore-forming $\alpha 1$ -subunit, the intracellular auxiliary subunit β , the disulfide-linked glycoprotein dimer of $\alpha 2$ and δ , and the auxiliary subunit γ present in some Ca^{2+} channel subtypes. The α -subunits consist of four transmembrane (TM) domains I - IV with six membrane-spanning helices S1 - S6 each. The p-loops between helices S5 and S6 are thought to function as ion selectivity filter. Cylinders represent predicted α -helices, the zigzag line a glycosylphosphatidylinositol anchor (adapted from Catterall, 2011).

1.4. RIM-binding proteins

1.4.1 Structure of RIM-BP genes and proteins

Mammalian genomes encode three RIM-binding proteins, while invertebrate genomes encode only one (Mittelstaedt and Schoch, 2007).

The RIM-BP1 gene (*Bzrap1*) is located on chromosome 11 in mice. At least 15 mouse *Bzrap1* transcripts have been deposited in the NCBI and Ensembl databases (Figure 3), encompassing up to 32 exons. The largest protein isoform spans 1,846 amino acids (aa) and has a molecular weight of 199.9 kDa [Ensembl transcript Bzrap1-001 (ENSMUST00000039627.11, identical to NCBI reference sequence NM_172449.2), UniProt entry Q7TNF8 isoform 1].

The *Rimbp2* gene is located on mouse chromosome 5. Six different protein-encoding transcripts have been annotated the Ensembl database. Two validated transcript reference sequences are found in the NCBI database (NM_001081388.2, identical to ENSMUST00000111346.5, and ENSMUST00000111346, identical to ENSMUST00000200470.4). The resulting protein isoforms (Uniprot entries Q80U40, D3YXR8 and A0A0G2JFB0) contain all known protein interaction sites and

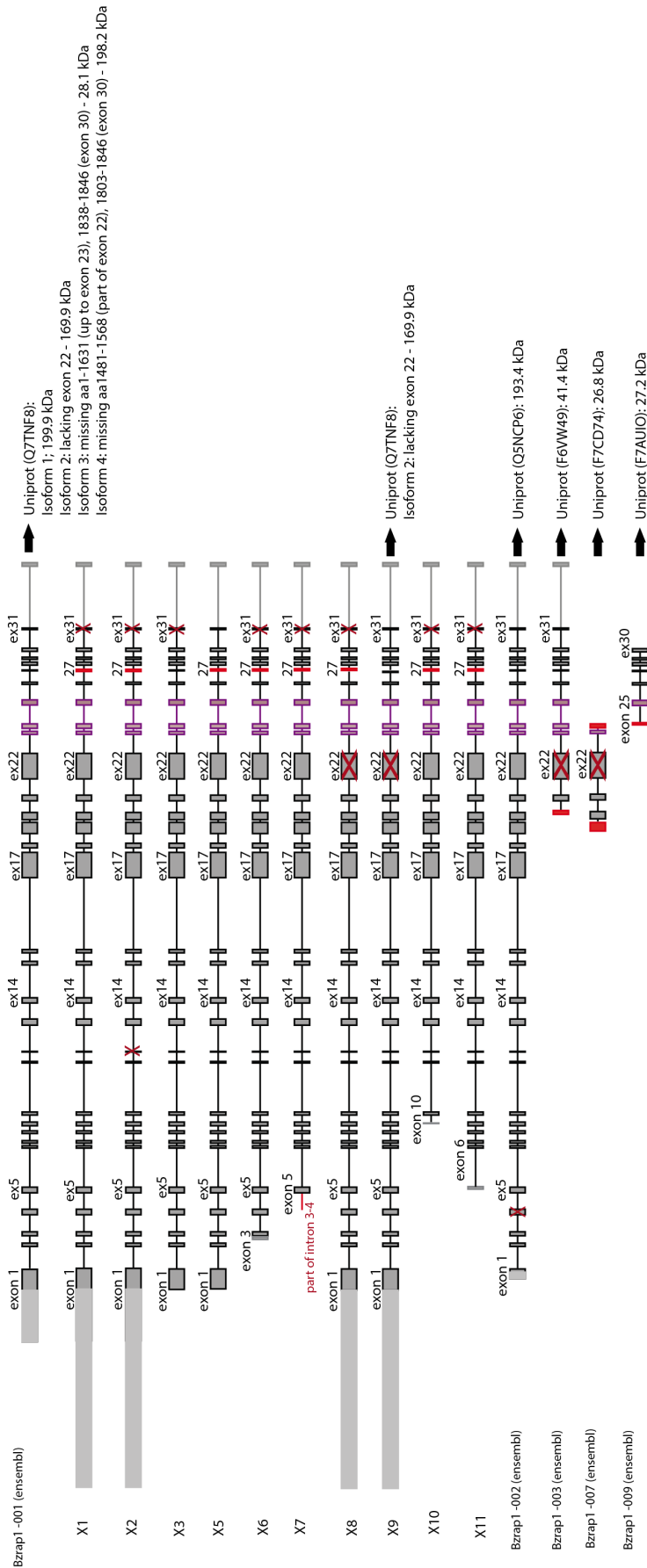


Figure 3 Overview of mouse Bzap1 (RIM-BP1) transcripts. Ensembl transcript Bzap1-001 is identical to NM_172449.2 (NCBI). The reference sequences X1-X11 (NCBI) are only predicted transcripts. Bzap1-002/003/007/009 are annotated transcripts in the Ensembl database.

vary in their lengths by only up to 10 aa. The longest isoform encompasses 1,079 aa and has a molecular weight of 119.1 kDa (UniProt entry D3YXR8).

The *Rimbp3* gene consists of a single exon located on mouse chromosome 6 (Mittelstaedt and Schoch, 2007) coding for a protein of 1,606 aa and 177,3 kDa (Ensembl transcript ENSMUST00000169803.2, UniProt entry E9PZY2).

All murine RIM-BP1 and RIM-BP2 isoforms consist of one central and two C-terminal SH3 domains (Figure 4), which are very well conserved. Additionally, they contain three central Fibronectin III (FNIII) repeats with a conserved β -sandwich structure formed by two antiparallel β -pleated sheets. RIM-BP3 equally possesses three SH3 domains but only two FNIII repeats.

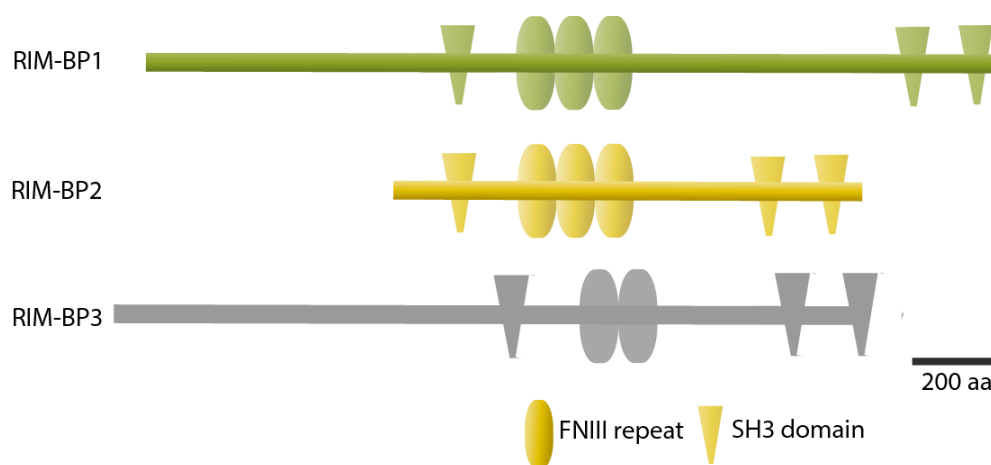


Figure 4 Schematic diagram of the domain structure of mouse RIM-BP isoforms. All three murine RIM-BPs encompass three highly conserved Src-homology 3 (SH3) domains and two to three fibronectin type III (FNIII) repeats.

1.4.2 Expression of RIM-BP proteins in mice

The highest expression levels of RIM-BP1 and RIM-BP2 have been reported for neuron-rich regions in the brain (Galiègue et al., 1999; Hibino et al., 2002; Mittelstaedt and Schoch, 2007). RIM-BP1 was shown to be more ubiquitously expressed, while RIM-BP2 expression is higher in rostral brain regions, including hippocampus, olfactory bulb and cortex, and is far less abundant in the cerebellum (Mittelstaedt and Schoch, 2007).

RIM-BP1 is expressed at low levels also in thymus, spleen and testis (Mittelstaedt and Schoch, 2007). In our hands, real-time PCR revealed low expression of RIM-BP1 also in kidney and heart, and of RIM-BP2 in heart, testis and thymus (unpublished data).

In contrast, RIM-BP3 is almost absent from the central nervous system, whereas its expression is high in non-neuronal tissue, such as thymus, liver, kidney, spleen and testes (Mittelstaedt and Schoch, 2007). Interestingly, RIM-BP3 has been shown to be crucial in spermatogenesis (Zhou et al., 2009).

1.4.3 RIM-BP localization and interactions

RIM-BPs primarily localize to presynaptic sites (Davydova et al., 2014; Hibino et al., 2002). In fractionation studies and synaptosome preparations RIM-BPs were detected in the same synaptic plasma membrane fraction as RIM and in the same insoluble fraction as RIM and Bassoon, respectively (Hibino et al., 2002). These data suggest that RIM-BPs are part of the same insoluble presynaptic complex as RIM and Bassoon. However, an additional expression in some postsynaptic neuron types cannot be fully excluded (Hibino et al., 2002).

At the *Drosophila melanogaster* neuromuscular junction (NMJ), the RIM-BP ortholog DRBP is exclusively localized to the presynaptic AZ. This AZ type contains a specialized scaffolding structure termed 'T-bar' (Figure 5). A major component of the T-bar is the coiled-coil domain protein Bruchpilot, which is crucial for the clustering of the Ca^{2+} channel subunit Cacophony (Cac) and SV release (Fouquet et al., 2009; Kittel et al., 2006). Stimulated emission depletion (STED) microscopy showed that DRBP encircles the Cac field beneath the Bruchpilot scaffold (Figure 5, Liu et al., 2011).

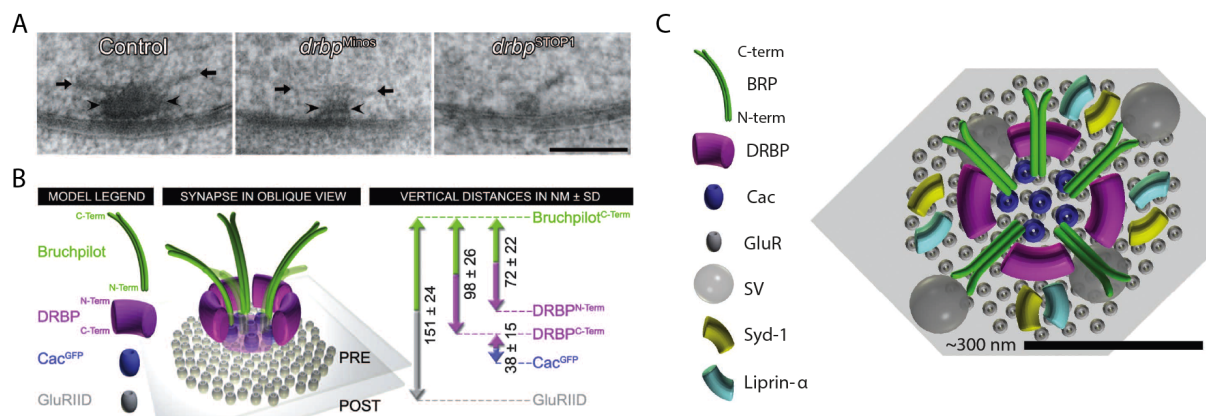


Figure 5 Structure of the T-bar at the AZ of *Drosophila* neuromuscular junction. (A) T-bar EM images from NMJs of controls, *drbp* hypomorphic (*drbp*^{Minos}) and *drbp*-deficient (*drbp*^{STOP1}) flies. T-bar pedestals are marked with arrowheads and T-bar platforms with arrows. (B) and (C) Model of an AZ in oblique view (B) and top view (C). Peak - to-peak vertical distance measurements were performed on two-color STED images. PRE, presynaptic; POST, postsynaptic; BRP, Bruchpilot; DRBP, Drosophila RIM-binding protein; Cac, Cacophony voltage-gated Ca^{2+} channel; GluR, glutamate receptor; SV, synaptic vesicle (adapted from Liu et al, 2011 and Maglione and Sigrist, 2013).

RIM-BP1 was originally discovered in a yeast-2-hybrid screen for binding partners of the peripheral benzodiazepine receptor (Galiègue et al., 1999). Shortly thereafter, murine RIM-BP1 and RIM-BP2 have been shown to bind to RIMs (Hibino et al., 2002; Wang et al., 2000) as well as to the α_{1D} -subunit of L-type Ca^{2+} channels ($\text{Ca}_v1.3$) and the α_{1B} -subunit of N-type ($\text{Ca}_v2.2$) Ca^{2+} channels (Hibino et al., 2002). Based on the sequence similarities it can also be argued that RIM-BPs can bind to P/Q-type ($\text{Ca}_v2.1$), R-type ($\text{Ca}_v2.3$) and other types of L-type channels ($\text{Ca}_v1.4$)

(Hibino et al., 2002). Additionally, RIM-BP1 and RIM-BP2 interact with Bassoon (Davydova et al., 2014).

All interactions characterized to date have been mapped to the SH3 domains of RIM-BPs. Concurrent binding of RIMs, Ca^{2+} channels and Bassoon to RIM-BPs is possible. Indeed, Hibino and colleagues showed that RIM-BP2 could bind RIM2 and α_{1D} simultaneously (Hibino et al., 2002), while Davydova and colleagues demonstrated simultaneous binding of Bassoon and $\text{Ca}_v2.1$ with RIM-BP2 (Davydova et al., 2014). Using surface plasmon resonance technology, Davydova and colleagues also showed that Bassoon preferentially binds to the first SH3 domain (SH3I), while RIMs and Ca_v s prefer binding to the C-terminal SH3 domains (SH3II and SH3III) (Davydova et al., 2014). In contrast, the function of the FNIII repeats remains unknown.

1.4.4 RIM-BP function

In PC12 cells, inhibiting RIM-BP2 interaction with either Ca_v s or RIM2 increases depolarization-activated secretion of growth hormone (Hibino et al., 2002), while overexpression of RIM-BP2 has no significant effect.

Disruption of the single *drbp* gene results in a loss of the T-bar structure at the AZ of the *Drosophila melanogaster* NMJ, and reduced abundance of Cac (Liu et al., 2011). Functionally, Ca^{2+} influx, evoked synaptic transmission and release probability are reduced, and rise times of evoked responses are significantly increased. This phenotype suggests a desynchronization of action potential arrival and neurotransmitter release, likely due to a Cac clustering defect at the AZ (Liu et al., 2011). Furthermore, short-term facilitation was significantly enhanced in the absence of DRBP (Liu et al., 2011). Additionally, presynaptic homeostatic potentiation of Ca^{2+} influx, neurotransmitter release and RRP size is impaired in DRBP-deficient NMJs (Müller et al., 2015). In the same study, DRBP mutants were also surprisingly sensitive to EGTA and showed a decelerated slow phase of SV recovery following RRP depletion. The authors concluded that DRBP stabilizes a high release probability SV pool residing in close proximity to the presynaptic Cac clusters and that DRBP deletion impairs the access to this pool and its replenishment after depletion (Müller et al., 2015). Recently, it was also shown that DRBP binds to the transport adaptor protein Aplip1/JIP1 *via* a C-terminal SH3 domain and that this interaction is essential for co-transport of Bruchpilot and DRBP to the sites of putative AZ formation (Siebert et al., 2015).

In humans, several genomic studies identified an association of RIM-BPs with autism-spectrum disorders (ASD) (Bucan et al., 2009; Hussman et al., 2011; Pinto et al., 2010). Several studies on mouse neurons indirectly pointed towards a prominent role of RIM-BPs in evoked neurotransmitter release in mammalian neurons. One study showed that the RIM-BP interaction motif in RIM1 α is necessary to rescue the shift in the Ca^{2+} dependency of neurotransmitter release observed in RIM1/2-deficient hippocampal neurons (Kaeser et al., 2011). The phenotype is presumably due to an

impairment in Ca_v clustering and the results indicate that the precise tethering of Ca_v s to the presynaptic AZs not only requires direct interaction of RIMs with Ca_v s but also with RIM-BPs (Kaesler et al., 2011). In another study, interference with the Bassoon-RIM-BP2 interaction led to an impairment in the synaptic localization of only $\text{Ca}_v2.1$ channels, but not $\text{Ca}_v2.2$ channels (Davydova et al., 2014), also suggesting an important role of RIM-BP2 in positional priming.

During our work on RIM-BPs, the first study on a RIM-BP knockout in murine neurons was published (Acuna et al., 2015). The authors analyzed the effect of a conditional deletion of both RIM-BP1 and RIM-BP2 in mass-cultured hippocampal neurons and at the Calyx of Held (Acuna et al., 2015). They described a surprisingly mild phenotype compared to that observed in *Drosophila melanogaster* NMJ. The AZ structure appeared intact in RIM-BP1/2-deficient hippocampal neurons and postsynaptic current amplitudes were not significantly altered. However, success rates of evoked excitatory postsynaptic currents (EPSCs) and variability of postsynaptic current amplitudes were increased. Additionally, paired-pulse ratios (PPRs) were increased in inhibitory neurons, arguing for a decreased release probability (Acuna et al., 2015). At the Calyx of Held, RIM-BP loss caused a significant reduction in EPSCs amplitudes. The coefficient of variation (C.V.) of EPSC amplitudes and rise-times was increased as well as the synaptic delay (Acuna et al., 2015). The authors concluded that the deletion of RIM-BPs decelerates and desynchronizes action potential-evoked neurotransmitter release. RRP release kinetics were also altered in RIM-BP1/2-deficient calyx terminals, while the size of the RRP was unaffected. Since deletion of RIM-BPs did not affect the total Ca^{2+} current or voltage dependence of Ca^{2+} currents but increased sensitivity of neurotransmitter release to the slow Ca^{2+} chelator EGTA, the authors concluded that RIM-BPs regulate the fidelity of the synaptic transmission likely through a tight coupling of presynaptic Ca^{2+} channels to the release machinery at the AZs.

1.5. Aims of this work

RIM-BPs have been repeatedly associated with ASD in genetic screens (Bucan et al., 2009; Hussman et al., 2011; Pinto et al., 2010). While a fundamental role in neurotransmitter release was revealed in *Drosophila melanogaster* NMJ, very little was known about RIM-BP function in mammalian synapses until recently. Our initial objective was therefore to characterize RIM-BP1 and RIM-BP2 function in neurotransmitter release in central mammalian synapses. More precisely, we aimed to dissect the specific roles and possible functional differences of each isoform. To this end, we designed constitutive single knockout mouse lines for RIM-BP1 and RIM-BP2, which were generated by Genoway, France.

Remarkably, we found that neurotransmitter release in RIM-BP1-deficient glutamatergic hippocampal neurons was not significantly different from WT neurons (Figure 6, unpublished data). In contrast, our initial analysis of RIM-BP2-deficient neurons indicated a significant increase in facilitation during

repetitive stimulation. We therefore focused on the role of RIM-BP2 in neurotransmitter release.

In the first part of this work, we performed a comprehensive analysis of evoked and spontaneous release, the RRP size, P_{VR} , the release probability of a synaptic terminal (P_R) and the STP characteristics in RIM-BP2 deficient hippocampal neurons by electrophysiology on autaptic cultures (Grauel et al., 2016, Fig. 1). We also assessed evoked release and STP in area CA1 of acute hippocampal slices prepared from RIM-BP2 KO and WT animals (Grauel et al., 2016, Fig. 2).

Moreover, we crossed the single KO lines to generate a RIM-BP1/2 double knockout (DKO) mouse line in order to uncover functional redundancies of RIM-BP1 and RIM-BP2 by studying synaptic transmission also in DKO neurons. We compared neurotransmitter release and STP of RIM-BP2-deficient and RIM-BP1/2 DKO neurons in area CA1 of acute hippocampal slices and found that additional deletion of RIM-BP1 did not exacerbate the RIM-BP2 phenotype (Grauel et al., 2016, Fig. S4). These results suggest that RIM-BP1 and RIM-BP2 do not have redundant functions. Instead, RIM-BP1 appears to play at most a marginal role in neurotransmission at excitatory hippocampal synapses.

The observed changes in release probability and STP in RIM-BP2-deficient neurons could be either due to impairments in the molecular priming of SVs, or defects in coupling of Ca_v s to the release sites at the AZs (positional priming). In a third part, we therefore used application of hypertonic sucrose solutions to analyze fusogenicity, which is the intrinsic propensity of SVs to fuse with the plasma membrane independent of Ca^{2+} levels, RRP peak release rates and spontaneous release rates and thereby ruled out major alterations in molecular priming function in the absence of RIM-BP2 (Grauel et al., 2016, Fig. S3).

In a fourth set of experiments, we analyzed Ca^{2+} influx into presynaptic terminals and Ca^{2+} secretion coupling and found that Ca^{2+} sensitivity of neurotransmitter release is indeed altered in RIM-BP2 KO neurons (Grauel et al., 2016, Figs. 3 & S3).

We established dual- and triple-channel gated STED (gSTED) to precisely visualize Ca^{2+} channel localization relative to pre- and postsynaptic marker proteins (Grauel et al., 2016, Fig. 4). These experiments directly showed that RIM-BP2 deletion results in abnormal $Ca_v2.1$ clustering, while EM analysis revealed an intact overall synaptic ultrastructure (Grauel et al., 2016, Fig. S2). Functionally, we confirmed an increase in the coupling distance between Ca^{2+} channels and Ca^{2+} sensors for release using the slow membrane-permeable Ca^{2+} chelator EGTA-AM (Grauel et al., 2016, Fig. S6).

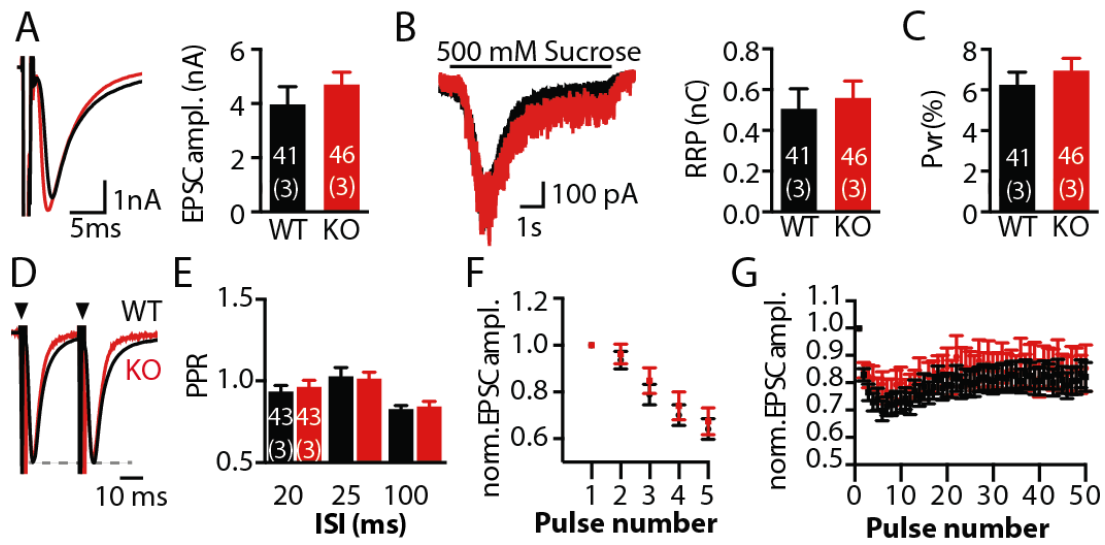


Figure 6 Deletion of RIM-BP1 does not affect evoked release in glutamatergic hippocampal neurons. (A) EPSC amplitudes (ampl.) of RIM-BP1 WT (black) and KO (red) autaptic neurons. (B) Size of the readily-releasable pool (RRP) of synaptic vesicles probed by hypertonic sucrose application. (C) Vesicular release probability (Pvr) of the same cells as in (A) and (B). (D) Normalized traces of two EPSCs at an interstimulus interval (ISI) of 25 ms. (E) Paired-pulse ratios (PPR) calculated for the indicated ISIs. (F) and (G) Normalized EPSC amplitudes of the same cells as in (E) in response to 5 APs triggered at 50Hz (F) and 50 APs triggered at 10 Hz (G). Unpublished data.

2. Research Article

Grauel, M.K., Magli **Grauel, M.K.**, Maglione, M., Reddy-Alla, S., Willmes, C.G., Brockmann, M.M., Trimbuch, T., Rosenmund, T., Pangalos, M., Vardar, G., Stumpf, A., Walter, A.M., Rost, B.R., Eickholt, B.J., Haucke, V., Schmitz, D., Sigrist, S.J., and Rosenmund, C. (2016). RIM-binding protein 2 regulates release probability by fine-tuning calcium channel localization at murine hippocampal synapses. *Proc. Natl. Acad. Sci. USA*, 113, 201605256.

DOI: <http://dx.doi.org/10.1073/pnas.1605256113>

PMID: 27671655

PMCID: [PMC5068320](https://www.ncbi.nlm.nih.gov/pmc/articles/PMC5068320/)

RIM-binding protein 2 regulates release probability by fine-tuning calcium channel localization at murine hippocampal synapses

M. Katharina Graue^{1a,b,c,1}, Marta Maglione^{b,c,d,1}, Suneel Reddy-Alla^{b,c,1}, Claudia G. Willmes^{b,e,f}, Marisa M. Brockmann^{a,b}, Thorsten Trimbach^{a,b}, Tanja Rosenmund^{a,b}, Maria Pangalos^{b,f}, Gülçin Vardar^{a,b}, Alexander Stumpf^{b,f}, Alexander M. Walter^g, Benjamin R. Rost^{b,f,h}, Britta J. Eickholt^{b,e}, Volker Haucke^{b,d,i}, Dietmar Schmitz^{b,f,h,2}, Stephan J. Sigrist^{b,c,2}, and Christian Rosenmund^{a,b,2}

^aInstitute of Neurophysiology, Charité Universitätsmedizin, 10117 Berlin, Germany; ^bNeuroCure Cluster of Excellence, Charité Universitätsmedizin, 10117 Berlin, Germany; ^cInstitute of Biology, Department of Biology, Chemistry, Pharmacy, Freie Universität Berlin, 14195 Berlin, Germany; ^dDepartment of Molecular Pharmacology and Cell Biology, Leibniz Institut für Molekulare Pharmakologie (FMP), 13125 Berlin, Germany; ^eInstitute of Biochemistry, Charité Universitätsmedizin, 10117 Berlin, Germany; ^fNeuroscience Research Center (NWFZ), Charité Universitätsmedizin, 10117 Berlin, Germany; ^gMolecular and Theoretical Neuroscience, Leibniz-Institut für Molekulare Pharmakologie, 10117 Berlin, Germany; ^hDZNE- German Center for Neurodegenerative Diseases, Charité Universitätsmedizin, 10117 Berlin, Germany; and ⁱInstitute of Chemistry and Biochemistry, Department of Biology, Chemistry, Pharmacy, Freie Universität Berlin, 14195 Berlin, Germany

Edited by Thomas C. Südhof, Stanford University School of Medicine, Stanford, CA, and approved August 15, 2016 (received for review March 31, 2016)

The tight spatial coupling of synaptic vesicles and voltage-gated Ca^{2+} channels (Ca_v s) ensures efficient action potential-triggered neurotransmitter release from presynaptic active zones (AZs). Rab-interacting molecule-binding proteins (RIM-BPs) interact with Ca^{2+} channels and via RIM with other components of the release machinery. Although human RIM-BPs have been implicated in autism spectrum disorders, little is known about the role of mammalian RIM-BPs in synaptic transmission. We investigated RIM-BP2-deficient murine hippocampal neurons in cultures and slices. Short-term facilitation is significantly enhanced in both model systems. Detailed analysis in culture revealed a reduction in initial release probability, which presumably underlies the increased short-term facilitation. Superresolution microscopy revealed an impairment in $\text{Ca}_v2.1$ clustering at AZs, which likely alters Ca^{2+} nanodomains at release sites and thereby affects release probability. Additional deletion of RIM-BP1 does not exacerbate the phenotype, indicating that RIM-BP2 is the dominating RIM-BP isoform at these synapses.

RIM-BP2 | calcium channel coupling | release probability | short-term plasticity | active zone structure

At the presynapse, coupling between action potentials (APs) and synaptic vesicle fusion is exquisitely precise, ensuring high temporal fidelity of neuron-to-neuron signaling in the nervous system. Two properties are thought to be responsible for this remarkable precision: a highly efficient release apparatus that transduces Ca^{2+} signals into vesicle fusion and a tightly organized active zone (AZ), where the release apparatus and voltage-gated Ca^{2+} channels (Ca_v s) are spatially coupled. Rab-interacting molecules (RIM) are thought to contribute to both properties, because loss of RIM impairs vesicle priming (1) and Ca_v localization at the AZ (2). RIM-binding proteins (RIM-BPs) directly interact with RIM (3), the pore-forming subunits of Ca_v1 and Ca_v2 channels (2, 4, 5), and Bassoon (5), and have therefore been suggested to play a role in presynaptic Ca_v localization. The *Drosophila* homolog of RIM-binding proteins (DRBP) is indeed crucial for neurotransmitter release at the AZ of neuromuscular junctions (NMJs) because loss of DRBP reduces Ca_v abundance and impairs the integrity of the AZ scaffold (6). DRBP-deficient flies show severe impairment of neurotransmitter release along with increased short-term facilitation (6, 7).

Recently, Acuna et al. (8) published a report on the combined loss of RIM-BP1 and RIM-BP2 in mouse synapses. The authors report that although RIM-BPs are not essential for synaptic transmission, AP-triggered neurotransmitter release is more variable and the sensitivity to the Ca^{2+} chelator EGTA is increased at the Calyx of Held, suggesting a larger coupling distance of Ca_v and the release machinery.

In the present study, we further investigated the consequences of constitutive deletion of RIM-BP2 on the structure and function of mouse hippocampal synapses. We show that loss of RIM-BP2 leads to a moderate reduction in initial release probability, which translates into profound changes in short-term plasticity (STP). This deficit can be overcome by increasing extracellular Ca^{2+} . We established triple-channel time-gated stimulated emission depletion (gSTED) microscopy for RIM-BP2, Munc13-1, and Bassoon, as well as for $\text{Ca}_v2.1$, RIM, and the postsynaptic marker protein Homer1. Using this technique, we demonstrate that although synapse number and molecular architecture appear essentially intact, RIM-BP2 is necessary for proper coclustering of the P/Q-type Ca_v subunit $\text{Ca}_v2.1$ with the AZ protein Bassoon at hippocampal CA3-CA1 synapses. We hypothesize that the observed change in Ca_v localization causes a discrete alteration in the coupling of Ca^{2+} influx and exocytosis, and thereby modifies release probability and, consequently, STP. Additional deletion of RIM-BP1 did not strengthen

Significance

Highly regulated and precise positioning of Ca^{2+} channels at the active zone (AZ) controls Ca^{2+} nanodomains at release sites. Their exact localization affects vesicular release probability (P_{VR}) and is important for proper synaptic transmission during repetitive stimulation. We provide a detailed analysis of synaptic transmission combined with superresolution imaging of the AZ organization in mouse hippocampal synapses lacking Rab-interacting molecule-binding protein 2 (RIM-BP2). By dual- and triple-channel time-gated stimulated emission depletion (gSTED) microscopy, we directly show that RIM-BP2 fine-tunes voltage-gated Ca^{2+} channel 2.1 ($\text{Ca}_v2.1$) localization at the AZ. We reveal that RIM-BP2 likely regulates the Ca^{2+} nanodomain by positioning $\text{Ca}_v2.1$ channels close to synaptic vesicle release sites. Loss of RIM-BP2 reduces P_{VR} and alters short-term plasticity.

Author contributions: M.K.G., M.M., S.R.-A., B.J.E., V.H., D.S., S.J.S., and C.R. designed research; M.K.G., M.M., S.R.-A., C.G.W., M.M.B., T.T., T.R., M.P., G.V., A.S., and B.R.R. performed research; A.M.W. contributed new reagents/analytic tools; M.K.G., M.M., S.R.-A., C.G.W., M.M.B., T.T., T.R., M.P., and B.R.R. analyzed data; A.M.W. provided data discussion; and M.K.G., M.M., S.R.-A., V.H., D.S., S.J.S., and C.R. wrote the paper.

The authors declare no conflict of interest.

This article is a PNAS Direct Submission.

Freely available online through the PNAS open access option.

¹M.K.G., M.M., and S.R.-A. contributed equally to this work.

²To whom correspondence may be addressed. Email: christian.rosenmund@charite.de, dietmar.schmitz@charite.de, or stephan.sigrist@fu-berlin.de.

This article contains supporting information online at www.pnas.org/lookup/suppl/doi:10.1073/pnas.1605256113/-DCSupplemental.

the changes in short-term facilitation, supporting our hypothesis that RIM-BP2 is the major RIM-BP paralog at glutamatergic hippocampal synapses.

Results

RIM-BP2 Localization at the AZ of Hippocampal CA3-CA1 Synapses. STED microscopy revealed that DRBP localizes close to the membrane near the AZ center of *Drosophila* NMJ synapses (6), but comparable studies on RIM-BPs at mammalian AZs with nanometer scale resolution are lacking. Quantitative real-time PCR suggested that RIM-BP2 is the predominant paralog in cultured hippocampal neurons (Fig. S14). We analyzed the spatial relationship between RIM-BP2 and two AZ components, Bassoon and MUNC13-1, at CA3-CA1 hippocampal synapses of mouse brain cryosections. On the confocal level, RIM-BP2 colocalized with both AZ proteins (Fig. S1B). To dissect the AZ nanoscale architecture, we established triple-channel gSTED with a lateral resolution of ~50 nm in all three channels (Fig. 1A and Fig. S1B–D). Analysis of the mean distance between nearest neighbors (*k*-nearest neighbor analysis) revealed that RIM-BP2 is localized at a short distance to Bassoon and MUNC13-1, whereas MUNC13-1 is equidistant to RIM-BP2 and Bassoon (*k* = 1). In coimmunoprecipitations from P2 fractions of mouse brains, RIM-BP2 coprecipitated with RIM and Munc13-1, but not with the Arf GTPase-activating protein GIT, a binding partner of Piccolo (9) and of endocytotic proteins such as Dynamin1 (Fig. S1E) and Stonin 2 (10). Together, these results indicate that RIM-BP2 is part of the presynaptic AZ scaffold and forms a complex with the priming factors RIM and Munc13-1.

Generation of a RIM-BP2 Constitutive Knockout Mouse Line. We generated knockout (KO) mice constitutively lacking RIM-BP2 by deleting exon 17 of the RIM-BP2 gene that encodes part of the second SH3 domain (Fig. S24). RIM-BP2-deficient mice were born at Mendelian ratios (Fig. S2B) and survived into adulthood. Complete loss of RIM-BP2 protein expression in KO animals was confirmed by immunostaining of hippocampal cryosections (Fig. S2C) and immunoblot analysis of P2 fractions using two antibodies targeting different RIM-BP2 epitopes (Fig. S2D and F). The expression of other presynaptic proteins such as RIM1/2, MUNC13-1, Erc1b/2, Synaptophysin1, and Synapsin1 was unaltered (Fig. S2D and E). Transmission electron microscopy showed that the ultrastructure of the presynaptic AZ was not grossly altered by the absence of RIM-BP2 (Fig. S2G–I).

RIM-BP2 Deletion Moderately Decreases Vesicular Release Probability and Leads to Increased Short-Term Facilitation in Cultured Neurons. To investigate the role of RIM-BP2 in synaptic transmission, we analyzed basic synaptic properties and STP in autaptic hippocampal glutamatergic neurons from RIM-BP2 WT and KO mice. Evoked excitatory postsynaptic current (EPSC) amplitudes were decreased by 20% in RIM-BP2 KO neurons compared with WT (Fig. 1B). We further analyzed the coefficient of variation (C.V.) of EPSCs as a measure for the reliability of evoked release. Consistent with previous results from RIM-BP1/2 double KOs (DKOs) (8), we found an increased C.V. in RIM-BP2 KO neurons (Fig. 1C). The size of the readily releasable pool (RRP) (11) was not significantly altered (Fig. 1D). The probability of a synaptic vesicle being released by an AP [vesicular release probability (P_{VR})] was calculated as the ratio of the EPSC and the RRP charge. P_{VR} was reduced by 10% in RIM-BP2 KO neurons (Fig. 1E). Additionally, we assessed release probability (P_R) by monitoring the progressive block of the NMDA receptor-mediated component of the EPSC by the noncompetitive NMDA receptor blocker (5S,10R)-(+)-5-methyl-10,11-dihydro-5H-dibenzo[*a,d*] cyclohepten-5,10-imine maleate (MK-801). The block rate, which is proportional to P_R (12), was indeed decreased by ~18% in RIM-BP2 KO neurons (Fig. S3A–C). Spontaneous miniature release, in contrast, was unaltered (Fig. 1F and G).

We next investigated how STP is affected by loss of RIM-BP2. Autaptic RIM-BP2 KO neurons showed a robust increase in paired-pulse ratio (PPR) when stimulated with pairs of APs at different interstimulus intervals (ISIs) compared with WT neurons

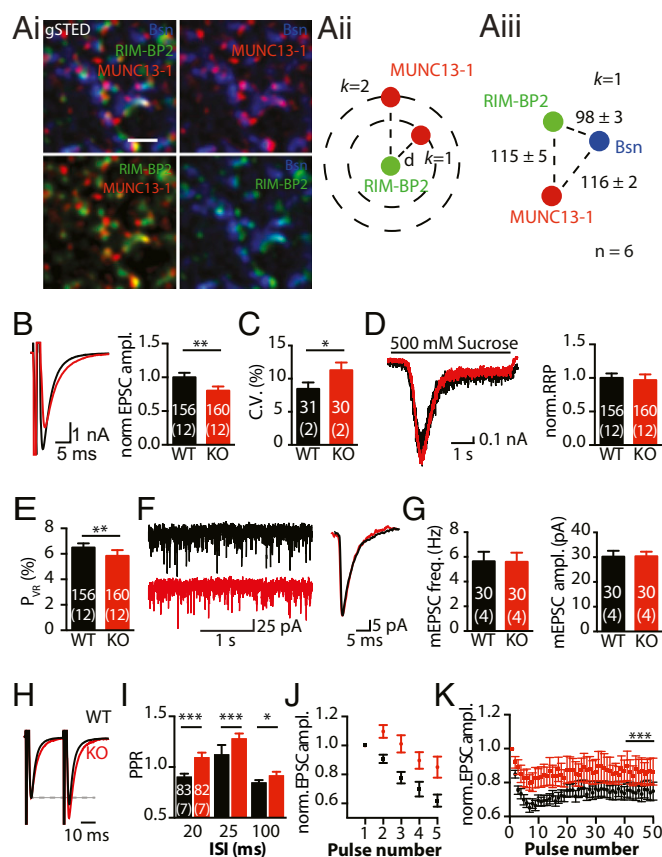


Fig. 1. RIM-BP2 localization at the hippocampal AZ, and effect of RIM-BP2 deletion on synaptic transmission in autaptic hippocampal neurons. (A, i–iii) Spatial organization of RIM-BP2 in relation to Bassoon (Bsn) and MUNC13-1 at the AZ of CA3-CA1 synapses in WT mouse brain cryosections imaged by gSTED and analyzed using the mean *k*-nearest neighbor distance between clusters. (Scale bar: 500 nm.) (B) EPSCs evoked by 2-ms somatic depolarization in RIM-BP2 WT (black) and KO (red) autaptic neurons. Amplitudes (ampl.) were normalized (norm.) to WT mean of the same culture. (C) C.V.s of 24 EPSC amplitudes recorded during a period of 2 min. (D) Synaptic responses to application of hypertonic sucrose (500 mM) solution probing the RRP. (E) P_{VR} of the same cells as in B and D. (F) Spontaneous release and averages of miniature EPSCs (mEPSCs) from the same cells. (G) mEPSC amplitudes and frequencies (freq.). (H) Normalized traces of two EPSCs at an ISI of 25 ms. (I) PPR calculated for the indicated ISIs. Normalized amplitudes of the same cells as in I in response to 5 APs triggered at 50 Hz (J) or 50 APs at 10 Hz (K). The last 10 EPSCs of the 10-Hz train are larger in KO neurons compared with WT. The numbers of neurons and independent cultures analyzed are shown within the bars. Data are expressed as mean \pm SEM. * P < 0.05; ** P < 0.01; *** P < 0.001.

(Fig. 1H and I). During short bursts of five APs at 50 Hz (Fig. 1J), EPSCs showed initial facilitation, followed by moderate depression in RIM-BP2 KO neurons but significant depression in WT neurons. Similarly, RIM-BP2 KO neurons exhibited significantly reduced depression of EPSC amplitudes during 10-Hz trains compared with WT neurons (Fig. 1K).

RIM-BP2 Deletion Alters STP in Acute Hippocampal Slices. To verify the results independently in autaptic culture, we analyzed synaptic transmission in the CA1 area of acute hippocampal slices. The input/output function relating field recordings of excitatory postsynaptic potentials (fEPSPs) and fiber volley amplitudes were unchanged (Fig. 2A), suggesting that the loss of RIM-BP2 does not cause major alterations in basal synaptic transmission.

However, the PPR of fEPSPs was significantly elevated for all ISIs (Fig. 2B and C), corroborating the cell culture results. Train stimulations with 25 pulses at 14 Hz caused greater initial facilitation and

less depression of fEPSPs in RIM-BP2 KO compared with WT mice (Fig. 2D). As in autaptic cultures, spontaneous miniature release was unaltered in hippocampal slices (Fig. 2E). Together, the data from acute slices and autaptic culture demonstrate enhanced short-term facilitation in the absence of RIM-BP2.

Additional RIM-BP1 Deletion Does Not Exacerbate the RIM-BP2 KO Phenotype. We crossed RIM-BP2 KO mice with constitutive RIM-BP1 KO mice (Fig. S4A–F) to generate RIM-BP1/2 DKO mice. In area CA1 of acute hippocampal slices, input/output functions of RIM-BP2 KO and RIM-BP1/2 DKO were indistinguishable (Fig. S4G). We then compared PPRs (Fig. S4H) and STP (Fig. S4I) in RIM-BP2 single-KO and RIM-BP1/2 DKO slices. Additional deletion of RIM-BP1 did not exacerbate the increased facilitation observed in the single RIM-BP2 KO. Thus, our data support the hypothesis that RIM-BP2 is the major RIM-BP paralog in murine hippocampal neurons.

RIM-BP2 Deletion Does Not Affect Vesicle Priming or Replenishment. RIM and Munc13 are known to mediate priming of synaptic vesicles (1, 13). Thus, could the increased short-term facilitation be caused by RIM-BP2 modulating priming through its interactions with the RIM/Munc13-1 complex? We can exclude this possibility for several reasons. First, the unaltered spontaneous release (Figs. 1G and 2E and Fig. S3G) argues against a priming defect in RIM-BP2 KO synapses (14). Second, the transmitter release induced by sub-saturating hypertonic stimulation (250 mM sucrose) compared with release induced by a saturating stimulus (500 mM sucrose) was identical in autaptic RIM-BP2 WT and KO neurons, indicating no difference in vesicle fusogenicity (14) (Fig. S3D and E). Third, due to a higher energy barrier for fusion, sucrose-induced release kinetics would be slower in the case of a priming deficit (15). However, peak release rates were unchanged (Fig. S3F). Additionally, we tested recovery from pool depletion but did not detect any difference between WT and RIM-BP2 KO neurons (Fig. S3H and I), suggesting that RIM-BP2 deletion does not affect RRP replenishment.

RIM-BP2 Deletion Alters Ca^{2+} Sensitivity of Release. Work at *Drosophila* NMJ synapses demonstrated that deletion of DRBP results in defective Ca_v localization, reduced Ca^{2+} influx, impaired synaptic transmission, and increased short-term facilitation (6). We examined presynaptic Ca^{2+} influx in cultured hippocampal neurons using the fast Ca^{2+} sensor GCamp6f coupled to synaptophysin (SynG-Camp6f) that specifically localizes the sensor to the presynapse (Fig.

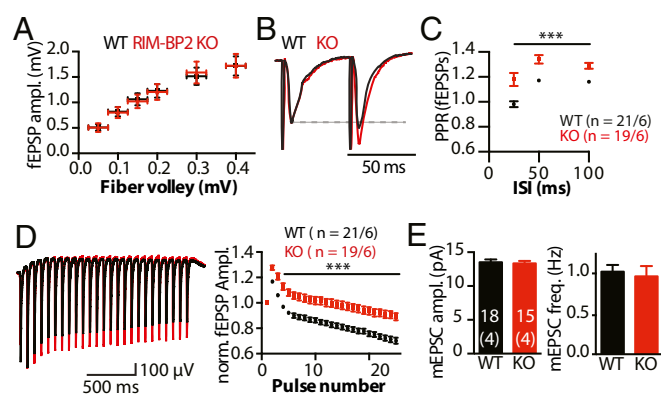


Fig. 2. RIM-BP2 deletion alters STP in acute hippocampal slices. (A) Input/output curves relating the amplitude of the presynaptic fiber volley to the fEPSP amplitude in the stratum radiatum of area CA1 of acute hippocampal slices at different stimulus intensities (0.05 mV–0.2 mV: WT, $n = 21$; KO, $n = 19$; 0.3 mV: WT, $n = 18$; KO, $n = 14$; 0.4 mV: WT, $n = 16$; KO, $n = 13$). (B) Normalized fEPSPs in response to a paired pulse with 50-ms ISI. (C) PPRs of fEPSPs at different ISIs. (D) fEPSPs elicited by a 14-Hz stimulation train, with stimulation artifacts blanked for better visibility. (E) mEPSC amplitudes and frequencies recorded from CA1 pyramidal neurons. The numbers of slices and independent animals are indicated. Data are expressed as mean \pm SEM. *** $P < 0.001$.

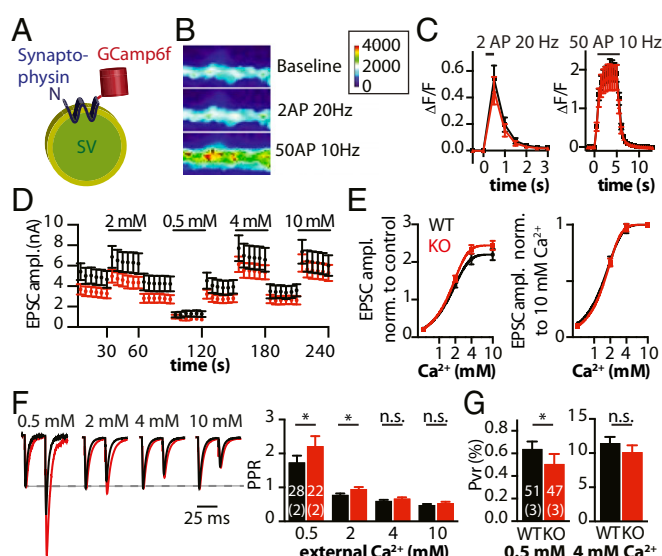


Fig. 3. RIM-BP2 deletion alters Ca^{2+} sensitivity of release. (A) Schematic representation of the genetically encoded Ca^{2+} indicator synG-Camp6f at the membrane of a synaptic vesicle. Heat-colored images of a WT dendrite (B) and quantification of synG-Camp6f fluorescence change ($\Delta F/F$) during stimulation with two APs at 20 Hz and 50 APs at 10 Hz (C). (D) Mean EPSCs of WT (black) and RIM-BP2 KO (red) autaptic neurons in different $[\text{Ca}^{2+}]_{\text{ext}}$. The $[\text{Ca}^{2+}]_{\text{ext}}$ s of test solutions are indicated (all 1 mM Mg^{2+}). A control solution (2 mM Ca^{2+} /4 mM Mg^{2+}) was applied in between. (E) EPSC amplitudes at different $[\text{Ca}^{2+}]_{\text{ext}}$ s normalized to alternating control responses (Left) and to 10 mM $[\text{Ca}^{2+}]_{\text{ext}}$ (Right). Hill functions were fitted to the data. (F) Normalized EPSCs in response to a paired stimulus and mean PPRs at indicated $[\text{Ca}^{2+}]_{\text{ext}}$. (G) P_{VR} of autaptic hippocampal neurons in 0.5 mM and 4 mM $[\text{Ca}^{2+}]_{\text{ext}}$. The numbers of neurons and independent cultures analyzed are shown within the bars. Data are expressed as mean \pm SEM. * $P < 0.05$. n.s., not significant.

34). We did not detect significant differences in global Ca^{2+} signals in response to two (at 20 Hz) or 50 (at 10 Hz) APs (Fig. 3B and C). Furthermore, we analyzed the dependence of transmitter release on varying external Ca^{2+} concentrations ($[\text{Ca}^{2+}]_{\text{ext}}$ s) in RIM-BP2 WT and KO autaptic neurons in detail (Fig. 3D and E). The relative sensitivity of EPSC amplitudes to varying $[\text{Ca}^{2+}]_{\text{ext}}$ s (0.5–10 mM Ca^{2+} /1 mM Mg^{2+}) was determined by intermittent measurements of EPSC amplitudes from control solution (2 mM Ca^{2+} /4 mM Mg^{2+} ; Fig. 3D). Normalizing to control EPSCs, we found that the relative potentiation of release is increased in RIM-BP2 KO at 4 mM and 10 mM $[\text{Ca}^{2+}]_{\text{ext}}$ s (Fig. 3E, Left). To fit a Hill function, we normalized the same dataset to saturating 10 mM $[\text{Ca}^{2+}]_{\text{ext}}$, resulting in almost identical Ca^{2+} dose-response curves for WT and KO neurons (Fig. 3E, Right), suggesting no change in the Ca^{2+} cooperativity n for release and similar numbers of Ca_v s at the AZ of both genotypes. These findings, however, do not exclude changes in residual Ca^{2+} at local micro- or nanodomains in the RIM-BP2 KO.

We next determined PPRs at different $[\text{Ca}^{2+}]_{\text{ext}}$ s (Fig. 3F). In 0.5–2 mM $[\text{Ca}^{2+}]_{\text{ext}}$, PPRs (25-ms ISI) were significantly increased in RIM-BP2 KO neurons, whereas PPRs were indistinguishable in 4–10 mM $[\text{Ca}^{2+}]_{\text{ext}}$. In a second set of experiments, we analyzed PPRs at different ISIs (25–250 ms) and found similar results for all chosen ISIs (Fig. S3J). PPRs were significantly increased in lower $[\text{Ca}^{2+}]_{\text{ext}}$ s (≤ 2 mM) and also for ISIs up to 250 ms with the exception of 0.5 mM $[\text{Ca}^{2+}]_{\text{ext}}$, where PPRs at 100 ms and 250 ms were identical in WT and RIM-BP2 KO. Overall, the differences in PPRs became smaller with increasing $[\text{Ca}^{2+}]_{\text{ext}}$. At 4 mM $[\text{Ca}^{2+}]_{\text{ext}}$, only the PPR values recorded at 50-ms and 250-ms ISIs were significantly increased in RIM-BP2 KO neurons.

We also measured P_{VR} at low and high $[\text{Ca}^{2+}]_{\text{ext}}$ s and found that in 0.5 mM $[\text{Ca}^{2+}]_{\text{ext}}$, P_{VR} was reduced by 21% in RIM-BP2 KO neurons (Fig. 3G), whereas the difference in 4 mM $[\text{Ca}^{2+}]_{\text{ext}}$ was not significant. Similarly, RIM-BP2 KO had significantly reduced

EPSC amplitudes, accompanied by an increased C.V. of the EPSCs in low, but not high, $[Ca^{2+}]_{ext}$ (Fig. S3K).

Altogether, these data show that loss of RIM-BP2 leads to an impairment of Ca^{2+} -secretion coupling that can be overcome by elevating $[Ca^{2+}]_{ext}$.

RIM-BP2 KO Alters Presynaptic $Ca_v2.1$ Channel Localization. If priming, global presynaptic Ca^{2+} influx, and Ca^{2+} cooperativity are unaltered in the RIM-BP2 KO neurons, could altered Ca_v positioning explain the changes in release probability and PPR?

To address this question, we turned to superresolution microscopy and tested if deletion of RIM-BP2 alters the subsynaptic positioning of the P/Q-type Ca_v subunit $Ca_v2.1$, because interference with RIM-BP2 and Bassoon interaction affects their synaptic localization (5). We first measured the synaptic distribution of $Ca_v2.1$ s in relation to the AZ protein Bassoon in the stratum radiatum of the hippocampal area CA1 of WT and RIM-BP2 KO mice by dual-channel gSTED (Fig. 4 A–F). We found that loss of RIM-BP2 did not significantly affect either the total number of $Ca_v2.1$ and Bassoon clusters or their ratio (Fig. S5 A and B), in agreement with the unaltered total Ca^{2+} influx observed

by Ca^{2+} imaging (Fig. 3 A–C). Notably, however, the average number of Bassoon clusters at short distance intervals from $Ca_v2.1$ clusters was significantly reduced by more than 30% (Fig. 4 B, i and C). This finding indicates that RIM-BP2 deletion alters $Ca_v2.1$ localization at short distances from the AZ. This effect is not due to an overall change in total cluster number. Supporting these results, at RIM BP2 KO synapses, we observed a 50% increase in the mean k distance of Bassoon clusters surrounding a given $Ca_v2.1$ cluster, but the P value reached was only 0.068 ($k = 1$; Fig. 4 B, ii and D). The mean k distance between individual Bassoon clusters did not significantly change in the absence of RIM-BP2, suggesting that although the distance between single AZs is unaltered in RIM-BP2 KO mice, $Ca_v2.1$ s are localized more distal from the AZ (Fig. 4 E and F).

To map $Ca_v2.1$ localization precisely relative to the AZ protein RIM1 and the postsynaptic marker Homer1, we established triple-channel gSTED (Fig. 4 G–N). The total number of $Ca_v2.1$, RIM1, and Homer1 clusters did not significantly differ between WT and RIM-BP2 KO (Fig. S5 C–E). However, RIM-BP2 KO mice showed higher variability in RIM1 cluster number as expressed in a highly variable RIM1/ $Ca_v2.1$ ratio (Fig. S5 D and E). This

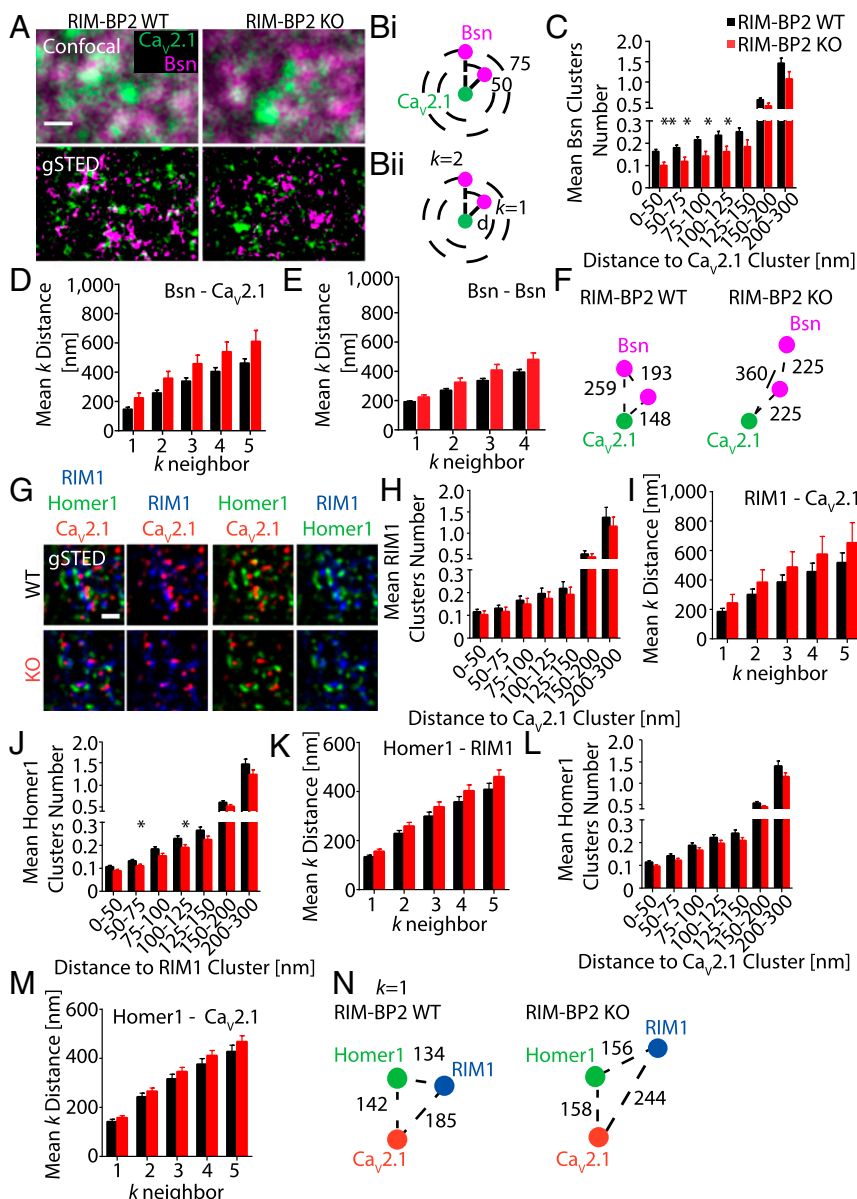


Fig. 4. RIM-BP2 loss results in defective $Ca_v2.1$ clustering at the AZ. (A) $Ca_v2.1$ and Bsn clusters imaged in situ at CA3-CA1 hippocampal synapses of RIM-BP2 WT and KO mice by dual-channel gSTED (Bottom) compared with confocal acquisition (Top). (B) Schematic representation of two kinds of cluster analysis. (B, i) Bsn clusters within indicated sampling distances (e.g., 50 nm, 75 nm) to a given $Ca_v2.1$ cluster were quantified and averaged on thousands of $Ca_v2.1$ clusters per image. (B, ii) Mean distance between the k -nearest neighbor Bsn cluster and $Ca_v2.1$ cluster ($k = 1, k = 2, k = 3, k = 4, k = 5$). (C) Bsn cluster numbers at short distances from $Ca_v2.1$ clusters (WT, $n = 5$; KO, $n = 6$). (D–F) Mean k distance between Bsn and $Ca_v2.1$ clusters (D) and between neighboring Bsn clusters (E) in RIM-BP2 KO mice. (G) Triple-channel gSTED images of $Ca_v2.1$, RIM1, and Homer1 at CA3-CA1 hippocampal synapses (WT, $n = 9$; KO, $n = 9$). (H) RIM1 clusters found in proximity to $Ca_v2.1$ channels. (I) Mean k distance of RIM1 clusters to $Ca_v2.1$ clusters. Homer1-RIM1 clustering (J) and Homer1-RIM1 mean k distance (K). Homer1 clusters close to $Ca_v2.1$ channels (L), and mean k distances between Homer1 clusters and $Ca_v2.1$ (M) are shown. (N) $Ca_v2.1$ spatial organization relative to RIM1 and Homer1 at excitatory hippocampal synapses. (Scale bars: A and G, 500 nm.) Distances between clusters are represented in nanometers. Values are expressed as mean \pm SEM. * $P < 0.05$; ** $P < 0.01$.

variability did not affect net RIM1 clustering relative to $\text{Ca}_v2.1$ s, although we also observed a trend here toward increased mean k distance of RIM1 surrounding $\text{Ca}_v2.1$ clusters (Fig. 4 *H* and *I*). We also found a significantly reduced mean number of Homer1 clusters surrounding a given RIM1 cluster at 50–75 nm and 100–125 nm in RIM-BP2 KO (Fig. 4*J*), suggesting an effect of RIM-BP2 on RIM1 clustering. However, the mean k distance of neighboring Homer1 toward RIM1 clusters did not significantly change (Fig. 4*K*). These data indicate that RIM-BP2 might exert a minor effect on the exact RIM1 spatial distribution at the AZ. The mean number of Homer1 clusters relative to $\text{Ca}_v2.1$ was not altered in RIM-BP2 KO (Fig. 4*L*). At RIM-BP2 WT synapses, the closest neighboring Homer1 cluster was found at 142 ± 10 nm from $\text{Ca}_v2.1$ clusters (Fig. 4 *M* and *N*). In RIM-BP2 KO, this distance increased by 11% with a statistical P value at the edge of significance ($P = 0.05$), demonstrating that RIM-BP2 deletion does not grossly alter $\text{Ca}_v2.1$ positioning versus the postsynaptic density.

Our structural analysis shows that loss of RIM-BP2 modifies the molecular architecture of the AZ by changing the relative distribution of $\text{Ca}_v2.1$ s versus the AZ scaffold protein Bassoon. Increased distance should result in a larger functional coupling distance between the Ca^{2+} channel and Ca^{2+} sensor, and therefore a stronger effect of the slow Ca^{2+} chelator EGTA (16). Thus, we tested whether application of the membrane-permeable EGTA acetoxymethyl ester (EGTA-AM) would have differential effects on EPSC amplitudes and P_{VR} of WT and RIM-BP2 KO autaptic neurons (Fig. S6 *A–C*). Indeed, preincubation with 25 μM EGTA-AM decreased EPSC amplitudes more in RIM-BP2 KO than in WT (Fig. S6*D*). Although this effect was not statistically significant, EGTA-AM did reduce P_{VR} by more than 50% in RIM-BP2 KO without altering WT P_{VR} (Fig. S6*B*). Thus, together with our structural data, the EGTA-AM effect on P_{VR} in RIM-BP2 KO neurons supports the idea of a larger distance between Ca^{2+} channels and Ca^{2+} sensors at release sites in the absence of RIM-BP2. Our analysis provides evidence that RIM-BP2 contributes to proper positioning of $\text{Ca}_v2.1$ s at AZs of hippocampal glutamatergic synapses that allows precise Ca^{2+} -secretion coupling.

Discussion

Presynaptic neurotransmitter release is a highly orchestrated process ensuring high-fidelity neuronal communication. The RIM/RIM-BP complex has been implicated in enhancing the efficiency of the fusion machinery and the positioning of synaptic vesicles in close proximity to Ca_v s to optimize Ca^{2+} -secretion coupling (2, 5, 6). Recently, Acuna et al. (8) showed that deletion of RIM-BP1 and RIM-BP2 in the murine Calyx of Held impairs the reliability of evoked neurotransmitter release, presumably due to an uncoupling of Ca_v s from release sites. At the *Drosophila* NMJ, the RIM-BP ortholog DRBP, together with Bruchpilot, is an AZ core component, and elimination of DRBP causes severe structural deficits in AZ organization, associated with strongly impaired basal transmission and STP (6, 7).

Our analysis of the RIM-BP2 KO in glutamatergic hippocampal neurons revealed a moderate disruption of the AZ architecture in comparison to the *Drosophila* phenotype, resulting in a mild decrease in release efficiency but a pronounced alteration in STP. Thus, rather subtle modifications in the fine positioning of the Ca_v s within the AZ are sufficient to promote changes in release probability and induce robust STP alterations.

The altered P_{VR} , PPR, and STP of RIM-BP2-deficient neurons are most plausibly explained by changes in the nanoscale organization of protein architectures within the AZs (i.e., the mislocalization of $\text{Ca}_v2.1$ s in proximity to Bassoon). We interpret these results as an indication of increased coupling distances between Ca^{2+} channels and release sites, also based on our EGTA-AM experiments. These data are also consistent with previously published results (5, 8). A larger distance between $\text{Ca}_v2.1$ s and release sites would result in an altered local Ca^{2+} profile “seen” by the Ca^{2+} sensor for release, which determines vesicle fusion and strongly depends on the coupling distance (17). RIM-BPs have been identified in a number of studies as candidate genes for autism spectrum disorder (ASD) (18–

21). Although neurons might be able to compensate for the 10% decrease in P_{VR} by homeostatic mechanisms, it is likely that the robust changes in STP might ultimately severely alter the computational properties and function of the affected neuronal networks, and thereby perturb synaptic information processing (22).

It should be noted that a very similar phenotype with mildly reduced P_{VR} and robustly increased short-term facilitation is also evident in Ras-related protein Rab3-deficient neurons (23). Schlüter et al. (23) speculate that Rab3 “superprimes” a subset of vesicles, specifically increasing their release probability. One possible mechanism is that Rab3 directs vesicles to release sites closer to Ca^{2+} channels, where they would have an intrinsically higher release probability. This scenario might explain the similarities in both phenotypes. Whereas Rab3 would control coupling of synaptic vesicles and Ca^{2+} channels from the vesicle side, RIM-BP2 might act from the Ca^{2+} channel side in a subset of AZs. Indeed, in our analysis, we see only a relatively small fraction of AZs having a $\text{Ca}_v2.1$ within 125 nm. At this subset of AZs, proper $\text{Ca}_v2.1$ localization depends on RIM-BP2.

We established triple-channel gSTED to determine precise distances between clusters of specific synaptic components at CA3-CA1 synapses in situ. At other excitatory synapses, previous studies using direct stochastic optical reconstruction microscopy (dSTORM) reported a Bassoon-Homer1 average axial distance of 154 nm (24). Accordingly, we find that at WT synapses, Homer1 is located at 142 nm and 134 nm from $\text{Ca}_v2.1$ and RIM1, respectively, indicating that gSTED can be used reliably to map protein cluster localization, and thus synaptic substructures at mammalian synapses in situ. However, with both superresolution techniques, true cluster distances are obviously influenced by using indirect immunolabeling, because the size of the primary/secondary IgG sandwich (~ 20 nm) and the position of the epitopes recognized by the antibodies likely influence the exact measured distances (epitopes targeted by each antibody are listed in Table S1). Still, comparing the values between mutant and WT constellation should be meaningful.

Here, we show that at hippocampal CA3-CA1 AZs, RIM-BP2 is located close to Bassoon and Munc13-1 in a complex in which each nearest neighbor is rather equidistant (~ 100 nm). According to ultrastructural studies, cortical pyramidal neuron synapses usually have a single AZ with a highly variable area of about $0.04 \mu\text{m}^2$ (25, 26). Our cluster analysis at CA3-CA1 synapses maps two adjacent Bassoon clusters at less than 200 nm. We therefore assume that the first ($k = 1$) nearest neighbor of our analysis might indicate a neighboring cluster within a single AZ. To address this point more precisely, 3D reconstruction of AZ components imaged at subdiffraction axial resolution will be necessary. Our data also show that the localization of $\text{Ca}_v2.1$ in close apposition to the PSD marker Homer1 is relatively stable even in the absence of RIM-BP2. Although the overall RIM1 expression level was not affected in crude synaptosomal membranes, we observed increased variability in RIM1 total cluster number in RIM-BP2-deficient synapses. This increased variability may reflect altered nanoscale distribution of RIM1 localization within AZs and toward the postsynapse, which is supported by a trend toward a larger RIM1-to- $\text{Ca}_v2.1$ mean k distance and slightly, but significantly, altered Homer1 clustering relative to RIM1 in RIM-BP2 KO.

We performed a detailed analysis of RIM-BP2 loss of function mostly in autaptic neurons, whereas our structural analysis was done in situ to provide information on the organization of the AZ within the hippocampus. Nevertheless, our PPR and STP experiments in slices demonstrate that RIM-BP2 KO results in a similar functional defect in both preparations. On the other hand, our EGTA-AM experiments provide evidence that RIM-BP2 is necessary for proper Ca^{2+} channel localization at the AZ also in vitro.

Besides coupling of Ca_v s to release sites, other functions have been suggested for RIM-BPs. At the *Drosophila* NMJ, DRBP is required for homeostatic modulation of presynaptic Ca^{2+} influx and the size of the RRP, as well for as recovery from pool depletion (7). In contrast, at the murine Calyx of Held, RRP size and the kinetics of priming into the RRP are not RIM-BP-dependent

(8). However, the release of the RRP was significantly decelerated in RIM-BP1/2 DKO. In our autaptic culture system, we observed no differences in RRP size, fusogenicity, or peak release rates, and we did not detect changes in the recovery from pool depletion. These results suggest that loss of RIM-BPs manifests distinctively at different specialized synapse types.

Why are the effects of RIM-BP2 deletion on presynaptic structure and function of hippocampal synapses rather subtle compared with the severe phenotype at *Drosophila* NMJ AZs? Differences in the exact structure of the AZ scaffolds and the level of genetic redundancy might well be involved here. In fact, different isoforms of AZ proteins likely contribute to shaping specific functions that differ from synapse to synapse. For both hippocampal and NMJ synapses, however, the RIM/RIM-BP complex is crucial for precise Ca_v localization at the AZ and expression of STP and/or long-term plasticity. The comparison of KO phenotypes suggests that in *Drosophila*, DRBP plays a more pivotal role (6, 27), whereas judged from single gene KOs at mammalian synapses, RIM is functionally most important (1, 2, 8, 28–30). Still, the importance of RIM-BPs for STP is conserved between flies and mammals (6, 8, 31), consistent with the highly conserved molecular interactions between RIM-BPs, Ca_v s, and RIM (2, 4, 6).

Further investigation is required to understand fully the molecular role of RIM-BPs in different synapse types, which might also depend on the type of presynaptic Ca_v present. Studying potential behavioral deficits in RIM-BP1 and RIM-BP2 KO mice and the function of RIM-BPs in neuronal circuits implicated in ASD (32) will likely advance our understanding of how the disruption of RIM-BP function might lead to behavioral and cognitive deficits.

Methods

KO Mouse Generation. RIM-BP2 and RIM-BP1 targeting vector construction and KO mouse generation by standard homologous recombination were performed by genOway. All animal experiments were approved by the animal welfare committee of Charité Universitätsmedizin Berlin and the Landesamt für Gesundheit und Soziales Berlin.

- Deng L, Kaeser PS, Xu W, Südhof TC (2011) RIM proteins activate vesicle priming by reversing autoinhibitory homodimerization of Munc13. *Neuron* 69(2):317–331.
- Kaeser PS, et al. (2011) RIM proteins tether Ca^{2+} channels to presynaptic active zones via a direct PDZ-domain interaction. *Cell* 144(2):282–295.
- Wang Y, Sugita S, Südhof TC (2000) The RIM/NIM family of neuronal C2 domain proteins. Interactions with Rab3 and a new class of Src homology 3 domain proteins. *J Biol Chem* 275(26):20033–20044.
- Hibino H, et al. (2002) RIM binding proteins (RBPs) couple Rab3-interacting molecules (RIMs) to voltage-gated Ca^{2+} channels. *Neuron* 34(3):411–423.
- Davydova D, et al. (2014) Bassoon specifically controls presynaptic P/Q-type Ca^{2+} channels via RIM-binding protein. *Neuron* 82(1):181–194.
- Liu KSY, et al. (2011) RIM-binding protein, a central part of the active zone, is essential for neurotransmitter release. *Science* 334(6062):1565–1569.
- Müller M, Genç Ö, Davis GW (2015) RIM-binding protein links synaptic homeostasis to the stabilization and replenishment of high release probability vesicles. *Neuron* 85(5):1056–1069.
- Acuna C, Liu X, Gonzalez A, Südhof TC (2015) RIM-BPs mediate tight coupling of action potentials to Ca^{2+} -triggered neurotransmitter release. *Neuron* 87(6):1234–1247.
- Kim S, et al. (2003) The GIT family of proteins forms multimers and associates with the presynaptic cytomatrix protein Piccolo. *J Biol Chem* 278(8):6291–6300.
- Podufall J, et al. (2014) A presynaptic role for the cytomatrix protein GIT in synaptic vesicle recycling. *Cell Reports* 7(5):1417–1425.
- Rosenmund C, Stevens CF (1996) Definition of the readily releasable pool of vesicles at hippocampal synapses. *Neuron* 16(6):1197–1207.
- Rosenmund C, Clements JD, Westbrook GL (1993) Nonuniform probability of glutamate release at a hippocampal synapse. *Science* 262(5134):754–757.
- Varoqueaux F, et al. (2002) Total arrest of spontaneous and evoked synaptic transmission but normal synaptogenesis in the absence of Munc13-mediated vesicle priming. *Proc Natl Acad Sci USA* 99(13):9037–9042.
- Arancillo M, et al. (2013) Titration of Syntaxin1 in mammalian synapses reveals multiple roles in vesicle docking, priming, and release probability. *J Neurosci* 33(42):16698–16714.
- Basu J, Betz A, Brose N, Rosenmund C (2007) Munc13-1 C1 domain activation lowers the energy barrier for synaptic vesicle fusion. *J Neurosci* 27(5):1200–1210.
- Eggermann E, Bucurenciu I, Goswami SP, Jonas P (2011) Nanodomain coupling between Ca^{2+} channels and sensors of exocytosis at fast mammalian synapses. *Nat Rev Neurosci* 13(1):7–21.
- Nadkarni S, Bartol TM, Stevens CF, Sejnowski TJ, Levine H (2012) Short-term plasticity constrains spatial organization of a hippocampal presynaptic terminal. *Proc Natl Acad Sci USA* 109(36):14657–14662.
- Bucan M, et al. (2009) Genome-wide analyses of exonic copy number variants in a family-based study point to novel autism susceptibility genes. *PLoS Genet* 5(6):e1000536.

Cell Culture and Electrophysiological Recordings. Primary neuronal cultures were prepared as described by Arancillo et al. (14). Whole-cell patch-clamp recordings in autaptic neurons were performed at days in vitro 13–21 as described (14).

Slice Preparation and Electrophysiological Recordings. Acute hippocampal slices were prepared as described by Stempel et al. (33). The 300- μm -thick horizontal slices were maintained for 30 min at 35 °C in sucrose-artificial cerebrospinal fluid (ACSF) and subsequently stored in ACSF at room temperature. Experiments were started after 30 min and no longer than 6 h after preparation. A detailed description of electrophysiological experiments is provided in *SI Methods*.

Immunohistochemical Analysis and gSTED Imaging. Following immunostaining, sagittal cryosections (10 μm) of RIM-BP2 WT and KO brains were imaged by gSTED with a Leica SP8 gSTED microscope (Leica Microsystems) equipped with two depletion lasers (592 nm and 775 nm). Cluster analysis on deconvolved images was performed with Amira (Visualization Sciences Group) and a MATLAB (The MathWorks, Inc.) custom-written script.

SynGComp6f Imaging. SynGComp6f was generated analogous to synGComp2 (34) by fusing GCamp6f (35) to the C terminus of the synaptic vesicle protein synaptophysin. Imaging was done as previously described (34).

SI Methods contains figures, a detailed description of the methods used, antibodies (Table S1), raw values, and statistical analysis (Tables S2–S4).

ACKNOWLEDGMENTS. We thank Annegret Felies, Berit Soehl-Kielczynski, Sabine Lenz, Katja Poetschke, Carola Schweynoch, Rike Dannenberg, and Bettina Brokowski for technical support; and Lauren Mamer for discussions. We thank Burkhard Wiesner and Martin Lehmann (FMP cellular imaging facility) for the use of the Leica gSTED microscope and for the fluorescent beads; Andreas Grasskamp for the point spread function estimation by Gaussian fit; Anna Fejtova and Eckart Gundelfinger for the RIM-BP2 antibody; and Pietro De Camilli for the Dynamin1 antibody. This work was supported by the Deutsche Forschungsgemeinschaft (Collaborative Research Grant SFB 958 [to V.H. (A1, A7), D.S. (A5), S.S. (A3, A6), C.R. (A5)] and Emmy-Noether Program (to A.M.W.), Studienstiftung des deutschen Volkes PhD Fellowship (to M.K.G.), and Excellence Cluster NeuroCure Exc257 (to B.J.E., V.H., D.S., S.S., and C.R.).

- Pinto D, et al. (2010) Functional impact of global rare copy number variation in autism spectrum disorders. *Nature* 466(7304):368–372.
- Hussman JP, et al. (2011) A noise-reduction GWAS analysis implicates altered regulation of neurite outgrowth and guidance in autism. *Mol Autism* 2(1):1.
- Corominas R, et al. (2014) Protein interaction network of alternatively spliced isoforms from brain links genetic risk factors for autism. *Nat Commun* 5:3650.
- Klyachko VA, Stevens CF (2006) Excitatory and feed-forward inhibitory hippocampal synapses work synergistically as an adaptive filter of natural spike trains. *PLoS Biol* 4(7):e207.
- Schlüter OM, Basu J, Südhof TC, Rosenmund C (2006) Rab3 superprimed synaptic vesicles for release: Implications for short-term synaptic plasticity. *J Neurosci* 26(4):1239–1246.
- Dani A, Huang B, Bergan J, Dulac C, Zhuang X (2010) Superresolution imaging of chemical synapses in the brain. *Neuron* 68(5):843–856.
- Schikorski T, Stevens CF (1997) Quantitative ultrastructural analysis of hippocampal excitatory synapses. *J Neurosci* 17(15):5858–5867.
- Holderith N, et al. (2012) Release probability of hippocampal glutamatergic terminals scales with the size of the active zone. *Nat Neurosci* 15(7):988–997.
- Graf ER, et al. (2012) RIM promotes calcium channel accumulation at active zones of the *Drosophila* neuromuscular junction. *J Neurosci* 32(47):16586–16596.
- Schoch S, et al. (2002) RIM1 α forms a protein scaffold for regulating neurotransmitter release at the active zone. *Nature* 415(6869):321–326.
- Castillo PE, Schoch S, Schmitz F, Südhof TC, Malenka RC (2002) RIM1 α is required for presynaptic long-term potentiation. *Nature* 415(6869):327–330.
- Kintscher M, Wozny C, Jochenning FW, Schmitz D, Breustedt J (2013) Role of RIM1 α in short- and long-term synaptic plasticity at cerebellar parallel fibres. *Nat Commun* 4:2392.
- Müller M, Liu KSY, Sigrist SJ, Davis GW (2012) RIM controls homeostatic plasticity through modulation of the readily-releasable vesicle pool. *J Neurosci* 32(47):16574–16585.
- Courchesne E, et al. (2007) Mapping early brain development in autism. *Neuron* 56(2):399–413.
- Stempel AV, et al. (2016) Cannabinoid type 2 receptors mediate a cell type-specific plasticity in the hippocampus. *Neuron* 90(4):795–809.
- Herman MA, Ackermann F, Trimbuch T, Rosenmund C (2014) Vesicular glutamate transporter expression level affects synaptic vesicle release probability at hippocampal synapses in culture. *J Neurosci* 34(35):11781–11791.
- Chen T-W, et al. (2013) Ultrasensitive fluorescent proteins for imaging neuronal activity. *Nature* 499(7458):295–300.
- Watanabe S, et al. (2014) Clathrin regenerates synaptic vesicles from endosomes. *Nature* 515(7526):228–233.
- Clements JD, Bekkers JM (1997) Detection of spontaneous synaptic events with an optimally scaled template. *Biophys J* 73(1):220–229.
- Xue M, et al. (2010) Binding of the complexin N terminus to the SNARE complex potentiates synaptic-vesicle fusogenicity. *Nat Struct Mol Biol* 17(5):568–575.

Supporting Information

Grael et al. 10.1073/pnas.1605256113

SI Methods

KO Mouse Generation. RIM-BP2 and RIM-BP1 KO targeting strategies were designed together with genOway. Targeting vector construction and KO mouse generation by homologous recombination were performed at the genOway facility (Figs. S24 and S44). Briefly, long- and short-homology regions were cloned from C57BL/6 mouse genomic DNA. The targeting vectors contained two loxP sites flanking exon 17 (RIM-BP2) and exons 23–25 (RIM-BP1), respectively, and a neomycin resistance gene flanked by FRT sites for positive selection (Figs. S24 and S44). Additionally, the vectors contained diphtheria toxin A as a negative selection marker. The linearized targeting constructs were transfected into ES cells, and positive clones were selected starting 48 h afterward. After PCR and Southern blot verification of 5' and 3' homologous recombination (Fig. S4 B and C), ES cells were injected into recipient blastocysts and implanted into pseudopregnant C57BL/6 females. The F1 chimeric males were crossed to a C57BL/6 Cre deleter line to excise the loxP flanked sequences, resulting in generation of the constitutive RIM-BP1 and RIM-BP2 KO mouse lines (Figs. S24 and S44). For both single-KO lines, heterozygous animals were backcrossed to C57BL/6 mice and progeny were expanded to establish colonies.

Heterozygous RIM-BP2 mice were bred to obtain homozygous, heterozygous, and WT littermates for all subsequent experiments. Mice from both strains were crossed to obtain RIM-BP1/2 DKO animals. Genotyping PCR on genomic DNA obtained from tail biopsies was performed before neuronal cultures were made, as well as before and after slice experiments (Fig. S4E).

The following primers were used for genotyping: RBP1 WT Salfw: ttatcactgctgcctgccacagcc, RBP1 LA2 forward (fw): agactcgagacaaccagctctctgc, RBP1 LA2 reverse (rev): acatctgaacctctcaggatgggac, RIM-BP2 KO fw: gactcagatctgcatgaggagctctg, RIM-BP2 WT fw: gaacataggacaggcagctacacttctcacctag, and RIM-BP2 WT/KO rev: caactctcacatacatcacctggatcg.

Quantitative Real-Time PCR. RNA was isolated from neuronal cultures at days in vitro (DIV) 3, 10, and 23, DNase I digested to eliminate genomic DNA and transcribed into cDNA. Quantitative real-time PCR was carried out using the LightCycler 480 Probes Master Kit and the LightCycler 480 (Roche Diagnostics). The following primers and Universal ProbeLibrary (UPL) probes were used: RIM-BP1 fw: gacatgtgtgctgctgattt, rev: acatccctgtctgaagg, UPL probe 16 [efficiency (eff.): 2.1]; RIM-BP2 fw: gtggcgga-gggctctcatag, rev: ctgcccgtgtgtattcat, UPL probe 58 (eff.: 1.9); RIM-BP3 fw: ccttagccaccgtaagca, rev: ggactgtgtcagtttcaggtg, UPL probe 1 (eff.: 2.0); and Rpl4 fw: gatgagctgtatggcacttgg, rev: ctgtgcatgggcaggtt, UPL probe 38 (eff.: 1.9).

For RIM-BP1 KO real-time PCR, mRNA was isolated from whole brain of WT, heterozygous, and homozygous littermates; DNase I digested; and transcribed into cDNA. The following primers and UPL probes were used (also Fig. S4D): assay 16: fw: gacatgtgtgctgctgattt, rev: acatccctgtctgaagg, UPL probe 16; assay 33: fw: aggtatgccatctatctga, rev: tgcgtacagtcacctcatgg, UPL probe 33; assay 21: fw: aggtctgtgtaccactgagctg, rev: catcagggttcg-gtgacatt, UPL probe 21; and assay 81: fw: gctgtgtccatccaactt, rev: ctggactcttctctctctg, UPL probe 81.

Immunoprecipitation from P2 Fraction. WT brains (4-wk-old mice) were homogenized in 10 mL of precooled homogenization buffer [0.32 M sucrose, 4 mM Hepes (pH 7.4)] containing 1 mM PMSF and protease inhibitor mixture (Roche Diagnostics). All steps

were performed at 4 °C. Homogenate was centrifuged at 800 × g for 10 min. The supernatant S1 was centrifuged at 10,000 × g for 15 min. The resulting pellet was suspended in 10 mL of homogenization buffer and spun again at 10,000 × g for 15 min. The washed P2 fraction was suspended in 1.8 mL of immunoprecipitation (IP) buffer [25 mM Hepes (pH 8.3), 150 mM NaCl, 1 mM MgCl₂, 10% (vol/vol) glycerol] containing 0.4% deoxycolate sodium salt and 1% Triton X-100. The P2 fraction was solubilized for 1 h and centrifuged at 17,000 × g for 30 min. The supernatant was transferred to the antibody-coupled beads (Protein A beads; Biorad) and incubated overnight. A self-raised rabbit anti-RIM-BP2 antibody (sera generated against peptide covering the last 20 amino acids of mouse RBP2 C terminus) was used, as well as random rabbit IgGs (Sigma–Aldrich) as controls. The input was collected after centrifugation at 1,000 × g for 3 min. The beads were extensively washed in washing buffer [25 mM Hepes (pH 7.4), 150 mM NaCl, 10% glycerol, 0.5% Triton X-100]. Elution of the bound complex was performed by addition of 100 µL of 2× Laemmli sample buffer, boiling the samples at 95 °C for 5 min. For immunoblotting, samples were run on 8% (wt/vol) SDS-polyacrylamide gels. For the P2 input and IP, samples were loaded at 2% and 25%, respectively (discussed below).

Immunohistochemistry. Brains freshly removed from 4- to 6-wk-old RIM-BP2 WT and KO mice were immediately shock-frozen on dry ice. Sagittal brain sections (10 µm) were cut with a cryostat (Leica) and collected on SuperFrost Plus slides (Menzel GmbH). For immunostaining, cryosections of RIM-BP2 WT and KO were processed simultaneously. Sections were fixed with 4% (wt/vol) paraformaldehyde (PFA) in 0.1 M phosphate buffer (PB), pH 7.4, for 10 min at room temperature (RT). Blocking was performed with 10% (vol/vol) normal goat serum (NGS) and 0.3% Triton X-100 in 0.1 M PB for 3 h at RT. Sections were then incubated with goat anti-mouse IgG Fab fragments (1:10; Jackson ImmunoResearch) in 0.1 M PB for 1 h at RT. Primary antibodies diluted in 5% (vol/vol) NGS and 0.3% Triton X-100 in 0.1 M PB were applied overnight at 4 °C. Secondary antibodies were incubated for 2 h at RT. For gSTED imaging, we used the following secondary antibodies: goat anti-guinea pig Alexa 488 (1:200), goat anti-guinea pig Alexa 594 (1:200 or 1:400 for confocal microscopy), goat anti-mouse Alexa 488 (1:200), goat anti-mouse Alexa 532 (1:200), goat anti-mouse ATTO647N (1:100; Active Motif), goat anti-rabbit Alexa 488 (1:200), goat anti-rabbit Alexa 594 (1:200), and goat anti-rabbit ATTO647N (1:100). All secondary antibodies conjugated to Alexa dyes were purchased from Invitrogen. Afterward, sections were washed, postfixed with 3% (wt/vol) PFA and 0.05% glutaraldehyde in 0.1 M PB, and mounted with Mowiol (pH 8) or ProLong Gold (gSTED imaging; Life Technologies) on high-precision glass coverslips. Conventional confocal images of RIM-BP2 immunofluorescence in the hippocampal CA1 area were acquired with a Leica SP5 laser confocal microscope equipped with a 20× 0.7-N.A. oil immersion objective. Primary antibodies used are described in Table S1.

Immunoblotting. For KO mouse analysis, the crude membrane fractions were isolated from WT and KO brain samples to investigate expression of RIM-BP2 and different synaptic proteins (Fig. S2 D–F) or RIM-BP1 (Fig. S4F). Brain samples from 4- to 6-wk-old mice were snap-frozen with liquid nitrogen and stored at –80 °C. Samples were homogenized in 10 vol of homogenization buffer, pH 7.4 (0.32 M sucrose, 10 mM Hepes, 2 mM

EDTA), precooled at 4 °C containing protease inhibitors. Next, the homogenates were centrifuged at $1,000 \times g$ for 15 min to remove the pelleted nuclear fraction (P1). The supernatant (S1) was then taken and centrifuged at $17,000 \times g$ for 30 min. The obtained crude membrane pellet (P2) was resuspended in 200–300 μ L of cold Hepes lysis buffer (50 mM Hepes, 2 mM EDTA). Protein concentrations were determined by Bradford assay. Samples were separated on 8% and 12% (wt/vol) SDS-polyacrylamide gels (30 μ g of protein per lane), transferred to a nitrocellulose membrane (Amersham Protran; GE Healthcare), and probed with different primary antibodies followed by incubation with secondary antibodies conjugated to horseradish peroxidase (Jackson ImmunoResearch). Bound antibodies were visualized using an enhanced chemiluminescence detection system (PerkinElmer Immuno Labs) and imaged with a Biorad ChemiDoc XRS+ imager (Biorad). Protein expression levels were quantified with Image laboratory software (Biorad). All primary antibodies used are described in Table S1.

Electron Microscopy. Hippocampal neurons were plated on sapphire disks and frozen at RT using an HPM 100 (Leica) at DIV 14 as described previously (36). Freeze substitution was performed in AFS2 (Leica). After staining with 1% uranyl acetate, samples were infiltrated and embedded into Epon and cured for 48 h at 60 °C. Serial 40-nm sections were cut using a microtome (Leica) and collected on formvar-coated single-slot grids (Science Services GmbH). Before imaging, sections were contrasted with 2.5% (wt/vol) uranyl acetate. Random profiles were imaged using a Zeiss 900 electron microscope with a digital Proscan 1K Slow-Scan CCD-Camera (Fa. Proscan elektronische Systeme GmbH) and analyzed with a custom-written ImageJ (NIH) and MATLAB (The MathWorks, Inc.) routine.

Electrophysiological Recordings. Whole-cell patch-clamp recordings in autaptic neurons were performed using a Multiclamp 700B amplifier (Molecular Devices) at DIV 13–21. The patch pipette solution contained 136 mM KCl, 17.8 mM Hepes, 1 mM EGTA, 0.6 mM MgCl₂, 4 mM ATP-Mg, 0.3 mM GTP-Na, 12 mM phosphocreatine, and 50 units/mL phosphocreatine kinase (300 mOsm, pH 7.4). The recording chamber was constantly perfused with extracellular solution containing 140 mM NaCl, 2.4 mM KCl, 10 mM Hepes, 2 mM CaCl₂, 4 mM MgCl₂, and 10 mM glucose (pH adjusted to 7.3 with NaOH, 300 mOsm). Solutions were applied using a fast-flow system. Data were filtered at 3 kHz, digitized at 10 kHz, and recorded with pClamp 10 (Molecular Devices). Data were analyzed with Axograph X (AxoGraph Scientific) and Prism 6 (GraphPad Software).

In autaptic cell culture, EPSCs were evoked by a brief 2-ms somatic depolarization to 0 mV from a holding potential of –70 mV. PPRs were calculated as the ratio from the second and first EPSC amplitudes. Hypertonic 500 mM sucrose solution was applied for 5 s to assess the size of the RRP of neurotransmitter vesicles (11). The RRP was assessed by integrating the transient current component evoked by application of hypertonic extracellular solution. Spontaneous release events were detected using a template-based algorithm in Axograph X (37). The spontaneous release rate is the fraction of the RRP released per second by spontaneous release and was calculated by dividing the miniature EPSC (mEPSC) frequency by the number of vesicles within the RRP. Synaptic vesicle fusogenicity was measured by applying 250 mM sucrose solution onto the neuron for 10 s and analyzed as described previously (38). Briefly, to obtain the fraction of RRP released at 250 mM sucrose solution, the charge transfer of the transient synaptic current was measured and divided by the RRP size obtained by application of 500 mM sucrose (5 s) from the same neuron. The peak release rate was calculated by normalizing and integrating the response to

500 mM sucrose. The maximal slope was then quantified as a measure for peak release rate (15).

For the (5*S*,10*R*)-(+)-5-methyl-10,11-dihydro-5*H*-dibenzo[*a,d*]cyclohepten-5,10-imine maleate (MK-801) assay, EPSCs were recorded at 0.33 Hz from autaptic hippocampal neurons. EPSCs were recorded in extracellular solution containing 140 mM NaCl, 2.4 mM KCl, 10 mM Hepes, 1 mM CaCl₂, 0 mM MgCl₂, 10 mM glucose, and 10 μ M glycine (pH adjusted to 7.3 with NaOH, 300 mOsm) until reaching a stable baseline. Progressive block rate was measured in the presence of 5 μ M MK-801. The AMPA component was used to normalize for the NMDA block-independent changes in synaptic transmission.

For calcium sensitivity assays (Fig. 3*F* and *G* and Fig. S3*J* and *K*), EPSCs from autaptic hippocampal neurons were measured in extracellular solution containing 0.5 mM, 2 mM, 4 mM, or 10 mM CaCl₂ and 1 mM MgCl₂. To control for rundown and cell-to-cell variability, test responses were normalized to average EPSCs in standard external solution (2 mM CaCl₂, 4 mM MgCl₂) that were recorded between treatments. Normalized responses were then normalized to the response in 10 mM CaCl₂. The normalized values were fitted into a standard Hill equation [$y = 1 + 10^{((\log EC_{50} - x) \cdot h)}$], where *h* is the Hill slope] to plot dose-response curves. For analysis of C.V. of EPSCs, only cells with an overall stable response were included.

For the functional coupling distance assay (Fig. S6), autaptic neurons were preincubated in 25 μ M EGTA-AM or DMSO control for 15 min, washed three times in extracellular solution, and left for 10–15 min in conditioned Neurobasal A medium (Gibco) to allow for complete cleavage of AM esters. Neurons were recorded within ~30 min thereafter.

For slice preparation, mice were anesthetized and decapitated. The brain was removed and chilled in ice-cold sucrose-artificial cerebrospinal fluid (sACSF) containing 87 mM NaCl, 26 mM NaHCO₃, 10 mM glucose, 50 mM sucrose, 2.5 mM KCl, 1.25 mM NaH₂PO₄, 0.5 mM CaCl₂, and 3 mM MgCl₂ saturated with 95% (vol/vol) O₂/5% (vol/vol) CO₂, pH 7.4. Horizontal slices were cut at 300- μ m thickness on a microslicer (VT1200S; Leica), maintained for 30 min at 35 °C in sACSF and subsequently stored in ACSF containing 119 mM NaCl, 26 mM NaHCO₃, 10 mM glucose, 2.5 mM KCl, 1 mM NaH₂PO₄, 2.5 mM CaCl₂, and 1.3 mM MgCl₂ saturated with 95% (vol/vol) O₂/5% (vol/vol) CO₂, pH 7.4, at RT. Experiments were started after 30 min and no longer than 6 h after the preparation.

For recordings of fPSPs in the stratum radiatum of area CA1, slices were placed in a recording chamber continuously superfused with ACSF (oxygenated with 95% (vol/vol) O₂/5% (vol/vol) CO₂) at RT. Compound polysynaptic potentials were evoked by electrical stimulation of the Schaffer collaterals (0.05-ms duration) via a bipolar insulated stimulation electrode. Extracellular recordings to record from a large number of parallel fiber bundles were performed with a low-resistance patch-pipette filled with recording ACSF placed in the stratum radiatum. Amplitudes of evoked synaptic potentials were measured from averaged ($n = 5$ –10) sweeps. Recordings were performed with a MultiClamp 700B amplifier. Signals were filtered at 2 kHz and digitized (BNC-2090; National Instruments Germany GmbH) at 5 kHz. IGOR Pro software was used for signal acquisition (WaveMetrics, Inc.). Data were analyzed with MATLAB or the Igor plug-in NeuroMatic (neuromatic.thinkrandom.com) software. Statistical analysis was performed with Prism 6.

For whole-cell recordings of spontaneous release in acute slices, intracellular electrodes were pulled from borosilicate glass (1.2-mm OD) and filled with KMeSO₃-based intracellular solutions containing 130 mM KMeSO₃, 10 mM Hepes, 10 mM KCl, 4 mM NaCl, 4 mM MgATP, 0.5 mM NaGTP, and 5 mM phosphocreatine-Na (pH 7.35). Electrode resistance was 2–5 M Ω . Series resistance (*R_s*) and input resistance were constantly monitored by applying a 4-mV hyperpolarizing voltage step for

50 ms. Experiments were discarded if changes in the R_s were >15%. The mEPSCs in slices were isolated at -60 mV in the presence of 1 μ M tetrodotoxin (TTX), 1 μ M GABAzine, 50 μ M D(-)-2-amino-5-phosphonopentanoic acid (D-APV), and 100 μ M cyclothiazide.

SynGCamp6f Imaging. SynGCamp6f was generated analogous to synGCamp2 (35) by fusing GCamp6f (36) to the C terminus of the synaptic vesicle protein synaptophysin. The construct was cloned into lentiviral shuttle vectors under control of the synapsin promoter. Lentiviral particles were produced as previously described (37) by the viral core facility of the Charité Berlin. Mass cultured hippocampal neurons were infected on DIV 1 and imaged on DIV 14–21 at a 2-Hz sampling rate with 100 ms of exposure time as previously described (38). A 490-nm LED system (pE2; CoolLED) was used. Three micromolar 2,3-Dihydroxy-6-nitro-7-sulfamoyl-benzof[*f*]chinoxalin-2,3-dione (NBQX) and 30 μ M bicuculline were added to the external solution to block spontaneous activity.

gSTED Microscopy. STED imaging with time-gated detection was performed using a commercial Leica SP8 TCS STED microscope (Leica Microsystems). Briefly, the system includes an inverted DMi8 CS microscope equipped with a pulsed white light laser (WLL; ~80-ps pulse width, 80-MHz repetition rate; NKT Photonics) for flexible excitation wavelengths and two STED lasers for depletion (continuous wave at 592 nm, pulsed at 775 nm). The pulsed 775-nm STED laser was triggered by the WLL. Within each independent experiment, samples from RIM-BP2 KO and WT mice were acquired with equal settings. In dual-channel experiments Alexa 488 and Alexa 532 were excited using a pulsed WLL at 488 nm and 545 nm, respectively. Depletion occurred at 592 nm. For Alexa 488 and Alexa 594, time gating ranged from 0.8–1.2 ns to 6 ns and from 0.8–2.3 ns to 6 ns, respectively.

Triple-channel STED imaging was performed exciting Alexa 488, Alexa 594, and ATTO647N at 488 nm, 598 nm, and 646 nm, respectively. Alexa 488 was depleted at 592 nm, whereas the 775-nm STED laser was used to deplete both Alexa 594 and ATTO647N. Time-gated detection was set from 0.3–6 ns for both dyes.

Fluorescence signals were detected sequentially by hybrid detectors at appropriate spectral regions separated from the STED laser by corresponding dichroic filters. Single optical slices were acquired with an HC PL APO CS2 100 \times /1.40-N.A. oil objective (Leica Microsystems), a scanning format of 1,024 \times 1,024, eight-bit sampling, and 4.5 zoom, yielding a pixel dimension of 25.25 nm and 25.25 nm in the *x* and *y* dimensions, respectively. To minimize thermal drift, the microscope was housed in a heatable incubation chamber (LIS Life Imaging Services).

Raw dual-channel gSTED images were deconvolved using the built-in algorithm of the Leica LAS-AF software (signal intensity, regulation parameter of 0.05). The point spread function was generated with a 2D Lorentz function having the full-width half-maximum (FWHM) set to 60 nm. Raw data obtained from triple-channel gSTED imaging were deconvolved with Huygens Professional software (Scientific Volume Imaging) using a theoretical point spread function automatically computed based on pulsed- or continuous-wave STED optimized function and the specific microscope parameters. Default deconvolution settings were applied. To measure the effective lateral point spread function of the SP8 TCS STED microscope, we used 40-nm fluorescent beads (Life Technologies; excitation and emission maxima at 505/515 nm or 660/680 nm). Fluorescent beads were diluted 1:80,000 in poly-L-lysine (Sigma) and mounted on coated slides using ProLong Gold (Life Technologies) and high-precision glass coverslips. gSTED imaging was performed at appropriate wavelengths with similar imaging parameters as used for brain cryosections.

Cluster Distance Analysis. For cluster distance analysis, deconvolved images were thresholded and segmented by watershed transform with Amira software (Visualization Sciences Group) to identify individual clusters and to obtain their *x* and *y* coordinates. Within the same independent experiment, the same threshold and segmentation parameters were used. According to the lateral resolution achieved, clusters with a size smaller than 0.0036 μ m² (two-channel gSTED) or 0.0025 μ m² (three-channel gSTED) were not considered for analysis.

The average number of clusters at specific distances and the *k*-nearest neighbor distance were analyzed with a MATLAB custom-written script. In the first step, the script determined the Euclidean distance between all possible cluster pairs in two channels in a matrix. The number of clusters in channel 1 found within 50-nm, 75-nm, 100-nm, 125-nm, 150-nm, 200-nm, and 300-nm distances from each single cluster of channel 2 was calculated and averaged for all particles found in channel 2. Thousands of clusters per single image were automatically analyzed. To identify precisely at which specific distance changes in clustering may occur, the mean number of channel 1 clusters found at sampling distances from channel 2 was expressed in distance intervals (0–50 nm, 50–75 nm, 75–100 nm, 100–125 nm, 0.125–200 nm, and 200–300 nm). The *k*-nearest neighbor distance analysis was similarly based on the matrix containing the distances between all particles in both channels: The distances of all particles in channel 1 to the ones in channel 2 were sorted in ascending order to find the *k*-nearest neighbor. The *k* value was set to 1, 2, 3, 4, and 5. The *k* distance values were then averaged on the number of clusters in channel 2. Data from independent experiments were pooled, and five to nine mice per genotype were analyzed.

Estimation of the Effective gSTED Point Spread Function by Gaussian Fit. To estimate the lateral resolution of the gSTED microscope, fluorescent beads with uniform diameters well below the diffraction limit (~40 nm) were imaged at appropriate wavelengths. We then approximated local intensity profiles with a 2D Gaussian function:

$$f(x, y|\vec{p}) = p_1 + p_2 \exp\left(-\left(\frac{(x-p_3)^2}{p_5} + \frac{(y-p_4)^2}{p_5}\right)\right),$$

where \vec{p} is a parameter vector. In its elements, p_1 represents a baseline pixel intensity value, p_2 corresponds to the peak of the Gaussian, p_3 and p_4 represent its *x* and *y* positions, and p_5 determines its width, which we assume to be equal in both dimensions. To quantify the deviation to the fluorescence profile of the image, a cost value was calculated:

$$\text{cost}(\vec{p}) = \sum_{x=1}^{x_{\max}} \sum_{y=1}^{y_{\max}} (i(x, y) - f(x, y|\vec{p}))^2,$$

where $i(x, y)$ is the intensity value of the experimentally obtained image at positions *x* and *y* and x_{\max} and y_{\max} are the maximal pixel positions (i.e., the image size). The optimal solution of \vec{p} was found by minimizing the cost value using a genetic optimization algorithm, implemented in the function “ga” of MATLAB R2016a with a population size of 500 and lower bounds of zero for all parameter values and upper bounds for p_3 and p_4 of x_{\max} and y_{\max} . There was no upper bound for the other parameters. The FWHM amplitude of the Gaussian was calculated to quantify the lateral resolution from the following relationship:

$$\text{FWHM} = 2\sqrt{p_5 \ln 2}.$$

Absolute distances were calculated from pixel distances by multiplying with a pixel size of 25.25 nm. For display purposes, the 2D

Gaussian was calculated at higher sampling in the plots of Fig. S2 C and D.

Statistics. For all electrophysiological datasets, Prism6 was used for statistical analysis. The D'Agostino–Pearson omnibus test was used to check for normal distribution of data. For WT vs. KO comparison, an unpaired *t* test with Welch's correction was used for normally distributed data and the Mann–Whitney *U* test was used for not normally distributed data.

For the 10-Hz trains in autaptic cultures, the last 10 EPSCs of each cell were averaged and the averages of WT and KO cells were tested using the Mann–Whitney *U* test.

For 14-Hz trains in slices, normalized data were tested using repeated measures ANOVA.

For gSTED, statistical analysis was done with SPSS Statistics software (IBM). Data normality was tested with the Kolmogorov–

Smirnov test. Pairwise comparisons were analyzed with an unpaired Student *t* test or Mann–Whitney *U* test according to normality, unless otherwise stated. Values are expressed as mean \pm SEM, and *n* indicates the number of animal tested.

For Western blot analysis, statistical analysis was performed with SPSS Statistics software, data were tested for normality with the Kolmogorov–Smirnov test, and significances between WT and KO RIM-BP2 animals were analyzed by the Mann–Whitney *U* test or unpaired Student *t* test according to normality. Values are expressed as median (25th–75th percentiles), and *n* indicates the number of animals tested.

For quantitative real-time PCR analysis, data from four independent experiments were pooled. Relative expression levels were tested in Prism 6 using repeated measurement two-way ANOVA with Tukey's multiple comparisons test.

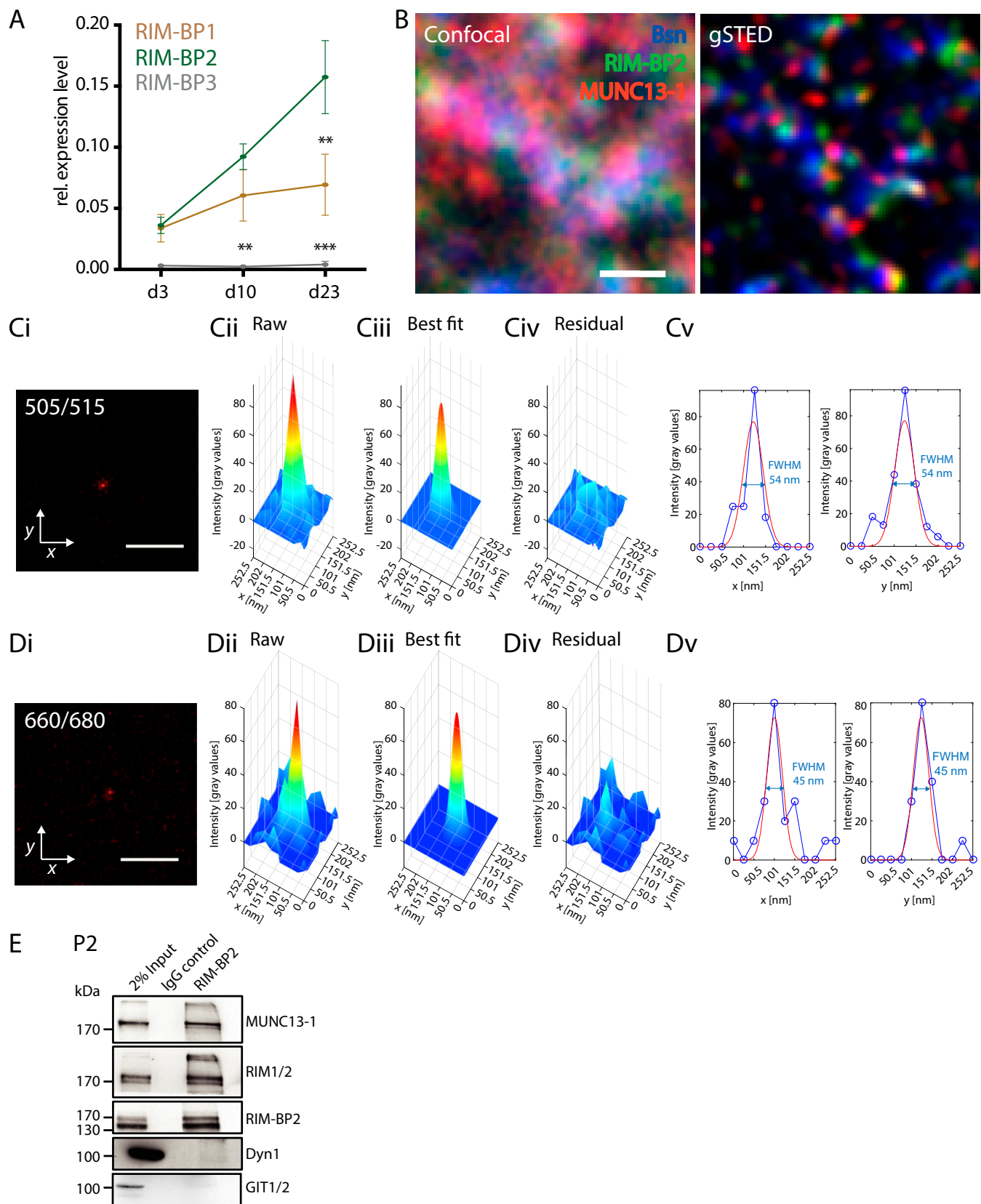


Fig. S1. RIM-BP expression and interaction with RIM and Munc13-1. (A) Relative (rel.) expression levels of RIM-BP1–3 in cultured murine hippocampal neurons over time. The mRNA levels are normalized to Rpl4. Data are expressed as mean \pm SEM, and tested against RIM-BP2 expression levels ($p_{\text{DIV23,RIM-BP1}} = 0.001$, $p_{\text{DIV10,RIM-BP3}} = 0.001$, $p_{\text{DIV23,RIM-BP3}} < 0.001$, Tukey's multiple comparisons test; $n = 4$). * $P < 0.05$; ** $P < 0.01$; *** $P < 0.001$. (B) Confocal (Left) and corresponding gSTED (Right) images of RIM-BP2 localization to Bassoon (Bsn) and MUNC13-1 at CA3-CA1 hippocampal synapses on a WT mouse brain cryosection. (Scale bar: 500 nm.) (C, *i-v* and D, *i-v*) Estimation of the effective lateral point spread function of the gSTED microscope. The gSTED images of a 40-nm fluorescent bead with excitation and emission maxima at 505 and 515 nm (C, *i*) or 660 and 680 (D, *i*), respectively, are shown. (Scale bar: 500 nm.) Three-dimensional surface plot of the local intensity profile (C, *ii* and D, *ii*) approximated with a 2D Gaussian fit (C, *iii* and D, *iii*). (C, *iv* and D, *iv*) Deviation of the 2D Gaussian fit from the intensity profile. (C, *v* and D, *v*) Intensity profile and 2D Gaussian fit values along the x axis for constant y (126.25 nm) (Left) and the y axis for constant x (126.25 nm) (Right). In both channels, the smallest bead had a FWHM of 54 nm (C, *v*) or 45 nm (D, *v*), indicating a lateral resolution of ~ 50 nm. (E) Representative Western blot showing input, IgG control, and immunoprecipitation of RIM-BP2 probed with antibodies against different synaptic proteins. RIM-BP2 forms a complex with the AZ proteins RIM1/2 and MUNC13-1, but not with the endocytic protein Dynamin1 (Dyn1) or the cytomatrix protein GIT.

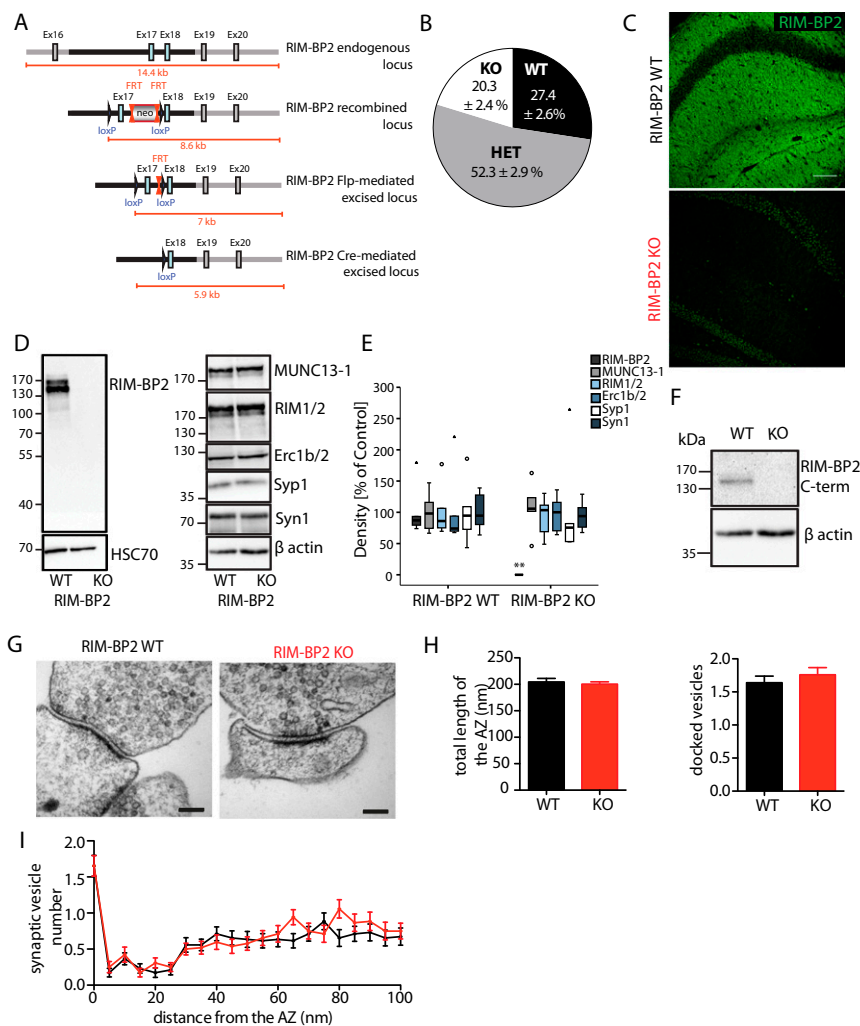
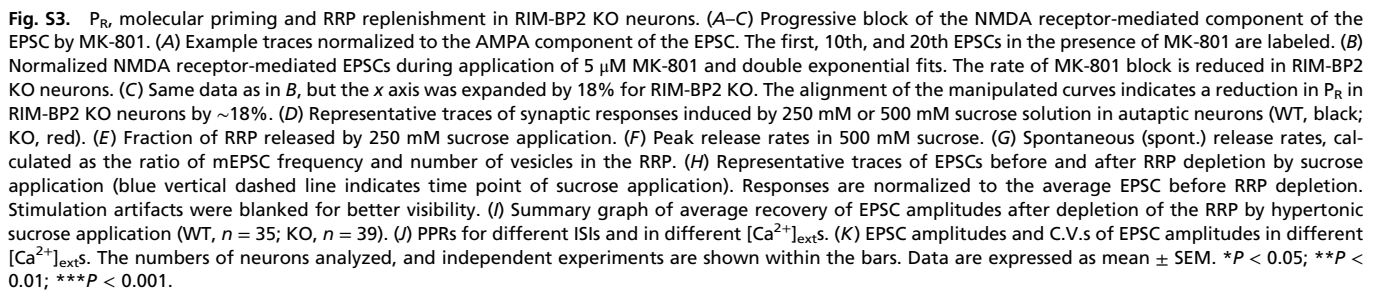


Fig. S2. Generation and characterization of RIM-BP2 KO mice. (A) Schematic representation of the RIM-BP2 targeting strategy showing the endogenous and recombined locus, as well as the RIM-BP2 locus after Flp-mediated and Cre-mediated excision. The RIM-BP2 locus after Cre-mediated excision corresponds to the constitutive RIM-BP2 KO. (B) Mendelian distribution of RIM-BP2-deficient progeny [total number of litters analyzed = 34; total number of animals: WT, 77; heterozygous (HET), 151; KO, 57]. (C) RIM-BP2 expression in the CA1 area of the hippocampus of WT and KO mice. Note the loss of RIM-BP2 immunoreactivity in the KO (WT, $n = 4$; KO, $n = 2$). (Scale bar: 100 μ m.) (D, Left) RIM-BP2 protein expression in WT ($n = 6$) and KO ($n = 6$) mouse crude P2 membrane preparations probed with an RIM-BP2-specific antibody recognizing amino acids 589–869 of rat RIM-BP2, upstream of the deletion site. (D, Right) Expression levels of the AZ proteins RIM1/2, MUNC13-1, and Erc1b/2 and synaptic vesicle proteins Synaptophysin1 (Syp1) and Synapsin1 (Syn1) in the WT and KO mouse are not affected. HSC70 and β -actin were used as loading controls. (E) Quantification of signals from the Western blot analysis in D showing complete loss of RIM-BP2 levels ($n = 6$; $**P < 0.01$, Mann–Whitney U test), but no significant alterations in the levels of other synaptic proteins analyzed ($n = 6$; $P > 0.05$, ERC1b/2/Syp1, Mann–Whitney U test; $P > 0.05$, MUNC13-1/RIMs/Syn1, unpaired Student t test). Data are expressed as median (25th–75th percentiles). Circles indicate outliers, and triangles indicate extremes. (F) RIM-BP2 protein expression in WT ($n = 6$) and KO ($n = 6$) mouse crude P2 membrane preparations probed with RIM-BP2 antibody recognizing the last 20 amino acids of mouse RIM-BP2 C terminus. β -Actin was used as a loading control. (G) Representative electron microscopic images of WT and RIM-BP2 KO synapses. (Scale bars: 100 nm.) (H) Bar graph of total length of the AZ (Left) and number of docked vesicles (Right). (I) Distribution of synaptic vesicles relative to the AZ. Data are expressed as mean \pm SEM.



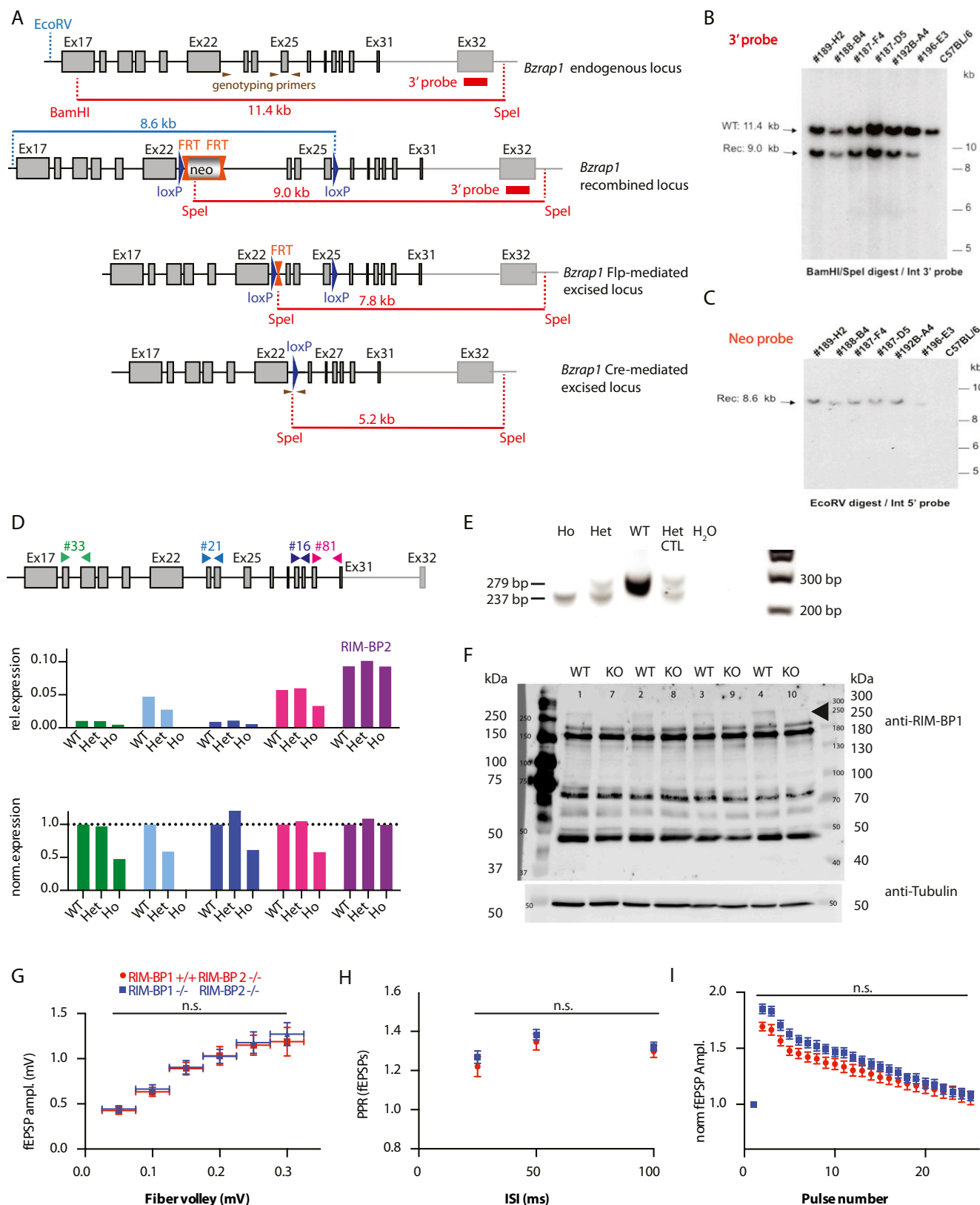


Fig. S4. STP of fEPSPs in the stratum radiatum of RIM-BP1/2 DKO mice. (A) Schematic representation of the *Bzrap1* (*RIM-BP1*) targeting strategy showing the endogenous and recombined locus, as well as the *Bzrap1* locus after Flp-mediated and Cre-mediated excision. The *Bzrap1* locus after Cre-mediated excision corresponds to the constitutive *Bzrap1* KO lacking exons 23–25, which leads to a frameshift and a premature stop codon in exon 27. If the resulting RNA were translated, the resulting truncated 174-kDa protein would lack the second and third SH3 domains, and therefore would likely not be functional. (B) Southern blot analysis for 3' homologous recombination (Rec) in ES cells performed by genOway. The genomic DNA of the tested ES cell clones was compared with WT DNA (C57BL/6). The digested DNA samples were blotted on nylon membrane and hybridized with an external 3' probe (LA-E-A probe) hybridizing downstream of the targeting vector homology sequence (genOway). (C) Southern blot analysis for 5' homologous recombination in ES cells performed by genOway. The genomic DNA of tested ES cell clones was compared with WT DNA (C57BL/6). The digested DNA samples were blotted on nylon membrane and hybridized with the Neo probe detecting the EcoRV fragment to screen for 5' homologous recombination events (genOway). (D) Schematic representation of different real-time PCR (RT-PCR) assays for RIM-BP1 and RT-PCR results of cDNA obtained from RIM-BP1 WT, heterozygous (Het), and homozygous (Ho) KO mouse brain. Expression relative to Rpl4 was normalized (norm.) to WT. The RT-PCR assay 21 confirms that exons 23–25 are deleted in the RIM-BP1 KO. Assays spanning exons before and after the deleted region show a 50% reduction of mRNA levels in the KO. The remaining signals are likely due to the presence of frameshift mRNA that has not been completely degraded. This mRNA would not yield a functional protein. (E) Genotyping results obtained using the three primers indicated in A and genomic DNA from tails of WT, Het, and RIM-BP2 Ho KO littermates. The WT band is larger than the KO band, as indicated. In Het animals, both bands are present. (F) Western blot of P2 fractions of RIM-BP1 WT ($n = 5$) and KO ($n = 5$) mice using the commercially available N-terminal antibody against RIM-BP1 (Synaptic Systems). In RIM-BP1 KO samples, the upper band (arrow) is missing. This band likely corresponds to the RIM-BP1 isoforms with a molecular mass of ~200 kDa. However, the RIM-BP1 antibody recognizes several bands at molecular mass that do not correspond to any of the isoforms described so far, indicating unspecific binding. (G) Input/output curves relating the fEPSP amplitude to the amplitude of the presynaptic fiber volley in stratum radiatum of the CA1 region in acute hippocampal slices (0.05 mV: WT, $n = 20$; KO, $n = 21$; 0.1 mV: WT, $n = 26$; KO, $n = 26$; 0.15 mV: WT, $n = 24$; KO, $n = 25$; 0.2 mV: WT, $n = 19$; KO, $n = 26$; 0.25 mV: WT, $n = 11$; KO, $n = 18$; 0.3 mV: WT, $n = 9$; KO, $n = 19$). (H) Summary graph of PPRs of fEPSPs in the stratum radiatum in response to paired stimulation with indicated ISIs ($n_{WT} = 28$, $n_{KO} = 34$). (I) Summary graph of fEPSPs in response to a 14-Hz stimulation train ($n_{WT} = 10$, $n_{KO} = 17$). Data are expressed as mean \pm SEM. n.s., not significant.

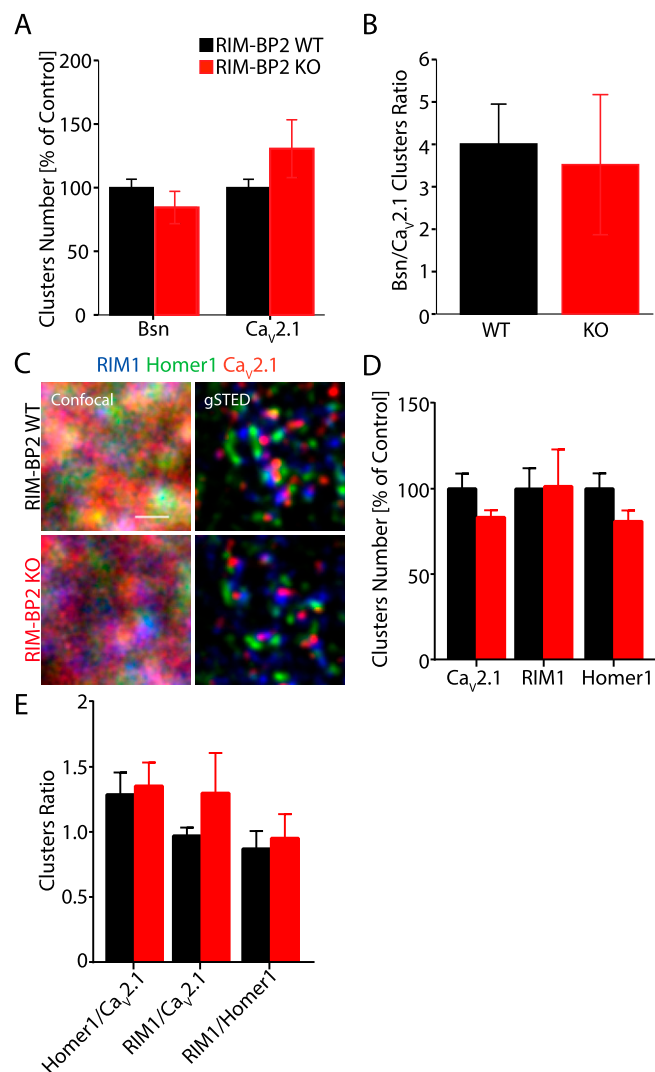


Fig. S5. RIM-BP2 does not significantly alter the number of Cav2.1 clusters. Cluster analysis performed on gSTED images of CA3-CA1 hippocampal synapses in situ shows that RIM-BP2 deletion does not significantly alter either the number of Bsn and Cav2.1 clusters (A) or their ratio (B) (WT, $n = 5$; KO, $n = 6$). (C) Cav2.1, RIM1, and Homer1 distribution at CA3-CA1 hippocampal synapses imaged by conventional confocal (Left) and gSTED (Right) microscopy in brain cryosections of RIM-BP2 WT (Upper) and KO (Lower) mice. (Scale bar: 500 nm.) (D) Quantification of the number of clusters imaged by gSTED (WT, $n = 9$; KO, $n = 9$). Also, this independent experiment showed that the number of Cav2.1 clusters does not significantly change in RIM-BP2 KO mice. (E) Similarly, RIM-BP2 deletion does not significantly alter either the number of Homer1 and RIM1 clusters or their ratio to Cav2.1 channels. However, as shown in D and E, we observed a higher variability in the total number of RIM1 clusters, and therefore in the ratio of RIM1/Cav2.1 clusters at RIM-BP2 KO synapses.

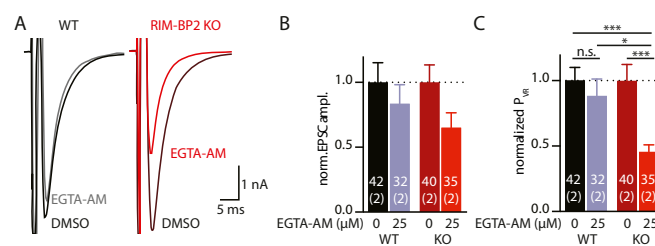


Fig. S6. EGTA-AM reduces P_{VR} significantly more in RIM-BP2 KO than in WT. (A) Representative traces of average EPSCs of WT and RIM-BP2 KO neurons preincubated with 25 μ M EGTA-AM or DMSO control. (B) Normalized EPSC amplitudes of neurons preincubated with 25 μ M EGTA-AM or DMSO control. EPSCs are reduced in EGTA-AM-treated neurons, but the effect is not significant. (C) P_{VR} of the same neurons as in A, normalized to control. EGTA-AM has a significantly stronger effect on the P_{VR} of RIM-BP2 KO neurons than on WT, supporting larger coupling distances. Data are expressed as mean \pm SEM. * $P < 0.05$; *** $P < 0.001$.

Table S1. Primary antibodies for immunohistochemistry and immunoblot

Antigen	Species	Dilution	Source
Bsn (N-terminal)	ms	1:1,200 (IHC)	Abcam
Cav2.1 (rat amino acids 1,921–2,212)	Rb	1:500 (IHC)	Synaptic Systems
Dynamin1	ms	1:1,000 (WB)	Kind gift of P. De Camilli (Boyer Center for Molecular Medicine, New Haven, CT)
ERC1b/2	Rb	1:500 (WB)	Synaptic Systems
GIT1/2 (p95PKL)	ms	1:1,000 (WB)	BD Biosciences
Homer1 (human amino acids 1–186)	GP	1:200 (IHC)	Synaptic Systems
HSC70	ms	1:2,000	Thermo Fisher Scientific
MUNC13-1 (rat amino acids 3–317)	Rb	1:150 (IHC)	Synaptic Systems
MUNC13-1	ms	1:1,000 (WB)	Synaptic Systems
RIM1 (rat amino acids 602–723)	ms	1:200 (IHC)	BD Pharmingen
RIM1/2	Rb	1:2,000 (WB)	Synaptic Systems
RIM-BP1 (mouse amino acids 1–335)	Rb	1:500 (WB)	Synaptic Systems
RIM-BP2 (last 20 aa of RIM-BP2 C terminus)	Rb	1:1,000 (IP, WB)	Self-raised
RIM-BP2 (rat amino acids 589–869)	GP	1:600/1:1,000 (IHC)	Kind gift of A. Fejtova and Eckart Gundelfinger, Leibniz Institute for Neurobiology, Magdeburg, Germany
Synapsin1	ms	1:1,000 (WB)	Synaptic Systems
Synaptophysin1	ms	1:10,000 (WB)	Synaptic Systems
β -Actin	ms	1:2,000 (WB)	Sigma
β -Tubulin	ms	1:2,000 (WB)	Sigma

GP, guinea pig; IHC, immunohistochemistry; ms, mouse; Rb, rabbit; WB, Western blot.

Parameter		RIM-BP2 WT			RIM-BP2 KO			Statistic	
		Mean	SEM	<i>n</i>	Mean	SEM	<i>n</i>	<i>P</i>	Test
Normalized EPSC amplitudes		1.00	0.07	156	0.80	0.06	160	0.0055	Mann–Whitney <i>U</i> test
C.V. of EPSC, %		8.46	0.98	31	11.29	1.16	30	0.0351	Mann–Whitney <i>U</i> test
Normalized RRP size		1.00	0.07	156	0.97	0.08	160	0.2315	Mann–Whitney <i>U</i> test
P _{VR} , %		6.51	0.32	156	5.85	0.46	160	0.0041	Mann–Whitney <i>U</i> test
mEPSC frequency: culture, Hz		5.65	0.76	30	5.61	0.73	30	0.9715	Unpaired Student <i>t</i> test
mEPSC amplitude: culture, pA		30.24	2.37	30	30.37	1.82	30	0.786	Mann–Whitney <i>U</i> test
PPR, 20-ms ISI: culture		0.91	0.03	83	1.10	0.05	82	0.0001	Mann–Whitney <i>U</i> test
PPR, 25-ms ISI: culture		1.13	0.09	83	1.29	0.05	82	<0.0001	Mann–Whitney <i>U</i> test
PPR, 100-ms ISI: culture		0.85	0.02	83	0.92	0.03	82	0.0366	Mann–Whitney <i>U</i> test
Train of 10 Hz: mean of last 10 pulses, nA		0.749	0.003	83	0.866	0.005	82	<0.0001	Mann–Whitney <i>U</i> test
fEPSPs, mV	FV: 0.05 mV	0.51	0.06	21	0.51	0.08	19	0.8285	Mann–Whitney <i>U</i> test
	FV: 0.1 mV	0.82	0.09	21	0.80	0.11	19	0.9137	
	FV: 0.15 mV	1.06	0.12	21	1.02	0.13	19	0.7685	
	FV:0.2 mV	1.23	0.13	21	1.21	0.15	19	0.7046	
	FV: 0.3 mV	1.52	0.17	18	1.59	0.21	14	0.8942	
	FV: 0.4 mV	1.72	0.19	16	1.72	0.23	13	0.9959	
Train of 14 Hz: slices fEPSPs, mV	Pulse 1	1.00	0.00	17	1.00	0.00	18	>0.05	Repeated measurement ANOVA
	Pulse 2	1.16	0.01456		1.27	0.02		<0.05	
	Pulse 3	1.05	0.01644		1.21	0.03		<0.001	
	Pulse 4	0.96	0.01833		1.13	0.03		<0.001	
	Pulse 5	0.91	0.01774		1.08	0.03		<0.001	
	Pulse 6	0.89	0.01940		1.06	0.03		<0.001	
	Pulse 7	0.88	0.01811		1.05	0.03		<0.001	
	Pulse 8	0.87	0.02		1.04	0.03		<0.001	
	Pulse 9	0.86	0.02		1.02	0.03		<0.001	
	Pulse 10	0.85	0.02		1.02	0.03		<0.001	
	Pulse 11	0.84	0.02		1.02	0.03		<0.001	
	Pulse 12	0.83	0.02		1.00	0.03		<0.001	
	Pulse 13	0.82	0.02		1.00	0.03		<0.001	
	Pulse 14	0.81	0.02		0.99	0.03		<0.001	
	Pulse 15	0.80	0.02		0.98	0.03		<0.001	
	Pulse 16	0.79	0.02		0.98	0.03		<0.001	
	Pulse 17	0.77	0.02		0.96	0.03		<0.001	
	Pulse 18	0.76	0.02		0.96	0.03		<0.001	
	Pulse 19	0.76	0.02		0.95	0.03		<0.001	
	Pulse 20	0.74	0.02		0.94	0.03		<0.001	
	Pulse 21	0.73	0.02		0.92	0.03		<0.001	
	Pulse 22	0.72	0.02		0.92	0.03		<0.001	
	Pulse 23	0.71	0.02		0.90	0.03		<0.001	
	Pulse 24	0.71	0.02		0.90	0.03		<0.001	
	Pulse 25	0.70	0.02		0.88	0.04		<0.001	
Fraction of RRP released, %		46.88	5.02	26	47.06	4.20	27	0.8496	Mann–Whitney <i>U</i> test
Peal release rate, 1/s		1.51	0.08	44	1.50	0.06	43	0.0841	Mann–Whitney <i>U</i> test
Spontaneous release rate, 1/s		0.002	0.0005	30	0.002	0.0003	30	0.2554	Mann–Whitney <i>U</i> test
PPR (fEPSP): slice	25-ms ISI	0.98	0.03	21	1.18	0.05	19	0.0003	Mann–Whitney <i>U</i> test
	50-ms ISI	1.17	0.02	21	1.34	0.03	19	<0.0001	Mann–Whitney <i>U</i> test
	100-ms ISI	1.16	0.01	21	1.29	0.02	19	<0.0001	Mann–Whitney <i>U</i> test
mEPSC frequency: slice, Hz		1.00	0.13	15	1.06	0.09	18	0.71	Unpaired Student <i>t</i> test
mEPSC amplitude: slice, pA		13.36	0.35	15	13.51	0.44	18	0.79	Unpaired Student <i>t</i> test
Hill curve	logEC ₅₀	0.25	0.05	22	0.25	0.03	28	0.1158	Extra sum-of squares <i>F</i> test
	Hill slope	3.37	1.95	22	3.74	1.97	28		
PPR (Fig. 3)	0.5 mM Ca ²⁺	1.74	0.20	22	2.22	0.29	28	0.0215	Mann–Whitney <i>U</i> test
	2 mM Ca ²⁺	0.79	0.04	22	0.95	0.06	28	0.0152	Unpaired Student <i>t</i> test
	4 mM Ca ²⁺	0.61	0.04	22	0.67	0.04	28	0.4946	Unpaired Student <i>t</i> test
	10 mM Ca ²⁺	0.49	0.03	22	0.54	0.04	28	0.2875	Unpaired Student <i>t</i> test
P _{VR} , % (Fig. 3)	0.5 mM Ca ²⁺	0.64	0.07	51	0.51	0.09	47	0.0281	Mann–Whitney <i>U</i> test
	4 mM Ca ²⁺	11.49	0.87	51	10.15	1.00	47	0.1303	Mann–Whitney <i>U</i> test

Table S3. Summary of all electrophysiological parameters of RIM-BP1/2 DKO

Parameter		RIM-BP2 KO			RIM-BP1/2 DKO			Statistic	
		Mean	SEM	<i>n</i>	Mean	SEM	<i>n</i>	<i>P</i>	Test
fEPSPs, mV	FV: 0.05 mV	0.43	0.04	20	0.45	0.04	21	0.5212	Mann–Whitney <i>U</i> test
	FV: 0.1 mV	0.63	0.05	26	0.67	0.5	26	0.6148	
	FV: 0.15 mV	0.88	0.07	24	0.90	0.08	25	0.9671	
	FV: 0.2 mV	1.03	0.10	19	1.03	0.08	26	1.0000	
	FV: 0.25 mV	1.15	0.11	11	1.18	0.12	18	0.6488	
	FV: 0.3 mV	1.19	0.16	9	1.27	0.13	19	0.9608	
PPR, fEPSP	25-ms ISI	1.22	0.05	28	1.27	0.03	34	0.1026	Mann–Whitney <i>U</i> test
	50-ms ISI	1.35	0.04		1.38	0.03		0.129	Mann–Whitney <i>U</i> test
	100-ms ISI	1.30	0.03		1.32	0.02		0.2690	Mann–Whitney <i>U</i> test
Train of 14 Hz (fEPSPs)	Pulse 1	1.00	0.00	10	1.00	0.00	17	>0.9999	Repeated measurement ANOVA
	Pulse 2	1.69	0.04		1.85	0.04		0.4137	
	Pulse 3	1.66	0.05		1.83	0.04		0.3003	
	Pulse 4	1.57	0.04		1.70	0.05		0.6672	
	Pulse 5	1.48	0.04		1.63	0.05		0.4986	
	Pulse 6	1.45	0.05		1.57	0.04		0.8907	
	Pulse 7	1.42	0.05		1.55	0.05		0.8047	
	Pulse 8	1.41	0.04		1.52	0.05		0.9056	
	Pulse 9	1.37	0.05		1.50	0.04		0.8488	
	Pulse 10	1.36	0.05		1.47	0.04		0.9551	
	Pulse 11	1.34	0.05		1.46	0.04		0.8304	
	Pulse 12	1.31	0.05		1.43	0.04		0.8703	
	Pulse 13	1.30	0.05		1.39	0.04		0.9966	
	Pulse 14	1.27	0.05		1.36	0.05		0.9944	
	Pulse 15	1.24	0.05		1.34	0.04		0.9862	
	Pulse 16	1.23	0.05		1.31	0.04		0.9995	
	Pulse 17	1.21	0.05		1.28	0.04		0.9999	
	Pulse 18	1.18	0.05		1.23	0.04		>0.9999	
	Pulse 19	1.17	0.05		1.23	0.05		>0.9999	
	Pulse 20	1.15	0.05		1.19	0.05		>0.9999	
	Pulse 21	1.13	0.06		1.18	0.04		>0.9999	
	Pulse 22	1.11	0.06		1.14	0.04		>0.9999	
	Pulse 23	1.10	0.06		1.11	0.04		>0.9999	
	Pulse 24	1.08	0.06		1.10	0.05		>0.9999	
	Pulse 25	1.06	0.06		1.07	0.04		>0.9999	

Table S4. Summary of gSTED-based cluster analysis

Parameter	Distance, nm/k neighbor	RIM-BP2 WT			RIM-BP2 KO			Statistic	
		Mean	SEM	<i>n</i>	Mean	SEM	<i>n</i>	<i>P</i>	Test
Bsn cluster number,* % of control	—	100	6.65	5	84.42	12.70	6	0.311	Unpaired Student <i>t</i> test
Ca _v 2.1 cluster number,* % of control	—	100	6.59	5	130.62	22.73	6	0.245	Unpaired Student <i>t</i> test
Bsn/Ca _v 2.1 ratio*	—	4.01	0.94	5	3.52	1.65	6	0.814	Unpaired Student <i>t</i> test
Mean Bsn cluster number at tested distance to a given Ca _v 2.1 cluster*	0–50	0.164	0.009	5	0.101	0.014	6	0.005	Unpaired Student <i>t</i> test
	50–75	0.181	0.011		0.119	0.018		0.022	
	75–100	0.216	0.013		0.143	0.020		0.017	
	100–125	0.236	0.017		0.163	0.023		0.037	
	125–150	0.251	0.018		0.185	0.031		0.112	
	150–200	0.562	0.044		0.411	0.068		0.110	
	200–300	1.466	0.121		1.078	0.178		0.119	
Mean <i>k</i> distance (Bsn–Ca _v 2.1),* nm	<i>k</i> = 1	148	12	5	225	33	6	0.068	Unpaired Student <i>t</i> test
	<i>k</i> = 2	259	18		360	46		0.082	
	<i>k</i> = 3	339	22		459	57		0.096	
	<i>k</i> = 4	406	26		540	66		0.114	
	<i>k</i> = 5	463	29		611	74		0.119	
Mean <i>k</i> distance (Bsn– Bsn),* nm	<i>k</i> = 1	193	6	5	225	14	6	0.074	Unpaired Student <i>t</i> test
	<i>k</i> = 2	271	11		326	27		0.112	
	<i>k</i> = 3	337	14		410	37		0.123	
	<i>k</i> = 4	395	18		482	44		0.127	
Ca _v 2.1 cluster number, % of control	—	100	8.88	9	83.35	4.11	9	0.116	Unpaired Student <i>t</i> test
RIM1 cluster number, % of control	—	100	12.04	9	101.46	21.64	9	0.954	Unpaired Student <i>t</i> test
Homer1 cluster number, % of control	—	100	9.01	9	80.98	6.37	9	0.104	Unpaired Student <i>t</i> test
RIM1/Ca _v 2.1 ratio	—	0.971	0.064	9	1.300	0.308	9	0.325	Unpaired Student <i>t</i> test
RIM1/Homer1 ratio	—	0.871	0.136	9	0.953	0.184	9	0.725	Unpaired Student <i>t</i> test
Homer1/ Ca _v 2.1 ratio	—	1.288	0.171	9	1.355	0.180	9	0.790	Unpaired Student <i>t</i> test
Mean RIM1 cluster number at tested distance to a given Ca _v 2.1 cluster	0–50	0.115	0.011	9	0.103	0.018	9	0.559	Unpaired Student <i>t</i> test
	50–75	0.131	0.014		0.116	0.020		0.551	
	75–100	0.166	0.019		0.150	0.025		0.625	
	100–125	0.195	0.025		0.174	0.030		0.581	
	125–150	0.218	0.031		0.192	0.032		0.566	
	150–200	0.510	0.078		0.441	0.079		0.545	
	200–300	1.371	0.237		1.161	0.220		0.526	
Mean <i>k</i> distance (RIM1–Ca _v 2.1), nm	<i>k</i> = 1	185	23	9	244	59	9	0.730	Mann–Whitney <i>U</i> test
	<i>k</i> = 2	301	37		385	85		0.796	
	<i>k</i> = 3	386	49		488	104		0.730	
	<i>k</i> = 4	456	58		575	121		0.730	
	<i>k</i> = 5	518	67		653	137		0.730	
Mean Homer1 cluster number at tested distance to a given RIM1 cluster	0–50	0.107	0.006	9	0.089	0.007	9	0.060	Unpaired Student <i>t</i> test
	50–75	0.132	0.007		0.111	0.007		0.045	
	75–100	0.184	0.010		0.154	0.011		0.056	Mann–Whitney <i>U</i> test [†]
	100–125	0.229	0.012		0.191	0.013		0.043	
	125–150	0.265	0.015		0.225	0.015		0.077	
	150–200	0.603	0.037		0.515	0.040		0.122	
	200–300	1.491	0.120		1.252	0.107		0.222 [†]	
Mean <i>k</i> distance (Homer1–RIM1), nm	<i>k</i> = 1	134	7	9	156	9	9	0.064	Unpaired Student <i>t</i> test
	<i>k</i> = 2	229	12		259	15		0.113 [†]	
	<i>k</i> = 3	299	17		338	20		0.161 [†]	Mann–Whitney <i>U</i> test [†]
	<i>k</i> = 4	358	22		403	24		0.113 [†]	
	<i>k</i> = 5	409	25		461	28		0.113 [†]	
Mean Homer1 cluster number at tested distance to a given Ca _v 2.1 cluster	0–50	0.114	0.007	9	0.096	0.007	9	0.077	Unpaired Student <i>t</i> test
	50–75	0.142	0.009		0.123	0.008		0.136	
	75–100	0.188	0.011		0.167	0.011		0.193	Mann–Whitney <i>U</i> test [†]
	100–125	0.223	0.013		0.197	0.013		0.136 [†]	
	125–150	0.241	0.015		0.210	0.013		0.127	
	150–200	0.534	0.038		0.448	0.030		0.094	
	200–300	1.406	0.118		1.156	0.092		0.050 [†]	
Mean <i>k</i> distance (Homer1–Ca _v 2.1), nm	<i>k</i> = 1	142	10	9	158	8	9	0.050 [†]	Unpaired Student <i>t</i> test
	<i>k</i> = 2	243	15		266	13		0.161 [†]	
	<i>k</i> = 3	316	19		346	17		0.265	Mann–Whitney <i>U</i> test [†]
	<i>k</i> = 4	376	23		412	21		0.270	
	<i>k</i> = 5	428	26		468	24		0.267	

*Double immunolabeling Bassoon/Ca_v2.1 in hippocampal cryosections.[†]Mann–Whitney *U* test, exact significance [*2* * (one-tailed)].

3. Discussion

Our analysis of neurotransmitter release in RIM-BP2-deficient neurons demonstrates a unique role of RIM-BP2 in the fine positioning of $\text{Ca}_\text{v}2$ s within the AZ of glutamatergic murine hippocampal synapses, thereby ensuring proper synaptic function.

Functionally, loss of RIM-BP2 resulted in a moderate reduction of release probability and a surprisingly pronounced increase in short-term facilitation during repetitive stimulation, attributable to an increase in the coupling distance between $\text{Ca}_\text{v}2$ s and the Ca^{2+} sensor and release machinery. These results are in agreement with previously published results obtained in other model systems (Acuna et al., 2015; Davydova et al., 2014; Liu et al., 2011) and a very recent study published shortly after the acceptance of our article (Acuna et al., 2016).

In murine RIM/RIM-BP quadruple KO neurons (QKO), Acuna and colleagues found a depletion of presynaptic dense projections indicative of a (at least partial) disruption of AZ structure, an almost complete loss of SV docking and priming and a severe impairment of Ca^{2+} -evoked release (Acuna et al., 2016). The remaining release was asynchronous and multiquantal. Surprisingly, the observed phenotypes in the RIM/RIM-BP QKO were mostly superadditive, exceeding the severity expected by simply adding the phenotypes of RIM1/2 DKO and RIM-BP1/2 DKO.

We found no evidence of a molecular priming deficit in RIM-BP2-deficient autaptic hippocampal neurons. The superadditive effect of RIM and RIM-BP deletion on the RRP size in the Calyx of Held (Acuna et al., 2016), however, could indicate that RIM-BPs do play a role in molecular priming, a function that might be occluded in our study by a functional redundancy of RIMs and RIM-BPs. Indeed, protein expression levels of the priming factor Munc13-1 are strongly reduced in the RIM/RIM-BP QKO neurons (Acuna et al., 2016). Therefore, RIMs and RIM-BPs might support SV priming by specifically stabilizing Munc13s. This would be in agreement with our finding that RIM-BP2 forms a stable complex with RIMs and Munc13-1 (Grauel et al., 2016; Fig. S1E). Consistently, at the NMJ of *Drosophila melanogaster*, the RIM-BP ortholog DRBP also plays a role in SV priming (Müller et al., 2015).

Astonishingly, quadruple deletion of RIM/RIM-BP led to an increase in the length of the postsynaptic density (PSD), which is accompanied by an increase in the expression levels of postsynaptic proteins, such as PSD95, Homer, GluA1 and NRB2 (Acuna et al., 2016). A similar phenotype can neither be detected in the RIM DKO (Acuna et al., 2016; Kaeser et al., 2011), nor in the Munc13 DKO (Augustin et al., 1999; Imig et al., 2014), nor in the RIM/ELKS QKO (Wang et al., 2016). Therefore, the increased PSD length is not simply an adaptation to the release phenotype or the disruption of AZ integrity. The results clearly indicate an important and redundant function of RIMs and RIM-BPs in trans-synaptic signaling and alignment of the PSD with the presynaptic AZ. Again, this function might not have become evident in our study due to redundancies of RIMs and RIM-BPs.

The trans-synaptic phenotype could also suggest a concerted action of RIMs and RIM-BPs in synapse assembly. Indeed, RIM-BPs have been shown to interact with Bassoon (Davydova et al., 2014). Bassoon, in turn, is crucial for the formation of precursor vesicles for AZ assembly (Dresbach et al., 2006; Maas et al., 2012). Moreover, DRBP binds to the adaptor protein Aplip1 in *Drosophila melanogaster* and are thought to be responsible for the co-transport of Bruchpilot to putative sites of synapse formation (Siebert et al., 2015). It is also plausible to argue that the trans-synaptic signaling might involve indirect interactions of RIMs with LAR-type receptor phosphotyrosine phosphatases via α -liprins, as LAR-type receptors have been implicated in synapse formation and trans-synaptic adhesion (reviewed in Um and Ko, 2013). Therefore, RIMs and RIM-BPs might act together as scaffolds in AZ formation.

In both studies published by Acuna and colleagues (Acuna et al., 2015, 2016) RIM-BP1 and RIM-BP2 were simultaneously deleted, not allowing for a differential analysis of their function. We found that in murine glutamatergic hippocampal neurons depletion of RIM-BP1 alone did not affect evoked release parameters (Figure 6 of the Introduction, unpublished data). This could be either due to a marginal role of RIM-BP1 in this type of synapse or to functional redundancies between the two isoforms. We therefore compared evoked release in acute hippocampal slices of RIM-BP2 KO and RIM-BP1/2 DKO animals and showed that the PPR and STP phenotype observed in RIM-BP2-deficient neurons was not exacerbated by the additional depletion of RIM-BP1. Hence, our data show that RIM-BP2 is the functionally more important isoform in glutamatergic hippocampal synapses. However, this might not be true for all synapse types. Differences in the observed phenotypes in different model systems (Acuna et al., 2015; Grauel et al., 2016) could be due to a differential expression of RIM-BPs and Ca_v s. Consistently, Davydova and colleagues have shown that the interaction of Bassoon and RIM-BP2 specifically controls the localization of $Ca_v2.1$ but not $Ca_v2.2$ channels in murine hippocampal neurons.

4. Conclusion

Many open questions concerning the unique functions of RIM-BPs persist and need to be addressed in future studies.

The role of RIM-BP1 and potential differential functions of RIM-BP splice variants remain elusive. Do they co-exist in the same synaptic terminals or are they differentially expressed in different synapse types? How do the different RIM-BP isoforms interact with specific types of Ca_v s expressed in different synapse types? It is also unclear whether RIM-BPs function only in the stable tethering of Ca_v s near release sites or if they are also crucial for Ca_v recruitment to the presynapse or the AZ. RIMs and RIM-BPs likely form part of the dense projections at the AZ (Acuna et al., 2016). However, other constituent proteins still need to be identified and the exact function of dense projections at central mammalian synapses remains unresolved. Additionally, an interesting question is how the

presynaptic RIM/RIM-BP complex regulates PSD size. What are the exact roles of RIM-BPs and which RIM-BP interaction partners might be involved?

Addressing these open questions will not only give us a better understanding of RIM-BP function but also enhance our knowledge of the development, maintenance and function of pre- and postsynaptic neuronal structures. Ultimately, these studies will also give us a better comprehension of the mechanisms of neuronal dysfunctions in mental disabilities and autism spectrum disorders, which have been linked to several mutations in the RIM and RIM-BP genes (Bucan et al., 2009; Hussman et al., 2011; Krumm et al., 2015; Pinto et al., 2010).

5. Appendix

5.1. References (from Introduction, Discussion and Conclusion)

- Acuna, C., Liu, X., Gonzalez, A., and Südhof, T.C. (2015). RIM-BPs Mediate Tight Coupling of Action Potentials to Ca^{2+} -Triggered Neurotransmitter Release. *Neuron* 87, 1234–1247.
- Acuna, C., Liu, X., and Südhof, T.C. (2016). How to Make an Active Zone: Unexpected Universal Functional Redundancy between RIMs and RIM-BPs. *Neuron* 91, 792–807.
- Altrock, W.D., tom Dieck, S., Sokolov, M., Meyer, A.C., Sigler, A., Brakebusch, C., Fässler, R., Richter, K., Boeckers, T.M., Potschka, H., et al. (2003). Functional inactivation of a fraction of excitatory synapses in mice deficient for the active zone protein bassoon. *Neuron* 37, 787–800.
- Augustin, I., Rosenmund, C., Südhof, T.C., and Brose, N. (1999). Munc13-1 is essential for fusion competence of glutamatergic synaptic vesicles. *Nature* 400, 457–461.
- Basu, J., Shen, N., Dulubova, I., Lu, J., Guan, R., Guryev, O., Grishin, N. V., Rosenmund, C., and Rizo, J. (2005). A minimal domain responsible for Munc13 activity. *Nat. Struct. Mol. Biol.* 12, 1017–1018.
- Basu, J., Betz, A., Brose, N., and Rosenmund, C. (2007). Munc13-1 C1 Domain Activation Lowers the Energy Barrier for Synaptic Vesicle Fusion. *J. Neurosci.* 27, 1200–1210.
- Betz, A., Thakur, P., Junge, H.J., Ashery, U., Rhee, J.S., Scheuss, V., Rosenmund, C., Rettig, J., and Brose, N. (2001). Functional interaction of the active zone proteins Munc13-1 and RIM1 in synaptic vesicle priming. *Neuron* 30, 183–196.
- Bliss, T.V.P., and Collingridge, G.L. (1993). A synaptic model of memory: long-term potentiation in the hippocampus. *Nature* 361, 31–39.
- Breustedt, J., Vogt, K.E., Miller, R.J., Nicoll, R.A., and Schmitz, D. (2003). $\alpha 1\text{E}$ -containing Ca^{2+} channels are involved in synaptic plasticity. *Proc. Natl. Acad. Sci. U. S. A.* 100, 12450–12455.
- Bucan, M., Abrahams, B.S., Wang, K., Glessner, J.T., Herman, E.I., Sonnenblick, L.I., Alvarez Retuerto, A.I., Imielinski, M., Hadley, D., Bradfield, J.P., et al. (2009). Genome-wide analyses of exonic copy number variants in a family-based study point to novel autism susceptibility genes. *PLoS Genet.* 5, e1000536.
- Castillo, P.E., Janz, R., Südhof, T.C., Tzounopoulos, T., Malenka, R.C., and Nicoll, R. a (1997). Rab3A is essential for mossy fibre long-term potentiation in the hippocampus. *Nature* 388, 590–593.
- Castillo, P.E., Schoch, S., Schmitz, F., Südhof, T.C., and Malenka, R.C. (2002). RIM1 α is required for presynaptic long-term potentiation. *Nature* 415, 327–330.
- Catterall, W.A. (2011). Voltage-Gated Calcium Channels. *Cold Spring Harb. Perspect. Biol.* 3, a003947–a003947.
- Catterall, W.A., and Few, A.P. (2008). Calcium Channel Regulation and Presynaptic Plasticity. *Neuron* 59, 882–901.
- Catterall, W.A., Leal, K., and Nanou, E. (2013). Calcium Channels and Short-term Synaptic Plasticity. *J. Biol. Chem.* 288, 10742–10749.
- Chen, J., Billings, S.E., and Nishimune, H. (2011). Calcium channels link the muscle-derived synapse organizer laminin $\beta 2$ to Bassoon and CAST/Erc2 to organize presynaptic active zones. *J. Neurosci.* 31, 512–525.
- Citri, A., and Malenka, R.C. (2008). Synaptic plasticity: multiple forms, functions, and mechanisms. *Neuropsychopharmacology* 33, 18–41.
- Coppola, T., Magnin-Luthi, S., Perret-Menoud, V., Gattesco, S., Schiavo, G., and Regazzi, R. (2001).

- Direct interaction of the Rab3 effector RIM with Ca^{2+} channels, SNAP-25, and synaptotagmin. *J. Biol. Chem.* 276, 32756–32762.
- Dai, Y., Taru, H., Deken, S.L., Grill, B., Ackley, B., Nonet, M.L., and Jin, Y. (2006). SYD-2 Liprin- α organizes presynaptic active zone formation through ELKS. *Nat Neurosci* 9, 1479–1487.
- Davydova, D., Marini, C., King, C., Klueva, J., Bischof, F., Romorini, S., Montenegro-Venegas, C., Heine, M., Schneider, R., Schröder, M.S., et al. (2014). Bassoon Specifically Controls Presynaptic P/Q-type Ca^{2+} Channels via RIM-Binding Protein. *Neuron* 82, 181–194.
- Deng, L., Kaeser, P.S., Xu, W., and Südhof, T.C. (2011). RIM Proteins Activate Vesicle Priming by Reversing Autoinhibitory Homodimerization of Munc13. *Neuron* 69, 317–331.
- Dick, O., tom Dieck, S., Altmann, W.D., Ammermüller, J., Weiler, R., Garner, C.C., Gundelfinger, E.D., and Brandstätter, J.H. (2003). The presynaptic active zone protein bassoon is essential for photoreceptor ribbon synapse formation in the retina. *Neuron* 37, 775–786.
- Dresbach, T., Torres, V., Wittenmayer, N., Altmann, W.D., Zamorano, P., Zuschratter, W., Nawrothki, R., Ziv, N.E., Garner, C.C., and Gundelfinger, E.D. (2006). Assembly of active zone precursor vesicles: obligatory trafficking of presynaptic cytomatrix proteins Bassoon and Piccolo via a trans-Golgi compartment. *J. Biol. Chem.* 281, 6038–6047.
- Dulubova, I., Lou, X., Lu, J., Huryeva, I., Alam, A., Schneggenburger, R., Südhof, T.C., and Rizo, J. (2005). A Munc13/RIM/Rab3 tripartite complex: from priming to plasticity? *EMBO J.* 24, 2839–2850.
- Dunlap, K., Luebke, J.I., and Turner, T.J. (1995). Exocytotic Ca^{2+} channels in mammalian central neurons. *Trends Neurosci.* 18, 89–98.
- Eggermann, E., Bucurenciu, I., Goswami, S.P., and Jonas, P. (2011). Nanodomain coupling between Ca^{2+} channels and sensors of exocytosis at fast mammalian synapses. *Nat. Rev. Neurosci.* 13, 7–21.
- Fernández-Chacón, R., Königstorfer, A., Gerber, S.H., García, J., Matos, M.F., Stevens, C.F., Brose, N., Rizo, J., Rosenmund, C., and Südhof, T.C. (2001). Synaptotagmin I functions as a calcium regulator of release probability. *Nature* 410, 41–49.
- Fouquet, W., Oswald, D., Wichmann, C., Mertel, S., Depner, H., Dyba, M., Hallermann, S., Kittel, R.J., Eimer, S., and Sigrist, S.J. (2009). Maturation of active zone assembly by *Drosophila* Bruchpilot. *J. Cell Biol.* 186, 129–145.
- Frank, T., Rutherford, M.A., Strenzke, N., Neef, A., Pangršič, T., Khimich, D., Fejtova, A., Fetjova, A., Gundelfinger, E.D., Liberman, M.C., et al. (2010). Bassoon and the synaptic ribbon organize Ca^{2+} channels and vesicles to add release sites and promote refilling. *Neuron* 68, 724–738.
- Fukuda, M. (2003). Distinct Rab binding specificity of Rim1, Rim2, rabphilin, and Noc2. Identification of a critical determinant of Rab3A/Rab27A recognition by Rim2. *J. Biol. Chem.* 278, 15373–15380.
- Galiègue, S., Jbilo, O., Combes, T., Bribes, E., Carayon, P., Le Fur, G., and Casellas, P. (1999). Cloning and characterization of PRAX-1. A new protein that specifically interacts with the peripheral benzodiazepine receptor. *J. Biol. Chem.* 274, 2938–2952.
- Gasparini, S., Kasyanov, a M., Pietrobon, D., Voronin, L.L., and Cherubini, E. (2001). Presynaptic R-type calcium channels contribute to fast excitatory synaptic transmission in the rat hippocampus. *J. Neurosci.* 21, 8715–8721.
- Grauel, M.K., Maglione, M., Reddy-Alla, S., Willmes, C.G., Brockmann, M.M., Trimbach, T., Rosenmund, T., Pangalos, M., Vardar, G., Stumpf, A., et al. (2016). RIM-binding protein 2 regulates release probability by fine-tuning calcium channel localization at murine hippocampal synapses. *Proc. Natl. Acad. Sci.* 113, 201605256.
- Gundelfinger, E.D., Reissner, C., and Garner, C.C. (2016). Role of Bassoon and Piccolo in Assembly and Molecular Organization of the Active Zone. *Front. Synaptic Neurosci.* 7.
- Hallermann, S., and Silver, R.A. (2013). Sustaining rapid vesicular release at active zones: potential

roles for vesicle tethering. *Trends Neurosci.* 36, 185–194.

Hallermann, S., Fejtova, A., Schmidt, H., Weyhersmüller, A., Silver, R.A., Gundelfinger, E.D., and Eilers, J. (2010). Bassoon Speeds Vesicle Reloading at a Central Excitatory Synapse. *Neuron* 68, 710–723.

Han, Y., Kaeser, P.S., Südhof, T.C., and Schneggenburger, R. (2011). RIM determines Ca^{2+} channel density and vesicle docking at the presynaptic active zone. *Neuron* 69, 304–316.

Held, R.G., Liu, C., and Kaeser, P.S. (2016). ELKS controls the pool of readily releasable vesicles at excitatory synapses through its N-terminal coiled-coil domains. *Elife* 5, 7250–7257.

Hibino, H., Pironkova, R., Onwumere, O., Vologodskaya, M., Hudspeth, A.J., and Lesage, F. (2002). RIM Binding Proteins (RBPs) Couple Rab3-Interacting Molecules (RIMs) to Voltage-Gated Ca^{2+} Channels. *Neuron* 34, 411–423.

Holderith, N., Lorincz, A., Katona, G., Rózsa, B., Kulik, A., Watanabe, M., and Nusser, Z. (2012). Release probability of hippocampal glutamatergic terminals scales with the size of the active zone. *Nat. Neurosci.* 15, 988–997.

Hussman, J.P., Chung, R.-H., Griswold, A.J., Jaworski, J.M., Salyakina, D., Ma, D., Konidari, I., Whitehead, P.L., Vance, J.M., Martin, E.R., et al. (2011). A noise-reduction GWAS analysis implicates altered regulation of neurite outgrowth and guidance in autism. *Mol. Autism* 2, 1.

Imig, C., Min, S.-W., Krinner, S., Arancillo, M., Rosenmund, C., Südhof, T.C., Rhee, J., Brose, N., and Cooper, B.H. (2014). The morphological and molecular nature of synaptic vesicle priming at presynaptic active zones. *Neuron* 84, 416–431.

Junge, H.J., Rhee, J.-S., Jahn, O., Varoqueaux, F., Spiess, J., Waxham, M.N., Rosenmund, C., and Brose, N. (2004). Calmodulin and Munc13 form a Ca^{2+} sensor/effector complex that controls short-term synaptic plasticity. *Cell* 118, 389–401.

Kaeser, P.S., Kwon, H.-B., Blundell, J., Chevalayre, V., Morishita, W., Malenka, R.C., Powell, C.M., Castillo, P.E., and Südhof, T.C. (2008). RIM1 α phosphorylation at serine-413 by protein kinase A is not required for presynaptic long-term plasticity or learning. *Proc. Natl. Acad. Sci. U. S. A.* 105, 14680–14685.

Kaeser, P.S., Deng, L., Wang, Y., Dulubova, I., Liu, X., Rizo, J., and Südhof, T.C. (2011). RIM Proteins Tether Ca^{2+} Channels to Presynaptic Active Zones via a Direct PDZ-Domain Interaction. *Cell* 144, 282–295.

Kaufmann, N., DeProto, J., Ranjan, R., Wan, H., and Van Vactor, D. (2002). Drosophila liprin- α and the receptor phosphatase Dlar control synapse morphogenesis. *Neuron* 34, 27–38.

Khimich, D., Nouvian, R., Pujol, R., tom Dieck, S., Egner, A., Gundelfinger, E.D., and Moser, T. (2005). Hair cell synaptic ribbons are essential for synchronous auditory signalling. *Nature* 434, 889–894.

Kintscher, M., Wozny, C., Jochenning, F.W., Schmitz, D., and Breustedt, J. (2013). Role of RIM1 α in short- and long-term synaptic plasticity at cerebellar parallel fibres. *Nat. Commun.* 4.

Kittel, R.J., Wichmann, C., Rasse, T.M., Fouquet, W., Schmidt, M., Schmid, A., Wagh, D. a, Pawlu, C., Kellner, R.R., Willig, K.I., et al. (2006). Bruchpilot promotes active zone assembly, Ca^{2+} channel clustering, and vesicle release. *Science* 312, 1051–1054.

Kiyonaka, S., Wakamori, M., Miki, T., Uriu, Y., Nonaka, M., Bito, H., Beedle, A.M., Mori, E., Hara, Y., De Waard, M., et al. (2007). RIM1 confers sustained activity and neurotransmitter vesicle anchoring to presynaptic Ca^{2+} channels. *Nat. Neurosci.* 10, 691–701.

Kiyonaka, S., Nakajima, H., Takada, Y., Hida, Y., Yoshioka, T., Hagiwara, A., Kitajima, I., Mori, Y., and Ohtsuka, T. (2012). Physical and functional interaction of the active zone protein CAST/ERC2 and the β -subunit of the voltage-dependent Ca^{2+} channel. *J. Biochem.* 152, 149–159.

Ko, J., Na, M., Kim, S., Lee, J.-R., and Kim, E. (2003a). Interaction of the ERC family of RIM-binding proteins with the liprin- α family of multidomain proteins. *J. Biol. Chem.* 278, 42377–42385.

- Ko, J., Kim, S., Valtschanoff, J.G., Shin, H., Lee, J.-R., Sheng, M., Premont, R.T., Weinberg, R.J., and Kim, E. (2003b). Interaction between liprin- α and GIT1 is required for AMPA receptor targeting. *J. Neurosci.* *23*, 1667–1677.
- Krumm, N., Turner, T.N., Baker, C., Vives, L., Mohajeri, K., Witherspoon, K., Raja, A., Coe, B.P., Stessman, H.A., He, Z., et al. (2015). Excess of rare, inherited truncating mutations in autism. *Nat. Genet.* *47*, 582–588.
- Leal-Ortiz, S., Waites, C.L., Terry-Lorenzo, R., Zamorano, P., Gundelfinger, E.D., and Garner, C.C. (2008). Piccolo modulation of Synapsin1a dynamics regulates synaptic vesicle exocytosis. *J. Cell Biol.* *181*, 831–846.
- Liu, C., Bickford, L.S., Held, R.G., Nyitrai, H., Sudhof, T.C., and Kaeser, P.S. (2014). The active zone protein family ELKS supports Ca^{2+} influx at nerve terminals of inhibitory hippocampal neurons. *J. Neurosci.* *34*, 12289–12303.
- Liu, K.S.Y., Siebert, M., Mertel, S., Knoche, E., Wegener, S., Wichmann, C., Matkovic, T., Muhammad, K., Depner, H., Mettke, C., et al. (2011). RIM-Binding Protein, a Central Part of the Active Zone, Is Essential for Neurotransmitter Release. *Science* (80-.). *334*, 1565–1569.
- Liu, X., Seven, A.B., Camacho, M., Esser, V., Xu, J., Trimbuch, T., Quade, B., Su, L., Ma, C., Rosenmund, C., et al. (2016). Functional synergy between the Munc13 C-terminal C1 and C2 domains. *Elife* *5*, 1–27.
- Lu, J., Machius, M., Dulubova, I., Dai, H., Südhof, T.C., Tomchick, D.R., and Rizo, J. (2006). Structural basis for a Munc13-1 homodimer to Munc13-1/RIM heterodimer switch. *PLoS Biol.* *4*, e192.
- Maas, C., Torres, V.I., Altrock, W.D., Leal-Ortiz, S., Wagh, D., Terry-Lorenzo, R.T., Fejtova, A., Gundelfinger, E.D., Ziv, N.E., and Garner, C.C. (2012). Formation of Golgi-derived active zone precursor vesicles. *J. Neurosci.* *32*, 11095–11108.
- Malenka, R.C., and Bear, M.F. (2004). LTP and LTD: an embarrassment of riches. *Neuron* *44*, 5–21.
- Maglione, Marta, and Stephan J Sigrist. 2013. “Seeing the Forest Tree by Tree: Super-Resolution Light Microscopy Meets the Neurosciences.” *Nature Neuroscience* *16*(7): 790–97.
- Mendoza Schulz, A., Jing, Z., Sánchez Caro, J.M., Wetzels, F., Dresbach, T., Strenzke, N., Wichmann, C., and Moser, T. (2014). Bassoon-disruption slows vesicle replenishment and induces homeostatic plasticity at a CNS synapse. *EMBO J.* *33*, 512–527.
- Mittelstaedt, T., and Schoch, S. (2007). Structure and evolution of RIM-BP genes: Identification of a novel family member. *Gene* *403*, 70–79.
- Mukherjee, K., Yang, X., Gerber, S.H., Kwon, H.-B., Ho, A., Castillo, P.E., Liu, X., and Sudhof, T.C. (2010). Piccolo and bassoon maintain synaptic vesicle clustering without directly participating in vesicle exocytosis. *Proc. Natl. Acad. Sci.* *107*, 6504–6509.
- Müller, M., Genç, Ö., and Davis, G.W. (2015). RIM-Binding Protein Links Synaptic Homeostasis to the Stabilization and Replenishment of High Release Probability Vesicles. *Neuron* *85*, 1056–1069.
- Nadkarni, S., Bartol, T.M., Stevens, C.F., Sejnowski, T.J., and Levine, H. (2012). Short-term plasticity constrains spatial organization of a hippocampal presynaptic terminal. *Proc. Natl. Acad. Sci. U. S. A.* *109*, 14657–14662.
- Ohtsuka, T., Takao-Rikitsu, E., Inoue, E., Inoue, M., Takeuchi, M., Matsubara, K., Deguchi-Tawarada, M., Satoh, K., Morimoto, K., Nakanishi, H., et al. (2002). Cast: a novel protein of the cytomatrix at the active zone of synapses that forms a ternary complex with RIM1 and munc13-1. *J. Cell Biol.* *158*, 577–590.
- Olivera, B.M., Miljanich, G.P., Ramachandran, J., and Adams, M.E. (1994). Calcium Channel Diversity and Neurotransmitter Release: The ω -Conotoxins and ω -Agatoxins. *Annu. Rev. Biochem.* *63*, 823–867.
- Olsen, O., Moore, K.A., Fukata, M., Kazuta, T., Trinidad, J.C., Kauer, F.W., Streuli, M., Misawa, H.,

- Burlingame, A.L., Nicoll, R.A., et al. (2005). Neurotransmitter release regulated by a MAL-S-liprin- α presynaptic complex. *J. Cell Biol.* 170, 1127–1134.
- Pinto, D., Pagnamenta, A.T., Klei, L., Anney, R., Merico, D., Regan, R., Conroy, J., Magalhaes, T.R., Correia, C., Abrahams, B.S., et al. (2010). Functional impact of global rare copy number variation in autism spectrum disorders. *Nature* 466, 368–372.
- Poirier, M.A., Xiao, W., Macosko, J.C., Chan, C., Shin, Y.-K., and Bennett, M.K. (1998). The synaptic SNARE complex is a parallel four-stranded helical bundle. *Nat. Struct. Biol.* 5, 765–769.
- Regus-Leidig, H., Fuchs, M., Löhner, M., Leist, S.R., Leal-Ortiz, S., Chiodo, V.A., Hauswirth, W.W., Garner, C.C., and Brandstätter, J.H. (2014). In vivo knockdown of Piccolino disrupts presynaptic ribbon morphology in mouse photoreceptor synapses. *Front. Cell. Neurosci.* 8, 259.
- Rhee, J.S., Betz, A., Pyott, S., Reim, K., Varoqueaux, F., Augustin, I., Hesse, D., Südhof, T.C., Takahashi, M., Rosenmund, C., et al. (2002). b Phorbol ester- and diacylglycerol-induced augmentation of transmitter release is mediated by Munc13s and not by PKCs. *Cell* 108, 121–133.
- Rizo, J., and Rosenmund, C. (2008). Synaptic vesicle fusion. *Nat. Struct. Mol. Biol.* 15, 665–674.
- Rosenmund, C., Sigler, A., Augustin, I., Reim, K., Brose, N., and Rhee, J.S. (2002). Differential control of vesicle priming and short-term plasticity by Munc13 isoforms. *Neuron* 33, 411–424.
- Sakamoto, S., Ishizaki, T., Okawa, K., Watanabe, S., Arakawa, T., Watanabe, N., and Narumiya, S. (2012). Liprin- α controls stress fiber formation by binding to mDia and regulating its membrane localization. *J. Cell Sci.* 125, 108–120.
- Schikorski, T., and Stevens, C.F. (1997). Quantitative ultrastructural analysis of hippocampal excitatory synapses. *J. Neurosci.* 17, 5858–5867.
- Schoch, S., and Gundelfinger, E.D. (2006). Molecular organization of the presynaptic active zone. *Cell Tissue Res.* 326, 379–391.
- Schoch, S., Castillo, P.E., Jo, T., Mukherjee, K., Geppert, M., Wang, Y., Schmitz, F., Malenka, R.C., and Südhof, T.C. (2002). RIM1 α forms a protein scaffold for regulating neurotransmitter release at the active zone. *Nature* 415, 321–326.
- Serra-Pagès, C., Kedersha, N.L., Fazikas, L., Medley, Q., Debant, A., and Streuli, M. (1995). The LAR transmembrane protein tyrosine phosphatase and a coiled-coil LAR-interacting protein co-localize at focal adhesions. *EMBO J.* 14, 2827–2838.
- Serra-Pagès, C., Medley, Q.G., Tang, M., Hart, A., and Streuli, M. (1998). Liprins, a family of LAR transmembrane protein-tyrosine phosphatase-interacting proteins. *J. Biol. Chem.* 273, 15611–15620.
- Sheng, J., He, L., Zheng, H., Xue, L., Luo, F., Shin, W., Sun, T., Kuner, T., Yue, D.T., and Wu, L. (2012). Calcium-channel number critically influences synaptic strength and plasticity at the active zone. *Nat. Neurosci.* 15, 998–1006.
- Shin, O.-H., Lu, J., Rhee, J.-S., Tomchick, D.R., Pang, Z.P., Wojcik, S.M., Camacho-Perez, M., Brose, N., Machius, M., Rizo, J., et al. (2010). Munc13 C2B domain is an activity-dependent Ca²⁺ regulator of synaptic exocytosis. *Nat. Struct. Mol. Biol.* 17, 280–288.
- Siebert, M., Böhme, M.A., Driller, J.H., Babikir, H., Mampell, M.M., Rey, U., Ramesh, N., Matkovic, T., Holton, N., Reddy-Alla, S., et al. (2015). A high affinity RIM-binding protein/Aplip1 interaction prevents the formation of ectopic axonal active zones. *Elife* 4, 1–30.
- Südhof, T.C. (2004). THE SYNAPTIC VESICLE CYCLE. *Annu. Rev. Neurosci.* 27, 509–547.
- Südhof, T.C. (2012). The Presynaptic Active Zone. *Neuron* 75, 11–25.
- Südhof, T.C. (2013). A molecular machine for neurotransmitter release: synaptotagmin and beyond. *Nat. Med.* 19, 1227–1231.
- Sutton, R.B., Fasshauer, D., Jahn, R., and Brunger, A.T. (1998). Crystal structure of a SNARE complex involved in synaptic exocytosis at 2.4 Å resolution. *Nature* 395, 347–353.

- Takao-Rikitsu, E., Mochida, S., Inoue, E., Deguchi-Tawarada, M., Inoue, M., Ohtsuka, T., and Takai, Y. (2004). Physical and functional interaction of the active zone proteins, CAST, RIM1, and Bassoon, in neurotransmitter release. *J. Cell Biol.* *164*, 301–311.
- Taru, H., and Jin, Y. (2011). The Liprin Homology Domain Is Essential for the Homomeric Interaction of SYD-2/Liprin- α Protein in Presynaptic Assembly. *J. Neurosci.* *31*, 16261–16268.
- Um, J.W., and Ko, J. (2013). LAR-RPTPs: synaptic adhesion molecules that shape synapse development. *Trends Cell Biol.* *23*, 465–475.
- Varoqueaux, F., Sigler, A., Rhee, J.-S., Brose, N., Enk, C., Reim, K., and Rosenmund, C. (2002). Total arrest of spontaneous and evoked synaptic transmission but normal synaptogenesis in the absence of Munc13-mediated vesicle priming. *Proc. Natl. Acad. Sci. U. S. A.* *99*, 9037–9042.
- Waites, C.L., Leal-Ortiz, S. a., Andlauer, T.F.M., Sigrist, S.J., and Garner, C.C. (2011). Piccolo regulates the dynamic assembly of presynaptic F-actin. *J. Neurosci.* *31*, 14250–14263.
- Waites, C.L., Leal-Ortiz, S.A., Okerlund, N., Dalke, H., Fejtova, A., Altrock, W.D., Gundelfinger, E.D., and Garner, C.C. (2013). Bassoon and Piccolo maintain synapse integrity by regulating protein ubiquitination and degradation. *EMBO J.* *32*, 954–969.
- Wang, S.S.H., Held, R.G., Wong, M.Y., Liu, C., Karakhanyan, A., and Kaeser, P.S. (2016). Fusion Competent Synaptic Vesicles Persist upon Active Zone Disruption and Loss of Vesicle Docking. *Neuron* *91*, 777–791.
- Wang, Y., Sugita, S., and Sudhof, T.C. (2000). The RIM/NIM family of neuronal C2 domain proteins. Interactions with Rab3 and a new class of Src homology 3 domain proteins. *J. Biol. Chem.* *275*, 20033–20044.
- Wang, Y., Liu, X., Biederer, T., and Südhof, T.C. (2002). A family of RIM-binding proteins regulated by alternative splicing: Implications for the genesis of synaptic active zones. *Proc. Natl. Acad. Sci. U. S. A.* *99*, 14464–14469.
- Xu, J., Camacho, M., Xu, Y., Esser, V., Liu, X., Trimbuch, T., Pan, Y.-Z., Ma, C., Tomchick, D.R., Rosenmund, C., et al. (2017). Mechanistic insights into neurotransmitter release and presynaptic plasticity from the crystal structure of Munc13-1 C1C2 BMUN. *Elife* *6*.
- Yang, Y., and Calakos, N. (2010). Acute In Vivo Genetic Rescue Demonstrates That Phosphorylation of RIM1 Serine 413 Is Not Required for Mossy Fiber Long-Term Potentiation. *J. Neurosci.* *30*, 2542–2546.
- Zhen, M., and Jin, Y. (1999). The liprin protein SYD-2 regulates the differentiation of presynaptic termini in *C. elegans*. *Nature* *401*, 371–375.
- Zhou, J., Du, Y.-R., Qin, W.-H., Hu, Y.-G., Huang, Y.-N., Bao, L., Han, D., Mansouri, A., and Xu, G.-L. (2009). RIM-BP3 is a manchette-associated protein essential for spermiogenesis. *Development* *136*, 373–382.
- Zucker, R.S., and Regehr, W.G. (2002). Short-Term Synaptic Plasticity. *Annu. Rev. Physiol.* *64*, 355–405.

5.2. List of Figures and Tables (from Introduction)

Figure 1 The presynaptic active zone.....	16
Table 1 Voltage-gated Ca^{2+} channel gene families and subtypes.....	18
Figure 2 Structure of voltage-gated Ca^{2+} channels.....	19
Figure 3 Overview of mouse Bzap1 (RIM-BP1) transcripts.	20
Figure 4 Schematic diagram of the domain structure of mouse RIM-BP isoforms..	21
Figure 5 Structure of the T-bar at the AZ of <i>Drosophila</i> neuromuscular junction.	22
Figure 6 Deletion of RIM-BP1 does not affect evoked release in glutamatergic hippocampal neurons.	26

5.3. Nomenclature

ACh	Acetylcholine
ASD	autism spectrum disorders
AZ	active zone
C.V.	coefficient of variation
CA1	<i>Cornu Ammonis</i> area 1 of the hippocampus
Cac	Cacophony; α -subunit of Ca_v s expressed in <i>Drosophila melanogaster</i>
Ca_v	voltage-gated Ca^{2+} channel
$Ca_v2.1$	P/Q-type voltage-gated Ca^{2+} channel
$Ca_v2.2$	N-type voltage-gated Ca^{2+} channel
DAG	Diacylglycerol
DRBP	<i>Drosophila melanogaster</i> ortholog of RIM-binding proteins; encoded by the <i>dRBP</i> gene
EGTA	Ethylene glycol-bis(2-aminoethylether)-N,N,N',N'-tetraacetic acid
EGTA-AM	membrane-permeable EGTA acetoxymethyl ester
ELKS	active zone protein named after its high content in the amino acids E, L, K, and S
EPSC	excitatory postsynaptic currents
fEPSP	field excitatory postsynaptic potentials
FNIII	fibronectin III repeat
GABA	γ -aminobutyric acid
LAR	Leukocyte-common antigen related
LTP	long-term plasticity
mEPSC	miniature excitatory postsynaptic currents
MK-801	(5S,10R)-(+)-5-methyl-10,11-dihydro-5H-dibenzo[a,d] cyclohepten-5,10-imine maleate; noncompetitive NMDA receptor blocker
NMDA	N-Methyl-D-aspartic acid
NMJ	neuromuscular junction
PDZ domain	structural protein domain; named after the first proteins discovered to contain this domain (PSD-95, Discs-large, ZO-1)
PPR	paired-pulse ratio
P_R	synaptic release probability
PSD	postsynaptic density
P_{VR}	vesicular release probability
RIM	Rab3-interacting molecule
RIM-BP	RIM-binding protein
RRP	readily-releasable pool; pool of fusion-competent synaptic vesicles
SH3	Src-homology 3 domain
SNAP-25	Synaptosome-associated protein of 25,000 relative molecular mass
SNAREs	soluble N-ethylmaleimide-sensitive factor attachment protein receptors
STED	stimulated emission depletion microscopy
STP	short-term plasticity
SV	synaptic vesicle
SynGCamp6f	synaptically localized version of the Calcium indicator protein GCamp6f

5.4. Statement of contribution

The present study was conducted as a collaborative scientific project. In the following I state my contributions to the published data (Grauel et al., 2016):

All experiments underlying figures **Fig.1B-K, Fig. 3, Fig. S1A, Fig. S2B, Fig. S3, Fig. S4D-E and Fig. S6** of the article published in *PNAS* (Grauel et al., 2016) were designed, conducted and analyzed by me. Experimental contributions to these figures by others are stated in the following:

Fig. 1.(B)-(K) Effect of RIM-BP2 deletion on synaptic transmission in autaptic hippocampal neurons.

Marisa Brockmann contributed some recordings to (B) and (D)-(K).

Tanja Rosenmund contributed some recordings to (B) and (D)-(E).

Fig. 3. RIM-BP2 deletion alters Ca^{2+} sensitivity of release.:

Thorsten Trimbuch designed the SynGCamp6f construct and the Viral Core Facility (VCF) of the Charité Universitätsmedizin Berlin cloned and produced the lentiviral construct used for (A)-(C).

Tanja Rosenmund contributed some recordings to (D)-(G).

Fig. S3. P_R , molecular priming and RRP replenishment in RIM-BP2 KO neurons.

Gülçin Vardar contributed some recordings to (B).

Marisa Brockmann and Tanja Rosenmund contributed some recordings to (E)-(K).

The following contributions to figures in the article (Grauel et al., 2016) were made by co-authors:

Dr. Marta Maglione contributed the gSTED data to figures Fig.1A, Fig.4, Fig.S1B-D and Fig. S5 as well as biochemistry and immunocytochemistry data to figures Fig.S1E, Fig.S2C-F and Fig.S4F.

Dr. Suneel Reddy-Alla contributed to the design of the knockout strategies.

Claudia G. Willmes, Dr. Maria Pangalos and A. Stumpf contributed electrophysiological data from acute hippocampal slices to figures Fig. 2 and Fig.S4G-I.

Dr. Marisa M. Brockmann contributed electron microscopic data to figure Fig. S2G-E.

Dr. Alexander M. Walter contributed analytical tools for gSTED analysis.

The initial draft of the publication (Grauel et al., 2016) was written by me and Dr. Marta Maglione. Dr. Benjamin R. Rost, Prof. Dr. Britta J. Eickholt, Prof. Dr. Volker Haucke, Prof. Dr. Dietmar Schmitz, Prof. Dr. Stephan J. Sigrist and Prof. Dr. Christian Rosenmund contributed with helpful discussions and advice.

5.5. Acknowledgements

This thesis would never have been possible without the support and influence of several people:

Foremost I want to thank Prof. Dr. Christian Rosenmund for giving me the opportunity to do my PhD thesis in his lab, for his guidance and support throughout the past years. He has given me a lot of freedom to try out new ideas and was very encouraging when I decided to change the topic of my thesis. I also want to thank him for giving me the possibility to visit the laboratory of Thomas Südhof at Stanford University to learn new methods involving human induced neurons.

I also would like to thank Prof. Dr. Stephan Sigrist for evaluating and examining my thesis and for the constructive suggestions and support during the writing of our manuscript.

I am also very thankful to Dr. Marta Maglione and all other co-authors of the article we published in *PNAS* last year. Working together with all of them has been a great pleasure indeed.

I am especially grateful to Dr. Benjamin Rost who - even though not my official supervisor - has continued to be a very important and inspiring mentor and friend to me.

For all their help, fruitful discussions and the great working atmosphere I want to thank all current and former members of the Rosenmund lab, in particular Melissa Herman, Marisa Brockmann, Marcial Camacho Perez, Thorsten Trimbuch, Pascal Fenske, Tanja Rosenmund, Marta Orlando, Shu-Wen Chang, Gülçin Vardar, Johannes Zimmermann and Julia Jordan. I am also very thankful to Heidi Pretorius for her excellent help with all the small and big organizational and bureaucratic issues, and our technical assistants Bettina Brokowski, Annegret Felies, Rike Dannenberg, Sabine Lenz, Katja Pötschke and Berit Soehl-Kielczynski for their invaluable practical support in cell culture, virus production and electron microscopy.

Special thanks to Lauren E. Mamer, who I have missed a ton during the last months, not only for correcting and improving my English, but above all for cheering me up innumerable times and being a truly great friend.

I also want to thank the *Studienstiftung des deutschen Volkes* for funding and supporting me throughout the past few years.

Finally, I wish to thank all my family and friends - and most of all my husband Javier - for their understanding and support during the good and bad times of my PhD thesis. It wasn't always easy and I certainly would not have made it until here without them.

5.6. Curriculum Vitae

Der Lebenslauf ist in der Online-Version aus Gründen des Datenschutzes nicht enthalten.

5.7. Erklärung an Eides statt

Hiermit erkläre ich, Marie Katharina Grauel, , dass ich die vorliegende Dissertation selbständig verfasst habe. Es wurden für diese Arbeit keine anderen als die angegebenen Quellen und Hilfsmittel verwendet.

Ich versichere, dass die vorliegende Arbeit nicht schon einmal in einem früheren Promotionsverfahren angenommen oder als ungenügend beurteilt worden ist.

Berlin, den 16. März 2017

Marie Katharina Grauel